INFRARED MAGNETO-SPECTROSCOPY OF GRAPHITE AND GRAPHENE NANORIBBONS

A Thesis
Presented to
The Academic Faculty

by

Wenlong Yu

In Partial Fulfillment
of the Requirements for the Degree
Doctor of Philosophy in the
School of Physics

Georgia Institute of Technology
December 2014

INFRARED MAGNETO-SPECTROSCOPY OF GRAPHITE AND GRAPHENE NANORIBBONS

Approved by:

Professor Zhigang Jiang,
Committee Chair
School of Physics
Georgia Institute of Technology

Professor Zhigang Jiang, Advisor
School of Physics
Georgia Institute of Technology

Professor Walter A. de Heer
School of Physics
Georgia Institute of Technology

Professor Phillip First
School of Physics
Georgia Institute of Technology

Professor Edward Conrad
School of Physics
Georgia Institute of Technology

Professor Wenshan Cai
School of Electrical and Computer Engineering and Materials Science and Engineering
Georgia Institute of Technology

Date Approved: 24 June 2014

To my parents Dezhen Lv and Guoyi Yu,

my sister Huaping Yu,

and my wife Wen Zheng.

I love you all dearly.

ACKNOWLEDGEMENTS

I would never have been able to finish my thesis without the guidance of my committee members, help from friends, and support from my family and wife.

I would like to express my deepest appreciation to my advisor Professor Zhigang Jiang, for his excellent guidance, caring, patience, and providing me with an excellent atmosphere for doing research. I would like to thank all my labmates. I want to thank Dr. Chao Huan for helping with the cryostat system. I want to thank Xunchi Chen, Yuxuan Jiang, Di Chen, and Owen Vail for interesting discussions and help in the lab. Special thanks to Dr. Daniel Benjamin for helping me get familiar with the lab, for teaching me to use equipment, and for playing racquet ball with me. I would like to thank my collaborators for their kind help at National High Magnetic Field Laboratory. I want to thank Dr. Dmitry Smirnov, Dr. Jean-Marie Poumirol for their excellent work, and especially Dr. "Richard" Li-Chun Tung for passing on his knowledge of infrared spectroscopy. I would like to thank my fellow students for providing me academic and technical support. I want to thank Dr. Rui Dong, Dr. Jeremy Hicks, Dr. Ming Ruan, Dr. Yike Hu, John Hankinson, James Palmer, Zelei Guo for help with my research. I want to thank all my friends in Atlanta. Dr. Lede Xian, Feng Wang, Wenchao Jiang, Feifei Qian, Xiaofeng Meng, Ruoyu Li, Chao Shi, Yuntao Li, Ruomeng Yu, Shangguo Zhu, Yang Gao, and Qi Ge for their kindness, good advice, and friendship.

I would also like to thank my parents and my sister. They are always supporting me and encouraging me with their best wishes. Finally, I would like to thank my wife, Wen Zheng for her patience, her support and always standing by me through the good times and bad.

TABLE OF CONTENTS

DEDICATION . . . . . **iii**

ACKNOWLEDGEMENTS . . . . . **iv**

LIST OF TABLES . . . . . **vii**

LIST OF FIGURES . . . . . **viii**

SUMMARY . . . . . **xiv**

I INTRODUCTION **1**

1.1 The Electronic Properties of Graphene and Graphite 2

1.1.1 Single Layer Graphene 2

1.1.2 Bilayer Graphene 6

1.1.3 Bulk Graphite 9

1.2 Magnetic Field Effect 11

1.2.1 Landau levels in Monolayer Graphene 11

1.2.2 Bilayer Graphene and Graphite 13

1.3 Outline of the Thesis 17

II EXPERIMENTAL TECHNIQUES **18**

2.1 Fourier Transform Infrared Spectroscopy 18

2.1.1 Introduction 18

2.1.2 Simplified Math Description 20

2.1.3 Experimental Setup 22

2.2 Graphene Nanoribbon Array Fabrication 23

2.2.1 Electron-beam Lithography 23

2.2.2 Oxygen Plasma Etching 24

2.2.3 High Vacuum Annealing 25

2.3 Sample Characterization 26

III TUNING ELECTRON-PHONON COUPLING IN GRAPHITE VIA A MAGNETIC FIELD 28

3.1 Introduction to Magnetophonon Resonance in Graphene and Graphite 28

3.2 Experiments and Discussion 31

3.2.1 Experimental Method 31

3.2.2 Results and Analysis 32

3.3 Conclusion 40

IV MAGNETOPLASMONS IN EPITAXIAL GRAPHENE NANORIBBONS 43

4.1 Introduction 43

4.1.1 Epitaxial Graphene 43

4.1.2 Infrared Magneto-spectroscopy of Epitaxial Graphene 44

4.1.3 Plasmons in graphene structures 54

4.2 Experiments and Discussions 64

4.2.1 Experimental Method 64

4.2.2 Results and Analysis 65

4.3 Conclusion 76

V CONCLUSION 78

REFERENCES 80

VITA 92

LIST OF TABLES

1 Plasmon energy ω_p extracted from Figure 51 and Figure 54. 77

LIST OF FIGURES

1 (a) Exfoliated monolayer graphene on 300nm-thick SiO_2 on Si substrate. (b) Contour plot of the visible contrast of graphene on SiO_2 as a function of wavelength and SiO_2's thickness. Calculated based on the method described in Ref. [1]. 1

2 Honeycomb lattice and its Brillouin zone. (a) Lattice structure of graphene. $\boldsymbol{a}_1$ and $\boldsymbol{a}_2$ are the lattice unit vector, and δ_i, $i = 1, 2, 3$ are the nearest-neighbor vectors. (b) Corresponding Brillouin zone. Dirac cones are at the $\mathbf{K}$ and $\mathbf{K}'$ points. 3

3 Calculated electronic dispersion of graphene using Eq. 5. E is in units of t. (a) Energy spectrum in units of t, with $a = 1.42\,\text{Å}$ and $t' = -0.1t$. The plane is located at $E = 0$. (b) Energy spectrum with $t' = 0$. The energy bands close to the Dirac points are linear. 4

4 Lattice structure of bilayer graphene with various hopping energies. The A atoms are over each other while the B atoms are displaced with respect to each other. The Slonczewski-Weiss-McClure (SWM) parameters are labeled as γ_0, γ_1, γ_3,and γ_4. 7

5 Calculated band structure of bilayer graphene using Eq. 22 with $v_F = 10^6\,\text{m/s}$ and $t_\perp = 0.4\,\text{eV}$. (a) Band structure of bilayer graphene for $V = \gamma_3 = 0$. (b) Band structure of bilayer graphene for $V = 0.05\,\text{eV}$ and $\gamma_3 = 0$. 9

6 (a) Crystal structure of bulk graphite. The graphene layers are stacked in AB order. $\gamma_i\,(i = 1, ..., 5)$ defines the hopping energy. (b) Brillouin zone of bulk graphite. 10

7 Numerically calculated Landau levels of monolayer graphene as a function of magnetic field. Here, $e = 1.6 \times 10^{-19}$C, $\hbar = 1.05 \times 10^{-34}\,\text{J} \cdot \text{s}$, and $v_F = 10^6$ m/s. 12

8 Transitions between Landau levels in monolayer graphene. (a) Relative transmission spectrum at 0.4 T and 1.9 K shows four transitions. (b) The observed transitions plotted as a function of B. The solid symbols are data obtained from the measurement and the dashed lines represent the best fits with Fermi velocity $v_F = 1.03 \times 10^6\,m/s$. Reprinted from Ref.[2]. 13

9 Landau levels in the bilayer graphene as a function of the magnetic field using Eq. 34. Here, $e = 1.6 \times 10^{-19}$C, $\hbar = 1.05 \times 10^{-34}\,\text{J} \cdot \text{s}$, $v_F = 10^6$m/s, and $t = 0.4$ eV. 14

10 Normalized infrared transmission spectra of bilayer graphene. The resonance dips are due to the intraband transitions. Picture adapted from [3]. 15

11 Numerically calculated LLs in graphite at $B = 20\,\mathrm{T}$ as a function of k_z. Here, $\gamma_0 = 2.88\,\mathrm{eV}$, $\gamma_1 = 0.38\,\mathrm{eV}$, $\gamma_2 = -0.02\,\mathrm{eV}$, $\gamma_3 = 0$, $\gamma_4 = 0.072\,\mathrm{eV}$, $\gamma_5 = 0.028\,\mathrm{eV}$, and $\Delta = 0.0075\,\mathrm{eV}$ [4]. 15

12 (a) Landau-level transitions related to the H point as a function of $\sqrt{B}$. The solid and dashed lines represent expected results calculated using Eq. 31 with $v_F = 1.02 \times 10^6\,\mathrm{m/s}$. (b) Landau-level transitions related to the K point as a function of B. The solid lines show expected dipole-allowed transitions calculated using Eq. 37 with $\gamma_0 = 3.2\,\mathrm{eV}$ and $\gamma_1 = 0.375\,\mathrm{eV}$. Grey data points were taken on highly oriented pyrolytic graphite, which exhibit a behavior nearly identical to natural graphite. The inset schematically shows the observed interband transitions in the effective bilayer. Reprinted from Ref. [5]. 16

13 The block diagram of an FTIR spectrometer 19

14 Schematic of an interferometer. The beam is split into two by the beamsplitter. Two beams travel a distance x_1 and x_2 when they are recombined, respectively. 20

15 (a) Interferogram. (b) The spectrum obtained by Fourier transform from the interferogram. 21

16 (a) Layout of the experimental setup. (b) Parabolic cone: the surface is coated with a thin layer of gold for better reflection. (c) Constant DC voltage is applied to the silicon bolometer while the current is measured. 22

17 SEM image of epitaxial graphene ribbon array. (a) The size of the array is $2\,\mathrm{mm} \times 2\,\mathrm{mm}$. (b) Zoomed-in view of (a). The width of ribbon is 100 nm with 100 nm spacing. 24

18 Graphene nanoribbon array fabrication process. 25

19 SEM image of epitaxial graphene nanoribbon arrays. (a) Four arrays on the substrate. Each array is $400\,\mu\mathrm{m}$ by $40\,\mu\mathrm{m}$ and the spacing between arrays is $100\,\mu\mathrm{m}$. (b) 50 nm wide ribbons with 100 nm spacing. (c) 100 nm wide ribbons with 100 nm spacing. (d) 200 nm wide ribbons with 200 nm spacing. 26

20 AFM image of epitaxial graphene nanoribbon arrays. (a) The width of ribbon is 200 nm with 200 nm spacing. The bottom panel shows the line profile. The pair of red arrows measures the width and the pair of green arrows gives the thickness of the ribbon. The thickness of multilayer epitaxial graphene is $\sim 148.9\,\text{Å}$ corresponding to ~ 44 graphene layers. (b) 3D view of the ribbons. 27

21 (a) Color map of the magneto-oscillatory component of Raman scattering spectra of E_{2g} band phonons as a function of magnetic field measured at $T = 4.2$ K. The extracted peak position is shown with full dots. The size is proportional to the line amplitude. Solid lines T_k represent the energies of the inter-Landau-level transitions: $L_{-k,(-k-1)} \rightarrow L_{k+1,(k)}$, which couple to E_{2g} phonon. (b) Zoomed-in view of the 0 to 10 T range of the magnetic fields. Reprinted from Ref. [6]. 29

22 Magnetic field evolution of the peak position (upper part) and the linewidth of the magneto-oscillatory component of the measured E_{2g} Raman band. Solid red lines show the best fit using Eq. 44. Reprinted from Ref. [6]. 31

23 (a) The Scotch tape used for our ultrathin graphite flakes preparation. The part number is 34-8702-3430-8. (b) Raman spectrum of ultrathin graphite flakes. Typical G peak and D' peak are evidenced. Inset: Optical image of ultrathin graphite flakes. 32

24 Infrared transmission spectrum of the Scotch tape used in the experiment at zero magnetic field. 33

25 The raw spectra of ultrathin graphite flakes on the Scotch tape. . . . 34

26 The relative transmission spectra of ultrathin graphite flakes on Scotch tape at different magnetic fields. The spectra are vertically shifted for clarity. The dashed red, orange, and green lines represent the best fits to the transitions, while the dashed yellow line guides the evolution of the transition $H : n = -1 \rightarrow 0$ as a function magnetic field. Two vertical dashed lines indicate the relevant phonon energies. 35

27 The relative transmission spectra $T(B)/T(0)$ of ultrathin graphite flakes on Scotch tape at selected magnetic fields. The spectra are vertically shifted for clarity. The green lines show the lower branch fitting, and the cyan lines represent the higher branch fitting. The red lines represent the fits using the two-Lorentzian model described by Eq. 48. At a high magnetic field (34 T), a single Lorentzian model is used to fit the spectrum. 36

28 The extracted CR energies and linewidth from the results of the fits to the relative transmission spectra of graphite. (a) CR energy is plotted as a function of magnetic field. The solid lines show the best fits using Eq. 49. The fitting parameters are also presented. (b) Linewidth versus magnetic field. The solid line represents the best linear-in-B fit. 38

29 Relative transmission spectra $T(B)/T(0)$ of graphite around 1580cm^{-1} without CR background. The solid red lines represent the best fits using Eq. 51. The asymmetric lineshape develops from a peak to a dip with increasing magnetic field. 39

30 The extracted E_{ph} energy and linewidth from the Fano fits. (a) E_{ph} is plotted as a function of magnetic field. (b) Linewidth versus magnetic field with fitting (solid black line) using Eq. 49. The solid black lines represent the best fit using Eq. 49. The fitting parameters are also presented. 40

31 Fitting parameters q and A_0 as a function of magnetic field. 41

32 (A) Blue data points show the Landau levels in the tunneling differential conductance spectra versus sample bias in multilayer epitaxial graphene at $B = 5$ T. The red line shows the best fit. (Inset) Landau level peak position versus the square root of Landau level index and magnetic field. (B) Landau level spectra at various magnetic fields. (C) Landau level energies at different magnetic fields (1 T to 8 T) as a function of the square root of Landau level index and magnetic field. The linear fit (solid line) yields a Fermi velocity of $v_F = 1.128 \pm 0.004 \times 10^6$ m/s. Reprinted from Ref. [7]. 44

33 Optical image of epitaxial graphene transistors on SiC substrate. Reprinted from Ref. [8]. 44

34 Band structure of an 11-layer epitaxial graphene on C-face measured by ARPES. Two linear Dirac cones are visible. Reprinted from Ref. [9]. 45

35 Relative transmission spectra of 30-layer epitaxial graphene grown on the C-face of SiC (solid black lines). Solid red lines represent the best fits using Eq. 52. Spectra are vertically shifted for clarity. 46

36 CR energy plotted as a function of $\sqrt{B}$. The solid red line represents the best linear fit using Eq. 54; $v_F = (1.02 \pm 0.01) \times 10^6$ m/s is obtained. 47

37 Linewidth of the CR plotted as a function of $\sqrt{B}$. 48

38 Spectral weight A plotted as a function of $\sqrt{B}$. The solid red line represents the best linear fit to all the data points using Eq. 58. $v_F = 1.93 \times 10^6$ m/s is obtained. 49

39 Relative transmission spectra of epitaxial graphene on Si-face of SiC. The spectra are vertically shifted for clarity. The red solid lines represent the best fits. 52

40 CR energies plotted as a function of magnetic field. Effective mass of $m^* = 0.065 m_0$ is extracted from the linear fit (solid red line). 53

41 (a) σ_B decreases slightly with increasing magnetic field. (b) γ_B remains constant to some extent. 55

42 Top panel: disk array of selectively doped GaAs/AlGaAs heterostructures on GaAs substrate containing the two-dimensional electron gas. The bottom panel: sheet conductance of array as a function of frequency. Magnetic field is perpendicular to the surface. Reprinted with permission from [10]. Copyright (1983) by the American Physical Society [1]. 56

43 (a) Schematics of ribbon array. (b) Relative transmission spectra of ribbon array. The solid lines show the spectra when the light polarization is perpendicular to the ribbon. The dashed lines show the spectra when the light polarization is parallel to the ribbon. Reprinted with permission from [11]. Copyright (1988) by the American Physical Society [1]. 57

44 (a) Relative mid-infrared transmission spectra, T/T_{CNP}, of graphene ribbon array. T_{CNP} is the transmission spectrum of graphene at charge neutral point and T is the spectrum at different gate voltage. The plasmon frequency increases with increasing carrier density. (b) Tune the plasmon energy through the gate voltage. $\Delta T = T - T_{CNP}$. The infrared light was polarized perpendicular to the ribbons. The dashed lines show the best fit using a damped oscillator model as $\mathrm{Im}(-\omega/(\omega^2 - \omega_p^2 + i\omega\Gamma_p))$The inset shows the spectra when the infrared light was polarized parallel to the ribbons. The Drude absorption was observed. (c) AFM images of samples. The widths of ribbons are 1μm, 2μm, and 4μm, respectively. (d) The plasmon frequency varies in graphene ribbons of different width. Reprinted from Ref. [12]. 63

45 (a) Schematics of four graphene ribbon arrays on the substrate. (b) AFM image of 50 nm-wide ribbons. (c) AFM image of 100 nm-wide ribbons. (d) AFM image of 200 nm-wide ribbons. The bright area shows the ribbons and the black part is the gap. The scale bar is 0.6 μm. 65

46 The light is polarized before reaching the sample. The polarization is either parallel or perpendicular to the ribbon direction. 66

47 (a) Relative transmission spectra of 2D graphene film at different magnetic fields. The spectra is vertically shifted for clarity. Inter-Landau-level transition $LL_{-1(0)} \rightarrow LL_{0(1)}$ in multilayer epitaxial graphene on C-face is observed as well as intra-Landau-level transition in graphene on Si-face. The dotted red line represents the Lorentzian fit to the CR resonance lineshape. (b) The CR energy ($LL_{-1(0)} \rightarrow LL_{0(1)}$) is plotted as a function of $\sqrt{B}$. The red solid line represents the best linear fit. . 67

48 Extinct transmission spectra $1-T(GNR)/T(SiC)$ of 100nm-wide GNR array sample. Solid red line shows the spectrum when the electric field of the light is parallel to the ribbon direction while solid black line shows the spectrum with $E \parallel x$. Inset: AFM image of 100nm-wide ribbons. 68

49 Relative transmission spectra $T(B)/T(0)$ of 2D reference sample, 100nm-wide GNR, and 50nm-wide GNR at selective magnetic fields. The spectra of 100nm-wide GNR is scaled by a factor of 10 while the spectra of 50nm-wide GNR is multiplied by 30. The curves are shifted for clarity. 69

50 Relative transmission spectra $T(B)/T(0)$ of GNR arrays consisting of 100nm-wide ribbons with $w/d = 2:1$ (solid black line) and $w/d = 1:1$ (solid red line). The curves are vertically shifted for clarity. The resonance absorption dips almost coincide with each other, revealing no plasmon cross-talk effect. 70

51 (a) ω_h^2 (ω_c^2) plotted as a function of B. The dotted lines show the best fits using Eq. 104 with $v_F = 1.02 \times 10^6$ m/s. (b) UHM energy ω_h in units of v_F/l_B plotted as a function of ql_b. The CR energy ω_c of 2D graphene collapse on a single point (red circle) at $q = 0$. The solid lines represent the best fits to the data using Eq. 104. The dashed green line defined by equation $E = \hbar v_F q$ separates the interband and intraband excitations. 72

52 Inset: The energy shift in units of Coulomb energy in the GNR array sample as a function of ql_B^2. Main panel: Apart form a small offset, the data collapse on a single line. The dotted line and the solid lines represent the best linear fit with $v_F = 1.02 \times 10^6$ m/s. 73

53 (a) Relative transmission spectra of 200nm-wide GNR array with infrared light polarized either parallel or perpendicular to the ribbon direction. (b) Relative transmission spectra of 100nm-wide GNR array with polarized infrared light. The dotted lines represent the best fits using a single Lorentzian model. 75

54 (a) The energy of UHM in units of v_F/l_B plotted as a function of ql_B. (b) The energy shift of UHM with respect to the CR energy in 2D graphene versus ql_B^2. The dotted lines show the best fits using Eq. 103 with $v_F = 1.02 \times 10^6$ m/s. 76

SUMMARY

The graphitic systems have attracted intensive attention recently due to the discovery of graphene, a single layer of graphite. The low-energy band structure of graphene exhibits an unusual linear dispersion relation which hosts massless Dirac fermions and leads to intriguing electronic and optical properties. In particular, due to the high mobility and tunability, graphene and graphitic materials have been recognized as promising candidates for future nanoelectronics and optoelectronics.

Electron-phonon coupling (EPC) plays a significant role in electronic and optoelectronic devices. Therefore, it is crucial to understand EPC in graphitic materials and then manipulate it to achieve better device performance. In the first part of this thesis, we explore EPC between Dirac-like fermions and infrared active phonons in graphite via infrared magneto-spectroscopy. We demonstrate that the EPC can be tuned by varying the magnetic field.

The second part of this thesis deals with magnetoplasmons in quasineutral graphene nanoribbons. Multilayer epitaxial graphene grown on the carbon terminated silicon carbide surface behaves like single layer graphene. Plasmons are excited in the nanoribbons of undoped multilayer epitaxial graphene. In a magnetic field, the cyclotron resonance can couple with the plasmon resonance forming the so-called upper-hybrid mode. This mode exhibits a distinct dispersion relation, radically different from that expected for conventional two dimensional systems.

CHAPTER I

INTRODUCTION

Graphene, a one-atomic thick layer of graphite, is a strictly two-dimensional material with carbon atoms located in a honeycomb structure. It is a basic structural element of other allotropes of carbon, including fullerenes, carbon nanotubes and graphite. Graphene exhibits exceptionally high crystalline and electronic quality, and extraordinary physical properties. Graphene prepared on a silicon substrate with a certain thickness of SiO_2 can be visualized using optical microscopy, which has enabled a rapid increase in experimental research since 2004. An ocean of new physics and potential applications has been revealed.

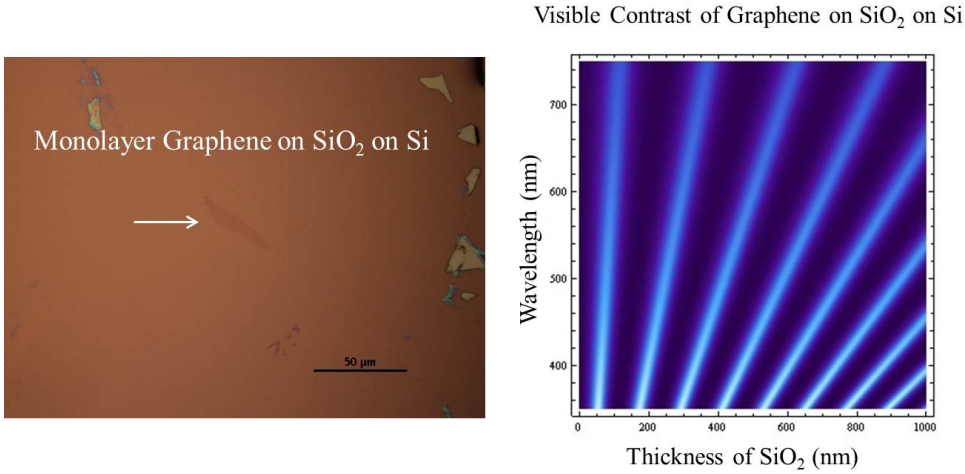

Figure 1: (a) Exfoliated monolayer graphene on 300nm-thick SiO_2 on Si substrate. (b) Contour plot of the visible contrast of graphene on SiO_2 as a function of wavelength and SiO_2's thickness. Calculated based on the method described in Ref. [1].

1.1 The Electronic Properties of Graphene and Graphite

1.1.1 Single Layer Graphene

Graphene is made out of carbon atoms arranged in a hexagonal structure, as shown in Figure 2. The carbon atoms are separated by a distance $a = 1.42$ Å. The three nearest-neighbor vectors in real space are given by

$$\delta_1 = \frac{a}{2}(1, \sqrt{3}),\ \delta_2 = \frac{a}{2}(1, -\sqrt{3}),\ \delta_3 = a(-1, 0). \tag{1}$$

And the six second-nearest neighbors are located at $\delta_1' = \pm\boldsymbol{a}_1$, $\delta_2' = \pm\boldsymbol{a}_2$, $\delta_3' = \pm(\boldsymbol{a}_2 - \boldsymbol{a}_1)$. The structure can be seen as a triangular lattice with a basis of two inequivalent atoms per unit cell. The lattice vectors can be written as

$$\boldsymbol{a}_1 = \frac{a}{2}(3, \sqrt{3}),\ \boldsymbol{a}_2 = \frac{a}{2}(3, -\sqrt{3}). \tag{2}$$

Therefore, the reciprocal-lattice vectors are given by

$$\boldsymbol{b}_1 = \frac{2\pi}{3a}(1, \sqrt{3}),\ \boldsymbol{b}_2 = \frac{2\pi}{3a}(1, -\sqrt{3}). \tag{3}$$

$\mathbf{K}$=$(\frac{2\pi}{3a}, \frac{2\pi}{3\sqrt{3}a})$ and $\mathbf{K}'$=$(\frac{2\pi}{3a}, -\frac{2\pi}{3\sqrt{3}a})$ are the inequivalent corners of the Brillouin zone and are called Dirac points. Later we will show that these Dirac points are of great importance to the electronic properties of graphene.

In the tight-binding approach, we consider that electrons can hop to both nearest atoms and second-nearest neighbors. Then, the Hamiltonian for electrons in graphene has the form [13]

$$H = -t \sum_{<i,j>,\sigma} (a^\dagger_{\sigma,i} b_{\sigma,j} + \mathbf{H}.c.) - t' \sum_{<i,j>,\sigma} (a^\dagger_{\sigma,i} a_{\sigma,j} + b^\dagger_{\sigma,i} b_{\sigma,j} + \mathbf{H}.c.), \tag{4}$$

where $a_{i,\sigma}$ ($a^\dagger_{i,\sigma}$) annihilates (creates) an electron with spin σ ($\sigma =\uparrow, \downarrow$) on site $\mathbf{R}_i$ on the sublattice A. For sublattice B, we can get an equivalent equation. Here, $t \approx 2.8$ eV is the nearest-neighbor hopping energy and t' is the next nearest-neighbor hopping energy. The value of t' is not well known. $0.02t \leq t' \leq 0.2t$ is found based

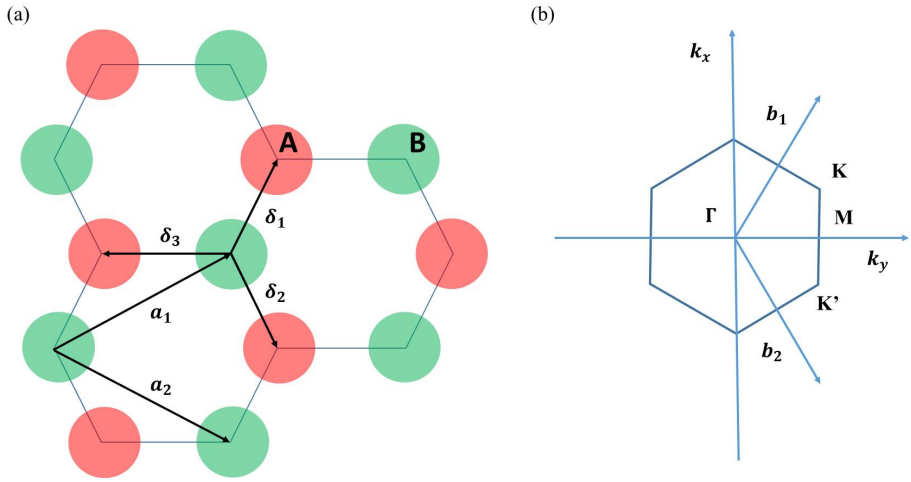

Figure 2: Honeycomb lattice and its Brillouin zone. (a) Lattice structure of graphene. $\boldsymbol{a}_1$ and $\boldsymbol{a}_2$ are the lattice unit vector, and δ_i, $i = 1, 2, 3$ are the nearest-neighbor vectors. (b) Corresponding Brillouin zone. Dirac cones are at the $\mathbf{K}$ and $\mathbf{K}'$ points.

on the *ab initio* calculations [14] and $t' \approx 0.1$ eV is extracted from the tight-binding fit to cyclotron resonance in experiments [15]. The energy bands derived from this Hamiltonian have the form [16]

$$\begin{aligned} E_{\pm}(\mathbf{k}) &= \pm t\sqrt{3 + f(\mathbf{k})} - t' f(\mathbf{k}), \\ f(\mathbf{k}) &= 2\cos(\sqrt{3}k_y a) + 4\cos(\frac{\sqrt{3}}{2}k_y a)\cos(\frac{3}{2}k_x a), \end{aligned} \tag{5}$$

where the plus and minus signs apply to the conduction band (upper, π^*) and the valence band (lower, π), respectively. Close to the Dirac points ($\mathbf{K}$ or $\mathbf{K}'$), we can approximate t' equals zero in the long wavelength limit. Then the graphene band dispersion at $\mathbf{K}$, for instance, can be simplified. Let $\mathbf{k} = \mathbf{K} + \mathbf{q}$ with $|\mathbf{q}| \ll \mathbf{K}$, the dispersion can be written as [13, 14, 17, 18, 19]

$$E_{\pm}(\boldsymbol{q}) \approx \pm v_F |\mathbf{q}| + O[(q/K)^2], \tag{6}$$

where $\mathbf{q}$ is the momentum with respect to the Dirac point $\mathbf{K}$ and $v_F = 3ta/2 \simeq 1 \times 10^6$ m/s is the Fermi velocity. What is most surprising is that the Fermi velocity in Eq. 6 is independent of energy or momentum. In the usual case, $v = k/m = \sqrt{2E/m}$ changes with energy. If we take t' into consideration, the dispersion near the Dirac

points can be written as

$$E_{\pm} \simeq 3t' \pm v_F|\mathbf{q}| - (\frac{9t'a^2}{4} \pm \frac{3ta^2}{8}\sin(3\theta_{\mathbf{q}}))|\mathbf{q}|^2, \tag{7}$$

where

$$\theta_{\mathbf{q}} = \arctan(\frac{q_x}{q_y}). \tag{8}$$

Therefore, t' shifts the position of the Dirac point in energy and breaks the electron-hole symmetry leading to asymmetric π and π^* bands as shown in Figure 3 (a).

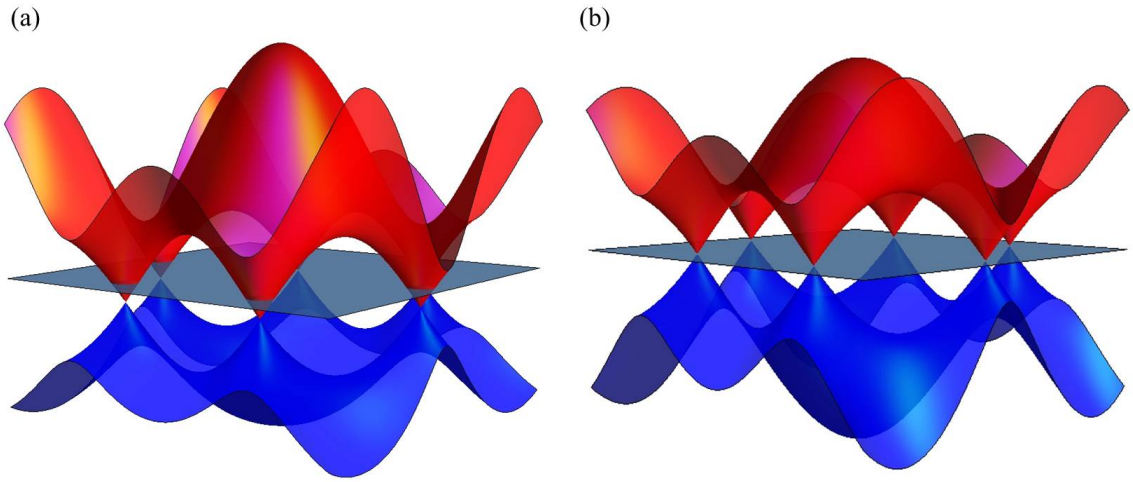

Figure 3: Calculated electronic dispersion of graphene using Eq. 5. E is in units of t. (a) Energy spectrum in units of t, with $a = 1.42\,\text{Å}$ and $t' = -0.1t$. The plane is located at $E = 0$. (b) Energy spectrum with $t' = 0$. The energy bands close to the Dirac points are linear.

The most important aspect of graphene's energy dispersion is its linear energy momentum relationship close to Dirac points as indicated in Eq. 6. The conductance band and the valence band intersect at $q = 0$. The Dirac cones for electrons and holes touch each other with no energy gap. Graphene is thus a zero band-gap semiconductor with a linear, rather than quadratic, low-energy dispersion for both electrons and holes.

We consider Eq. 4 with $t' = 0$ and the Fourier transform of the electron operators,

$$a_n = \frac{1}{\sqrt{N_c}} \sum_{\boldsymbol{k}} e^{-i\boldsymbol{k}\cdot\boldsymbol{R}_n} a(\boldsymbol{k}) \tag{9}$$

where N_c is the number of unit cells. According to Eq. 9, we expand the Fourier sum around $\mathbf{K}$ and $\mathbf{K}'$ and get an approximate representation of the field a_n as a sum of two new fields,

$$\begin{aligned} a_n &\simeq e^{-i\boldsymbol{K}\cdot\boldsymbol{R}_n} a_{1,n} + e^{-i\boldsymbol{K'}\cdot\boldsymbol{R}_n} a_{2,n}, \\ b_n &\simeq e^{-i\boldsymbol{K}\cdot\boldsymbol{R}_n} b_{1,n} + e^{-i\boldsymbol{K'}\cdot\boldsymbol{R}_n} b_{2,n}, \end{aligned} \tag{10}$$

where $i = 1, 2$ refer to the $\mathbf{K}$ and $\mathbf{K}'$ points, respectively. The new fields $a_{i,n}$ and $b_{i,n}$, are assumed to vary slowly over the unit cell. Using Eq. 10 in the tight-binding approach and expanding the operators to the linear order in $\boldsymbol{\delta}$ with the fact that $\sum_\delta e^{\pm i\boldsymbol{K}\cdot\delta} = \sum_\delta e^{\pm i\boldsymbol{K'}\cdot\delta} = 0$, we will get [20]

$$\begin{aligned} H \simeq -t \int dxdy \hat{\Psi}_1^\dagger(\boldsymbol{r}) \Bigg[\begin{pmatrix} 0 & 3a(1-i\sqrt{3})/4 \\ -3a(1+i\sqrt{3}/4) & 0 \end{pmatrix} \partial x \\ + \begin{pmatrix} 0 & 3a(-i-\sqrt{3})/4 \\ -3a(i-\sqrt{3}/4) & 0 \end{pmatrix} \partial y \Bigg] \hat{\Psi}_1(\boldsymbol{r}) \\ + \hat{\Psi}_2^\dagger(\boldsymbol{r}) \Bigg[\begin{pmatrix} 0 & 3a(1+i\sqrt{3})/4 \\ -3a(1-i\sqrt{3}/) & 0 \end{pmatrix} \partial x \\ + \begin{pmatrix} 0 & 3a(i-\sqrt{3})/4 \\ -3a(-i-\sqrt{3}/4) & 0 \end{pmatrix} \partial y \Bigg] \hat{\Psi}_2(\boldsymbol{r}) \\ = -iv_F \int dxdy \Bigg[\hat{\Psi}_1^\dagger(\boldsymbol{r}) \sigma\cdot\nabla \hat{\Psi}_1(\boldsymbol{r}) + \hat{\Psi}_2^\dagger(\boldsymbol{r}) \sigma^*\cdot\nabla \hat{\Psi}_2(\boldsymbol{r}) \Bigg], \end{aligned} \tag{11}$$

where $\sigma = (\sigma_x, \sigma_y)$, $\sigma^* = (\sigma_x, -\sigma_y)$ are the Pauli matrices and $\hat{\Psi}_i^\dagger = (a_i^\dagger, b_i^\dagger)$ $(i = 1, 2)$. Apparently, Eq. 11 is made of two massless Dirac-like Hamiltonians, one is for $\boldsymbol{p}$ around $\mathbf{K}$ and the other for $\boldsymbol{p}$ around $\mathbf{K}'$. The two-component electron wave function $\psi(\boldsymbol{r})$ close to the $\mathbf{K}$ point obeys the 2D Dirac equation,

$$-iv_F \sigma\cdot\nabla\psi(\boldsymbol{r}) = E\psi(\boldsymbol{r}). \tag{12}$$

In the momentum space, the wave function for the momentum around **K** has the form

$$\psi_{\pm,\mathbf{K}}(\mathbf{q}) = \frac{1}{\sqrt{2}} \begin{pmatrix} e^{-i\theta_{\boldsymbol{q}}/2} \\ \pm e^{i\theta_{\boldsymbol{q}}/2} \end{pmatrix} \tag{13}$$

for $H_K = v_F \boldsymbol{\sigma} \cdot \mathbf{k}$, where the $\pm$ signs correspond to the eigenenergies $E = \pm v_F q$ for the conduction π^* band and valence π band, respectively. $\theta_{\boldsymbol{q}}$ is defined by Eq. 8. The wave function for the momentum around $\mathbf{K}'$ has the form

$$\psi_{\pm,\mathbf{K}'}(\mathbf{q}) = \frac{1}{\sqrt{2}} \begin{pmatrix} e^{i\theta_{\boldsymbol{q}}/2} \\ \pm e^{-i\theta_{\boldsymbol{q}}/2} \end{pmatrix} \tag{14}$$

for $H_{K'} = v_F \boldsymbol{\sigma}^* \cdot \mathbf{k}$. The wave functions at **K** and $\mathbf{K}'$ are related by time-reversal symmetry. Also the sign of the wave functions will change when the phase θ is rotated by 2π indicating that the Berry's phase is π [21], which is the characteristic of spinors. The helicity is defined as the projection of the momentum operator along the spin direction. The quantum-mechanical operator for the helicity has the form

$$\hat{h} = \frac{1}{2} \boldsymbol{\sigma} \cdot \frac{\boldsymbol{p}}{|\boldsymbol{p}|}. \tag{15}$$

From the above equation, it is clear that the states $\psi_{\boldsymbol{K}}(\boldsymbol{r})$ and $\psi_{\boldsymbol{K'}}(\boldsymbol{r})$ are the eigenstates of $\hat{h}$,

$$\begin{aligned} \hat{h}\psi_{\boldsymbol{K}}(\boldsymbol{r}) &= \pm\frac{1}{2}\psi_{\boldsymbol{K}}(\boldsymbol{r}), \\ \hat{h}\psi_{\boldsymbol{K'}}(\boldsymbol{r}) &= \mp\frac{1}{2}\psi_{\boldsymbol{K'}}(\boldsymbol{r}). \end{aligned} \tag{16}$$

Therefore, electrons have a positive helicity while holes have a negative helicity. Eq. 16 indicates that $\boldsymbol{\sigma}$ has two eigenvalues either in the direction $\uparrow$ or in the direction $\downarrow$. This property shows that the states of the system close to the Dirac point have well defined *chirality* or *helicity*.

1.1.2 Bilayer Graphene

Unlike the monolayer graphene with conduction band and valence band touching at Dirac points, the bilayer graphene has the energy gap open with external electric field.

The tight-binding model can be extended to study the electronic structure of bilayer graphene [22]. The crystal structure of bilayer graphene with AB stacking is shown in Figure 4. The tight-binding Hamiltonian for bilayer graphene can be written as

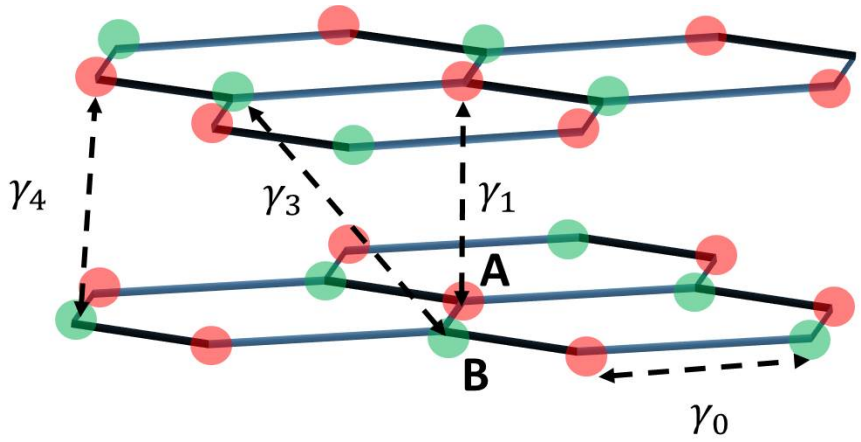

Figure 4: Lattice structure of bilayer graphene with various hopping energies. The A atoms are over each other while the B atoms are displaced with respect to each other. The Slonczewski-Weiss-McClure (SWM) parameters are labeled as γ_0, γ_1, γ_3,and γ_4.

[13]

$$
\begin{aligned}
h_{t.b.} = & -\gamma_0 \sum_{<i,j>} (a^{\dagger}_{m,i,\sigma} b_{m,j,\sigma} + \mathbf{H}.c.) \\
& - \gamma_1 \sum_{<j,\sigma>} (a^{\dagger}_{1,j,\sigma} a_{2,j,\sigma} + \mathbf{H}.c.) \\
& - \gamma_3 \sum_{<j,\sigma>} (b^{\dagger}_{1,j,\sigma} b_{2,j,\sigma} + \mathbf{H}.c.) \\
& - \gamma_4 \sum_{<j,\sigma>} (a^{\dagger}_{1,j,\sigma} b_{2,j,\sigma} + a^{\dagger}_{2,j,\sigma} b_{1,j,\sigma} + \mathbf{H}.c.),
\end{aligned}
\tag{17}
$$

where $a_{m,i,\sigma}$ ($b_{m,i,\sigma}$) annihilates an electron with spin σ on sublattice A (B). $m = 1, 2$ represent the different graphite layers at site $\mathbf{R}_i$. As shown in Figure 4, $\gamma_0 = t$ is the in-plane hopping energy. $\gamma_1 = t_{\perp} \approx 0.4$ eV, $\gamma_3 \approx 0.3$ eV, and $\gamma_4 \approx 0.04$ eV correspond to the hopping energies between atom A_1 and atom A_2, B_1 and B_2, A_1 (A_2) and B_2 (A_2), respectively [23, 24].

In the continuum limit, by expanding the momentum $\mathbf{k}$ around the $\mathbf{K}$ point, the

Hamiltonian can be written as

$$H = \sum_{\mathbf{k}} \Psi^{\dagger}_{\mathbf{k}} \cdot H_{\mathbf{K}} \cdot \Psi_{\mathbf{k}}, \tag{18}$$

where

$$H_{\mathbf{K}} = \begin{pmatrix} -V & v_F k & 0 & 3\gamma_3 a k^* \\ v_F k^* & -V & \gamma_1 & 0 \\ 0 & \gamma_1 & V & v_F k \\ 3\gamma_3 a k & 0 & v_F k^* & V \end{pmatrix}, \tag{19}$$

with $\gamma_4 = 0$. $k = k_x + ik_y$ is a complex number. V is half the shift in electrochemical potential between two graphite layers.

$$\Psi^{\dagger}_{\mathbf{k}} = (b^{\dagger}_1(\mathbf{k}), a^{\dagger}_1(\mathbf{k}), a^{\dagger}_2(\mathbf{k}), b^{\dagger}_2(\mathbf{k})) \tag{20}$$

is a four-component spinor.

If $V = 0$ and γ_3, $v_F k \ll \gamma_1$, the Hamiltonian can be simplified to

$$H = \begin{pmatrix} 0 & v_F^2 k^2/\gamma_1 + 3\gamma_3 a k^* \\ v_F^2 (k^*)^2/\gamma_1 + 3\gamma_3 a k & 0 \end{pmatrix}. \tag{21}$$

If $\gamma_3 = 0$, two parabolic bands, $E_{k,\pm} \approx \pm v_F^2 k^2/t_\perp$, will derive from Eq. 21. These two bands will touch each other at $E = 0$ as shown Figure 5 (a). If $V \neq 0$, the equivalence of the two layers will be broken. In this case, the energy dispersion reads

$$E^2_{\pm,\mathbf{k}} = V^2 + v_F^2 k^2 + t_\perp^2/2 \pm \sqrt{4V^2 v_F^2 k^2 + t_\perp^2 v_F^2 k^2 + t_\perp^4/4}. \tag{22}$$

As we can see in Figure 5 (b), an energy gap is opened close to the **K** point. For $V \ll t$ and small k, Eq. 22 can be simplified to

$$\begin{aligned} E_{+,k} &\approx V - 2V v_F^2 k^2/t_\perp + v_F^4 k^4/2t_\perp^2 V, \\ E_{-,k} &\approx -V + 2V v_F^2 k^2/t_\perp - v_F^4 k^4/2t_\perp^2 V. \end{aligned} \tag{23}$$

The energy gap is at $k^2 \approx 2V^2/v_F^2$. Therefore, the position depends on the bias V and can be measured experimentally [22, 25, 26, 27]. The presence of an energy gap makes the bilayer graphene suited for practical application.

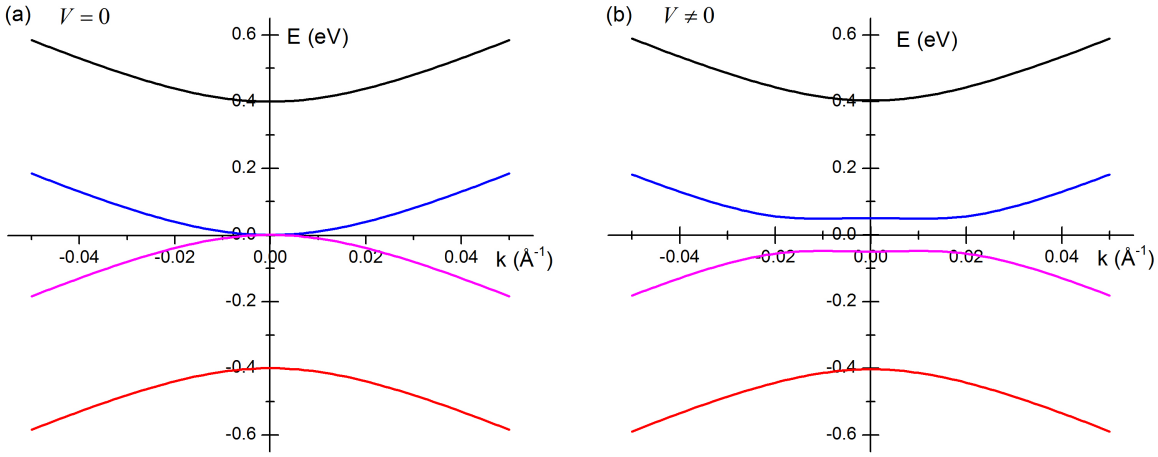

Figure 5: Calculated band structure of bilayer graphene using Eq. 22 with $v_F = 10^6\,\mathrm{m/s}$ and $t_\perp = 0.4\,\mathrm{eV}$. (a) Band structure of bilayer graphene for $V = \gamma_3 = 0$. (b) Band structure of bilayer graphene for $V = 0.05\,\mathrm{eV}$ and $\gamma_3 = 0$.

1.1.3 Bulk Graphite

Graphite consists of graphene layers coupled by the van der Waals force. As we can see in Figure 6 (a), every other graphene layer is shifted in the horizontal plane, which is known as AB stacking. The spacing between the nearest neighbors in the same layer is $a_0 = 1.42\,\text{Å}$. The layers are separated by $c_0 = 3.37\,\text{Å}$. Figure 6 (b) shows the Brillouin zone in momentum space. The electronic band dispersion of graphite was calculated by Wallace and others (Slonczewski, Weiss, and McClure) [16, 17, 18] in 40s and 50s with the tight-binding approach. This model is known as Slonczewski-Weiss-McClure (SWMc) band theory and has been used to understand graphitic materials ever since its establishment. If we only keep the first nonvanishing k_z-dependent term, the Hamiltonian for electrons in graphite can be written as

$$H = \begin{pmatrix} E_1 & 0 & H_{13} & H_{13}^* \\ 0 & E_2 & H_{23} & -H_{23}^* \\ H_{13}^* & H_{23}^* & E_3 & H_{33} \\ H_{13} & -H_{23} & H_{33}^* & E_3 \end{pmatrix}, \tag{24}$$

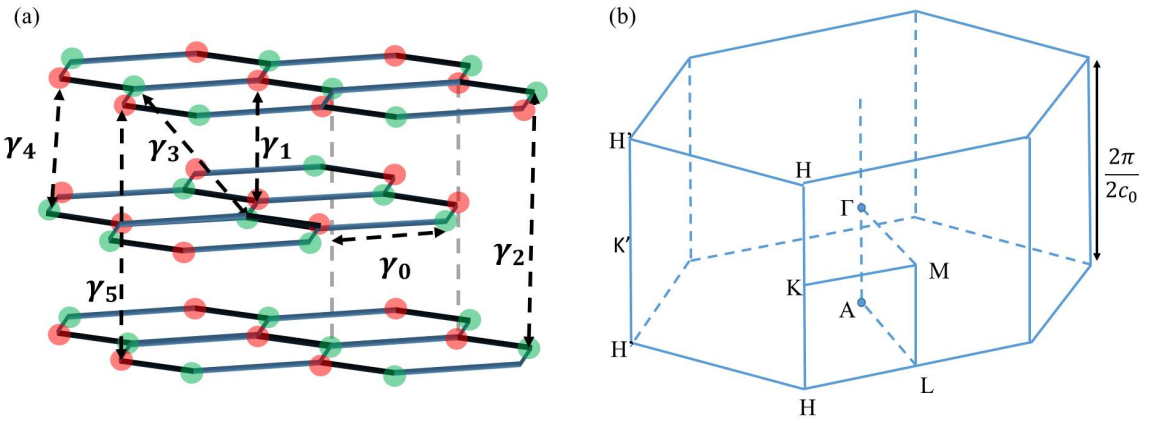

Figure 6: (a) Crystal structure of bulk graphite. The graphene layers are stacked in AB order. $\gamma_i\,(i = 1, ..., 5)$ defines the hopping energy. (b) Brillouin zone of bulk graphite.

where

$$
\begin{aligned}
&E_1 = \gamma_1\Gamma + \Delta + \frac{1}{2}\gamma_5\Gamma^2,\\
&E_2 = -\gamma_1\Gamma + \Delta + \frac{1}{2}\gamma_5\Gamma^2,\\
&E_3 = \gamma_2(1+\cos\xi) = \frac{1}{2}\gamma_2\Gamma^2,\ \xi = k_z c_0,\ \Gamma = 2\cos(\frac{1}{2}\xi),\\
&H_{13} = 2^{-1/2}(-\gamma_0 + \gamma_4\Gamma)\sigma e^{i\alpha},\ \alpha = \tanh(-k_x/k_y),\ \sigma = \frac{3}{2}a_0|\mathbf{k}|,\\
&H_{23} = 2^{-1/2}(\gamma_0 + \gamma_4\Gamma)\sigma e^{i\alpha},\\
&H_{33} = \gamma_3\Gamma\sigma e^{i\alpha}.
\end{aligned}
\tag{25}
$$

First we ignore γ_3 and γ_4 and get the energy

$$
\begin{aligned}
E &= \frac{1}{2}(E_1 + E_3) \pm [\frac{1}{4}(E_1 - E_3)^2 + \gamma_0^2\sigma^2]^{1/2},\\
E &= \frac{1}{2}(E_2 + E_3) \pm [\frac{1}{4}(E_2 - E_3)^2 + \gamma_0^2\sigma^2]^{1/2}.
\end{aligned}
\tag{26}
$$

The dependence of E on σ is called "hyperbolic" by Slonczewski and Weiss [18] compared to the more familiar "arabolic" dependence. If we include γ_3 and γ_4, we can not get an analytical solution for all $\mathbf{k}$. However, for certain planes in k space where $\alpha = \frac{1}{3}n\pi$, we can obtain the energy

$$
E = \frac{1}{2}(E_2 + E_3 - \gamma_3\Gamma\sigma\cos 3\alpha) \pm [\frac{1}{4}(E_2 - E_3 + \gamma_3\Gamma\sigma\cos 3\alpha)^2 + (\gamma_0 + \gamma_4\Gamma)^2\sigma^2]^{1/2}. \tag{27}
$$

In the case that E_1 and E_2 are well separated from E_3, by the perturbation theory, we find

$$E = E_3 + A\sigma^2 \pm [B^2\sigma^4 + 2B\sigma^3\gamma_3\Gamma\cos 3\alpha + \sigma^2\gamma_3^3\Gamma^2]^{1/2} \tag{28}$$

where

$$\begin{aligned} A &= \frac{1}{2}\left[\frac{(\gamma_0 - \gamma_4\Gamma)^2}{E_3 - E_1} + \frac{(\gamma_0 + \gamma_4\Gamma)^2}{E_3 - E_2}\right], \\ B &= \frac{1}{2}\left[\frac{(\gamma_0 + \gamma_4\Gamma)^2}{E_3 - E_2} - \frac{(\gamma_0 - \gamma_4\Gamma)^2}{E_3 - E_1}\right]. \end{aligned} \tag{29}$$

As we can see, the tight-binding parameters γ_i play a key role in the SWMc model. The physical representations and estimated values of these parameters have been illustrated and organized by Dresselhaus *et al.* [28] and Zhang *et al.* [29]. Recently, these parameters excluding γ_3 have been measured using the high-field magnetoreflectance on graphite [4].

1.2 Magnetic Field Effect

In the case that a strong external magnetic field is applied, the cyclotron orbits of carriers in materials will be quantized, leading to the quantized energy levels E_n which are the so-called Landau levels (LLs). A new length scale named magnetic length is also introduced as

$$l_B = \sqrt{\frac{\hbar}{eB}}, \tag{30}$$

where e is the electron charge, and $\hbar$ is Planck's constant.

1.2.1 Landau levels in Monolayer Graphene

The Landau levels of massless Dirac fermions in monolayer graphene read [30, 31, 32]

$$E_n = sgn(n)v_F\sqrt{2e\hbar B|n|},\ n = 0, \pm 1, \pm 2, ... \tag{31}$$

where v_F is the Fermi velocity, and the integer n represents an electron-like ($n > 0$) or a hole-like ($n < 0$) index. What is most interesting is the appearance of an $n = 0$

Landau level at the Dirac point due to the exceptional band structure of the graphene. The $n = 0$ Landau level leads to unusual quantum Hall effect of which experimental evidence was first reported in 2005 by two different groups, one led by Andre Geim and the other led by Philip Kim [21, 33]. The discovery is recognized as a major milestone in the experimental and theoretical study of graphene.

Another interesting fact of the Landau levels is that the energy spectrum has a $\sqrt{B}$ dependence different from linear B dependence in conventional two-dimensional electron systems as shown in Figure 7. The transitions between Landau levels give rise

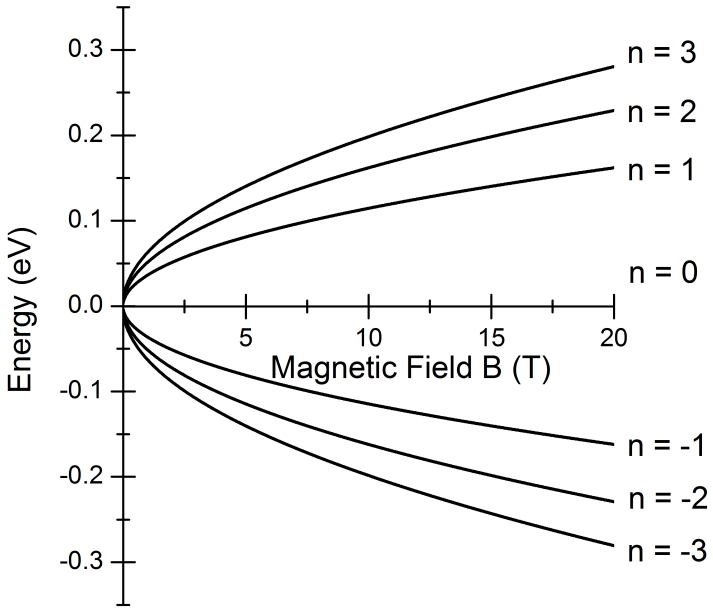

Figure 7: Numerically calculated Landau levels of monolayer graphene as a function of magnetic field. Here, $e = 1.6 \times 10^{-19}$C, $\hbar = 1.05 \times 10^{-34}\,\mathrm{J \cdot s}$, and $v_F = 10^6$ m/s.

to the cyclotron resonance. In monolayer graphene, the cyclotron resonance frequency is given by

$$\omega_c = v_F\sqrt{2e\hbar B}|\mathrm{sgn}(n+1)\sqrt{n+1} - \mathrm{sgn}(n)\sqrt{n}|, \tag{32}$$

while in a conventional two-dimensional electron gas [34],

$$\omega_c = \frac{eB}{m^*}. \tag{33}$$

Here, m^* is the effective mass of the carriers. This $\sqrt{B}$ dispersion of transitions

between Landau levels has been observed experimentally in infrared transmission spectroscopy as shown in Figure 8 [2, 15, 35, 36, 37, 38, 39].

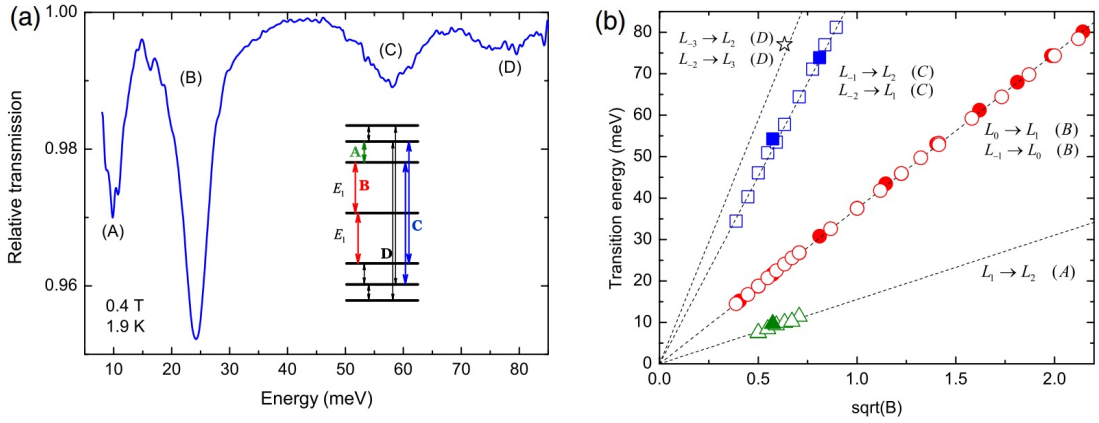

Figure 8: Transitions between Landau levels in monolayer graphene. (a) Relative transmission spectrum at 0.4 T and 1.9 K shows four transitions. (b) The observed transitions plotted as a function of B. The solid symbols are data obtained from the measurement and the dashed lines represent the best fits with Fermi velocity $v_F = 1.03 \times 10^6\, m/s$. Reprinted from Ref.[2].

1.2.2 Bilayer Graphene and Graphite

In the bilayer graphene, the Landau energy reads [3, 5, 40, 41, 42, 43]

$$E_n = \frac{sgn(n)}{\sqrt{2}}[(2|n|+1)\Delta^2 + \gamma_1^2 \pm \sqrt{\gamma_1^4 + 2(2|n|+1)\Delta^2\gamma_1^2 + \Delta^4}]^{1/2}. \quad (34)$$

Here, γ_1 is the interlayer coupling energy. Δ is the magnetic energy defined by

$$\Delta = v_F\sqrt{2\hbar eB}, \quad (35)$$

which is equal to the Landau level energy $E_{n=\pm1}$ of monolayer graphene. "$\pm$" correspond to the higher and lower subbands in the zero magnetic field, respectively. The index $n = \pm1, \pm2, ...$ describes a set of Landau levels. B represents the magnetic field. In each subband (lower or higher), the LLs are fourfold degenerate due to the spin and valley degeneracies. The unusual $n = 0$ LL is eightfold degenerate. If $\gamma_1 = 0$, Eq. 34 will give the LL energies of monolayer graphene.

Figure 9 shows the numerically calculated Landau levels as a function of magnetic field in bilayer graphene. Measurement of cyclotron resonance in bilayer graphene has

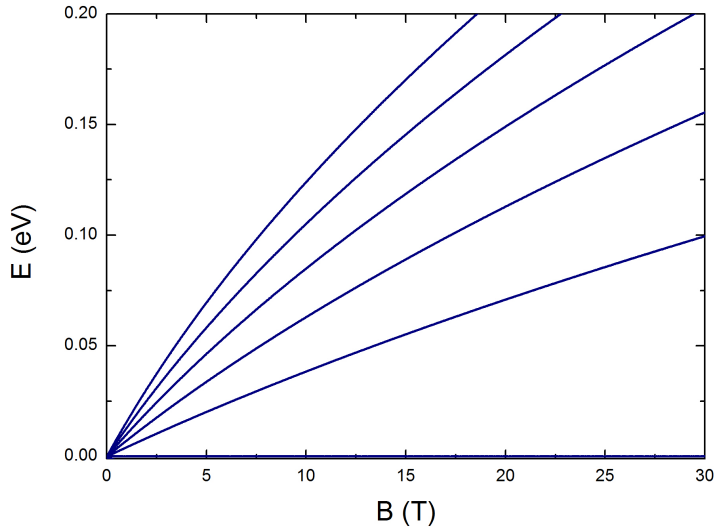

Figure 9: Landau levels in the bilayer graphene as a function of the magnetic field using Eq. 34. Here, $e = 1.6 \times 10^{-19}$C, $\hbar = 1.05 \times 10^{-34}$ J $\cdot$ s, $v_F = 10^6$m/s, and $t = 0.4$ eV.

also been reported [3, 5]. Figure 10 shows the infrared transmission spectra of bilayer graphene. The transitions between Landau levels are evidenced in the measurement [3].

In the bulk graphite, Landau energies E_n satisfy the following equations [44, 45]

$$\begin{aligned}(n+\frac{1}{2})\boldsymbol{B} =& \frac{E_n - E_3}{2}\left(\frac{E_n - E_1}{(1-\nu)^2} + \frac{E_n - E_2}{(1+\nu)^2}\right) \\ & \pm \{[\frac{E_n - E_3}{2}\left(\frac{E_n - E_1}{(1-\nu)^2} - \frac{E_n - E_2}{(1+\nu)^2}\right)]^2 + \frac{\boldsymbol{B}^2}{4}\}^{1/2},\end{aligned} \tag{36}$$

where $\boldsymbol{B} = \frac{3a^2\gamma_0^2}{2\hbar}eB$ and $\nu = \frac{\gamma_4\Gamma}{\gamma_0}$. $a_0 = 2.42\,\text{Å}$ is the lattice parameters of graphite. E_1, E_2, and E_3 are the same as defined in Eq. 25. Figure 11 shows numerically calculated LLs of graphite as a function of k_z along the K-H direction.

The Landau levels in bilayer graphene and graphite are calculated based on the simple nearest-neighbor tight-binding model. Because graphite consists of graphene layers, we can find some connections between Landau levels of graphite and those of

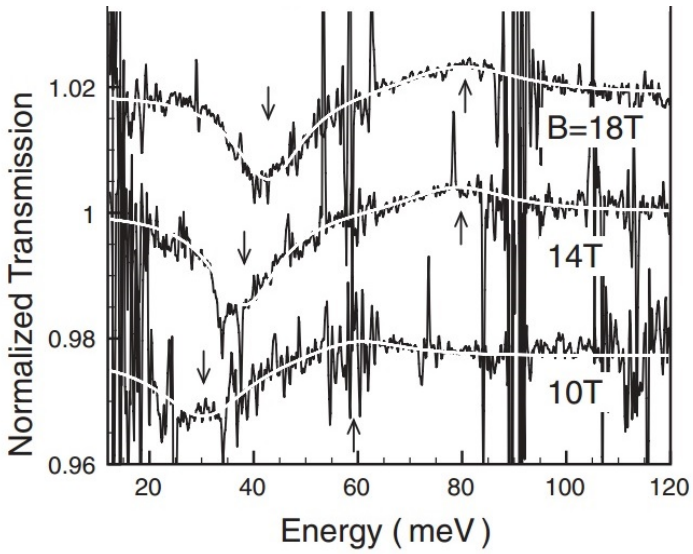

Figure 10: Normalized infrared transmission spectra of bilayer graphene. The resonance dips are due to the intraband transitions. Picture adapted from [3].

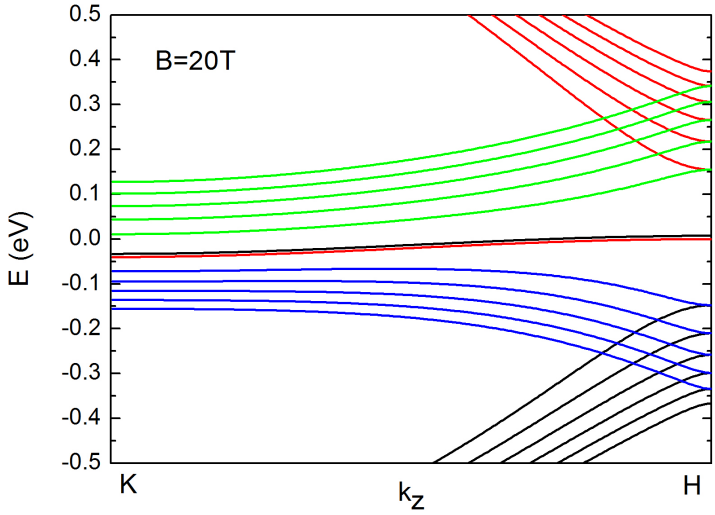

Figure 11: Numerically calculated LLs in graphite at $B = 20\,\mathrm{T}$ as a function of k_z. Here, $\gamma_0 = 2.88\,\mathrm{eV}$, $\gamma_1 = 0.38\,\mathrm{eV}$, $\gamma_2 = -0.02\,\mathrm{eV}$, $\gamma_3 = 0$, $\gamma_4 = 0.072\,\mathrm{eV}$, $\gamma_5 = 0.028\,\mathrm{eV}$, and $\Delta = 0.0075\,\mathrm{eV}$ [4].

graphene. At the K point of the graphite Brillouin zone, the subbands of graphite are equivalent to those of the bilayer graphene with the interlayer coupling energy

doubled: $2\gamma_1$ instead of γ_1, which gives rise to [45, 42]

$$E_n = \frac{sgn(n)}{\sqrt{2}}[(2|n|+1)\Delta^2 + (2\gamma_1)^2 \pm \sqrt{(2\gamma_1)^4 + 2(2|n|+1)\Delta^2(2\gamma_1)^2 + \Delta^4}]^{1/2}. \quad (37)$$

Eq. 37 indicates linear-in-B dependence of Landau levels in the low energy regime, $E_n \ll 2\gamma_1$. At the H point of the graphite Brillouin zone, the spectrum corresponds to the Dirac fermions [45] due to the effectively vanishing interlayer coupling which leads to the same expression as Eq. 31. Figure 12 exhibits an infrared transmission study of thin flakes of graphite in magnetic fields up to $B = 34$ T. Two series of Landau-level transitions are both evidenced. One series scales as $\sqrt{B}$ resulting from massless holes at the H point while the other one scales as B corresponding to the transitions of massive electrons in the vicinity of the K point [5].

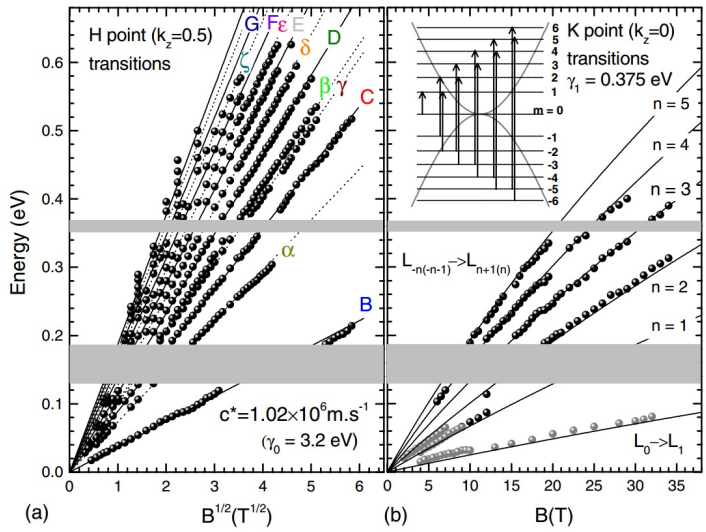

Figure 12: (a) Landau-level transitions related to the H point as a function of $\sqrt{B}$. The solid and dashed lines represent expected results calculated using Eq. 31 with $v_F = 1.02 \times 10^6$ m/s. (b) Landau-level transitions related to the K point as a function of B. The solid lines show expected dipole-allowed transitions calculated using Eq. 37 with $\gamma_0 = 3.2$ eV and $\gamma_1 = 0.375$ eV. Grey data points were taken on highly oriented pyrolytic graphite, which exhibit a behavior nearly identical to natural graphite. The inset schematically shows the observed interband transitions in the effective bilayer. Reprinted from Ref. [5].

1.3 Outline of the Thesis

This thesis presents the infrared magneto-spectroscopy study of graphite and graphene nanoribbons. Chapter 2 will introduce the experimental techniques employed in this work, including Fourier transform infrared spectroscopy, sample fabrication methods, and sample characterization. Chapter 3 will focus on the infrared magneno-spectroscopy measurement on ultrathin graphite flakes. The electron-phonon coupling in graphite is discussed. Chapter 4 will present the infrared magneto-spectroscopy measurement on graphene nanoribbon array. The upper hybrid mode due to coupling between the plasmon mode and cyclotron resonance mode is explored.

CHAPTER II

EXPERIMENTAL TECHNIQUES

2.1 Fourier Transform Infrared Spectroscopy

2.1.1 Introduction

The infrared (IR) spectral range is from 12800 cm^{-1} to 10 cm^{-1}. It was discovered back in the 19th century by astronomer William Herschel [46]. Since then, scientists have tried various ways to make use of infrared light. Infrared spectroscopy realized by spectrometers has been used in materials analysis for over 70 years. It can result in a positive identification of different materials. The Fourier Transform Infrared (FTIR) spectrometer is the latest generation. Compared to the previous infrared spectrometers, FTIR spectrometers have several prominent advantages: (1) It can increase sensitivity - scans can be co-added together to ratio out random noise. Therefore, the signal-to-noise ratio of the spectrum is extremely high. (2) It can increase the speed - one scan over all frequencies per second. (3) The resolution is extremely high (0.1 $\sim$ 0.005 cm^{-1}). (4) The accuracy of wavenumber is high with the error in the range of $\pm$ 0.01 cm^{-1}.

A common FTIR spectrometer consists of an infrared light source (mercury lamp, for example), interferometer, sample compartment, detector, and a computer. Figure 13 shows the block diagram of an FTIR spectrometer. The radiation generated by the light source passes through the aperture which controls the amount of energy presented to the sample. The infrared light enters the interferometer and the interferogram signal is output. Then the beam enters the sample compartment where it is transmitted through or reflected off of the sample. Specific frequencies of energy are absorbed, giving rise to the uniquely characteristic spectrum of the sample. The

beam finally reaches the detector which is used to measure the interferogram signal. The measured signal is sent to the computer and Fourier transformed to a spectrum.

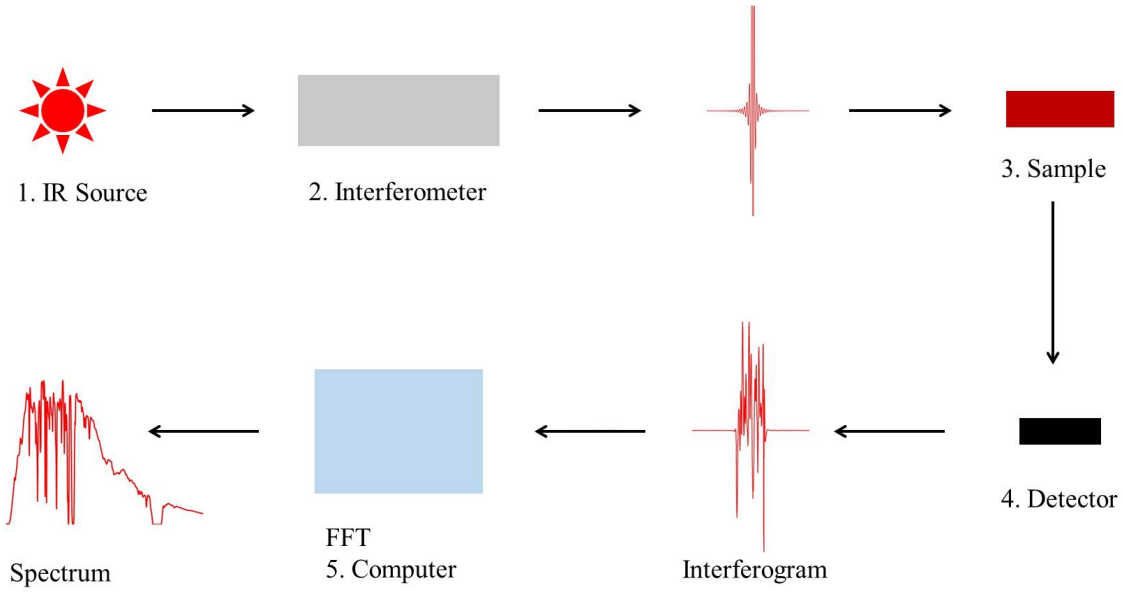

Figure 13: The block diagram of an FTIR spectrometer

A key component of an FTIR spectrometer is the interferometer as shown in Figure 14. Most interferometers employ a beamsplitter. The beamsplitter divides the incoming infrared beam into two. One beam is reflected by a flat mirror fixed in place and the other beam is reflected by a movable flat mirror which can move away from the beamsplitter. The two beams reflected by their respected mirror are recombined at the beamsplitter. Because the path that one beam travels is fixed and the other is changing as the mirror moves, the two beams will interfere with each other producing the so-called interferogram. The interferogram is a plot of the intensity of signal as a function of optical path difference p and it is in the space domain. A Fourier transform converts the interferogram to an infrared spectrum in the wavenumber domain as shown in Figure 15.

The Fourier transform infrared technique has brought significant practical advantages to infrared spectroscopy. The measurements made by FTIR are extremely

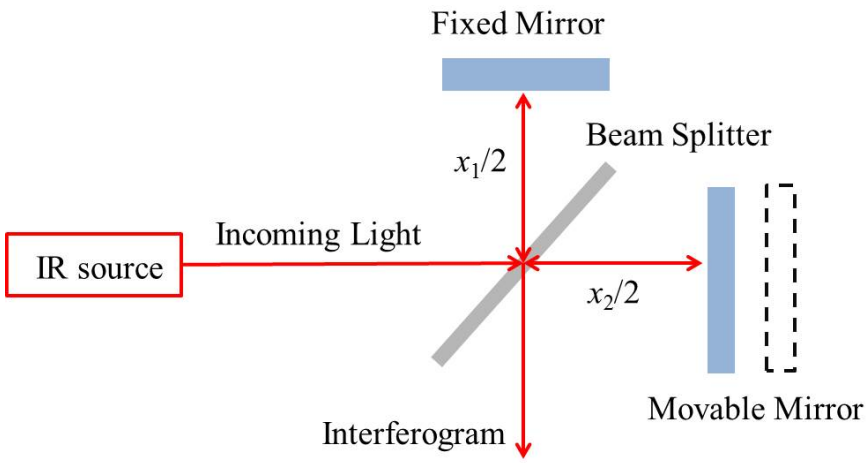

Figure 14: Schematic of an interferometer. The beam is split into two by the beamsplitter. Two beams travel a distance x_1 and x_2 when they are recombined, respectively.

accurate and reproducible making it a very reliable technique [47, 48, 49]. Fourier transform infrared spectroscopy is a powerful technique for the investigation of the low-lying energy excitations in materials. When combined with a magnetic field, it can be employed to study the cyclotron resonance and Landau level transitions [35, 50].

2.1.2 Simplified Math Description

Let the infrared light travel in the x direction. The amplitude of the wave can be written as

$$E(x,k) = E_0(k)e^{i(\omega t - 2\pi kx)}, \tag{38}$$

where k is the wavenumber and $E_0(k)$ is the maximum amplitude of the beam at $x = 0$. The amplitude of the beam is divided at the beam splitter and two beams are produced. Let x_1 and x_2 be the distance traveled by the beams when they recombine. As we can see from Figure 14, each beam undergoes one reflection and one transmission at the beam splitter. Let r and t be the reflection and transmission coefficients of the beam splitter, respectively. Then, the amplitude of the recombined

wave E_c is given by

$$E_c(x_1, x_2, k) = rtE_0(k)\left[e^{i(\omega t - 2\pi k x_1)} + e^{i(\omega t - 2\pi k x_2)}\right]. \tag{39}$$

By definition, the intensity of the recombined wave can be expressed as

$$\begin{aligned} I(p,k) &= E_c(x_1, x_2, k)E_c^*(x_1, x_2, k) \\ &= 2E_0^2(k)|rt|^2\left[1 + \cos(2\pi kp)\right] \\ &= I(k)\big(1 + \cos(2\pi kp)\big), \end{aligned} \tag{40}$$

where $I(k) = 2E_0^2(k)|rt|^2$ and $p = x_1 - x_2$ is the optical path difference. The total intensity for the whole spectral range is obtained by the following integration

$$I_c(p) - I(\infty) = \int_0^\infty I(k)\cos(2\pi kp)\, dk. \tag{41}$$

$I_c(p) - I(\infty)$ is the measured interferogram recorded at the detector. A Fourier transform of Eq. 41 converts the interferogram into a spectrum as

$$I(k) = \int_0^\infty \big(I_c(p) - I(\infty)\big)\cos(2\pi kp)\, dp. \tag{42}$$

The Fourier transform is performed by the computer converting the space domain to the wavenumber domain [51].

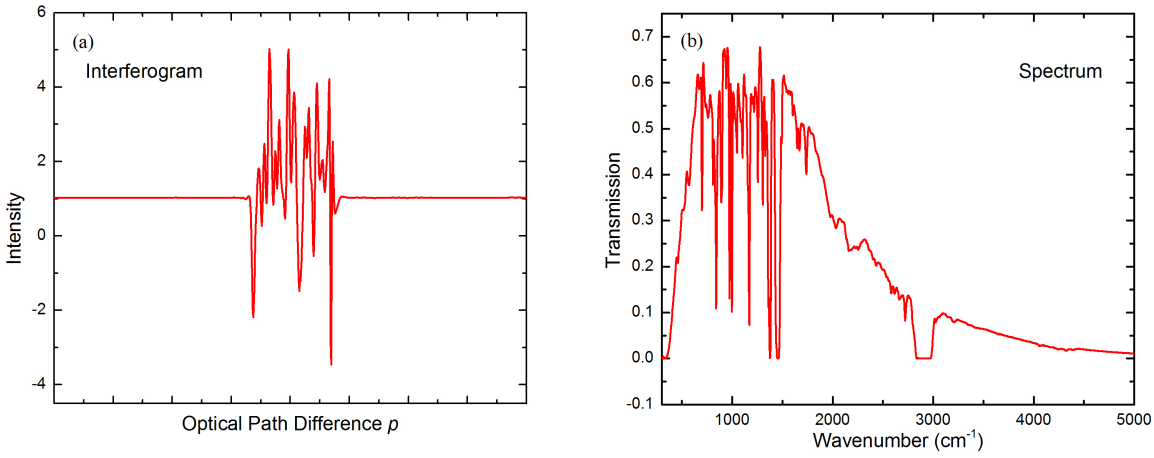

Figure 15: (a) Interferogram. (b) The spectrum obtained by Fourier transform from the interferogram.

2.1.3 Experimental Setup

The infrared magneto-spectroscopy measurement was performed at National High Magnetic Field Laboratory (Tallahassee, FL). Figure 16 (a) shows our typical experimental setup with a superconducting magnet. A commercial Bruker 113v is used

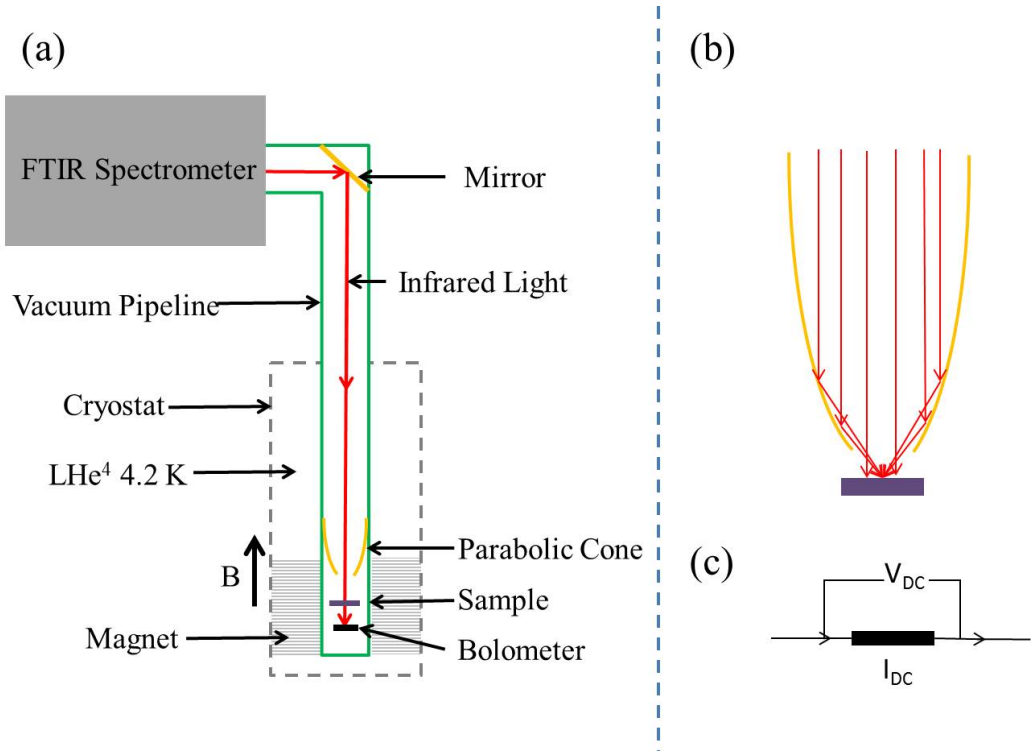

Figure 16: (a) Layout of the experimental setup. (b) Parabolic cone: the surface is coated with a thin layer of gold for better reflection. (c) Constant DC voltage is applied to the silicon bolometer while the current is measured.

as the FTIR spectrometer. The infrared light is delivered to the sample via a vacuum pipeline. The pipeline is pumped down to 1 mTorr to reduce the noise in the spectrum introduced by the absorption of air. Clean power-supply, clean ground, and vibration suppression are also necessary to decrease the noise level. A homemade parabolic cone coated with gold is placed right above the sample (Figure 16 (b)). This parabolic cone can focus the incoming parallel infrared light to one point. Because the sample is smaller than the diameter of the infrared beam, placing the sample at the focus point of the parabolic cone will allow most of the light to pass through

the sample so that we can get as strong signal as possible. The transmitted light is detected by a silicon bolometer after passing through the sample (Figure 16 (c)). The sample and bolometer are placed at the center of the magnet. The cryostat is filled with liquid He^4 and the temperature is kept at 4.2 K. The magnetic field is applied perpendicular to the surface of the sample and can go up to 35 T (resistive magnet).

The detector used in our FTIR measurement is a silicon bolometer. The resistance varies dramatically with the temperature. The bolometer at room temperature is very conductive while at ~ 4.2 K its resistance is more than 10 MΩ. The infrared radiation is popularly known as "heating source" because of its strong heating effect. Therefore, the temperature of the bolometer changes with the intensity of the infrared light leading to the resistance variation. By monitoring the resistance, we get information about the intensity of the infrared light. We apply a constant DC voltage across the bolometer and measure the current (Figure 16 (c)) which corresponds to the intensity of the infrared light passing the sample. Finally, the measured interferogram is converted to a spectrum via Fourier transform.

2.2 Graphene Nanoribbon Array Fabrication

2.2.1 Electron-beam Lithography

Electron-beam Lithography (EBL) can draw custom shapes and has very high resolution. The JEOL JBX-9300FS EBL system is used for the patterning, which has a large writing field (500 μm $\times$ 500 μm) with sub-10nm resolution. As shown in Figure 17 (a), we can write even larger patterns with the assistant of GenIsys *Layout BEAMER*, which is a powerful application. The EBL process contains several steps, including coating resist, baking, exposure, and development. Each step is essential for the final result. As shown in Figure 18, Hydrogen Silsesquioxane (HSQ, Dow Corning) of 2% concentration is spin-coated on the multilayer epitaxial graphene grown on the C-face of SiC. The acceleration rate is 2000 r/s and the final speed is

4000 rpm. We run at this speed for 60 seconds. The thickness of HSQ resist is about 353 Å after baked at 180 °C for 5 minutes on the hotplate. Then the sample is loaded into the EBL system immediately in order to produce a good result. The beam current of JEOL JBX-9300FS is constant with the value of 2 nA. The best dosage is 900 μC/cm^2 for the ribbon patterning on a SiC substrate. After exposure, the sample is developed in MF-319 developer (Microposit) for 70 seconds. HSQ is a negative resist which means the resist exposed to the electron-beam will remain and that not exposed to the electron-beam will be washed away by the developer. In addition, HSQ exposed to the electron-beam can not be etched by oxygen plasma at all. Therefore, it is a perfect mask for our work. At the end, the sample is rinsed in deionized (DI) water for 30 seconds and then blown dry very gently using nitrogen to remove the residue.

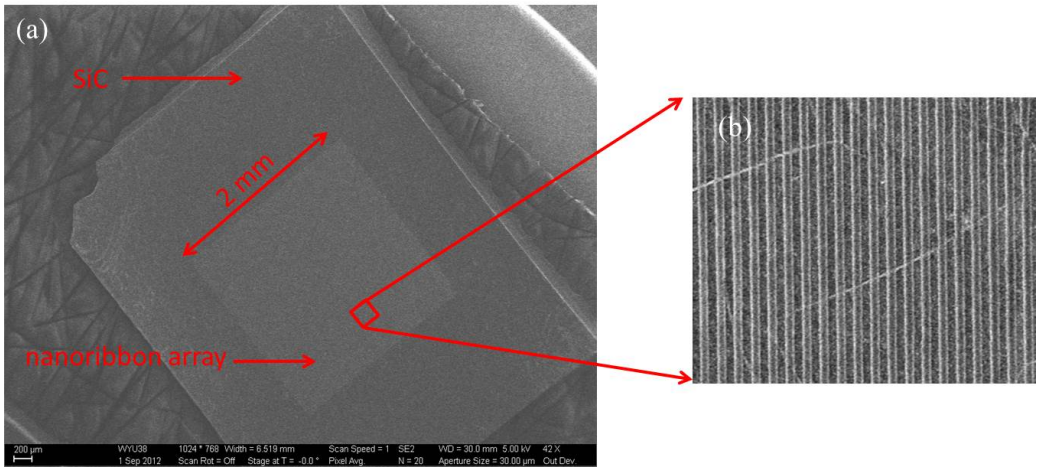

Figure 17: SEM image of epitaxial graphene ribbon array. (a) The size of the array is 2 mm × 2 mm. (b) Zoomed-in view of (a). The width of ribbon is 100 nm with 100 nm spacing.

2.2.2 Oxygen Plasma Etching

The pattern of HSQ on top of the graphene serves as a mask when the sample is etched by oxygen plasma. The oxygen plasma etching is performed using the Plasma-Therm RIE (reactive-ion etching) system with recipe ZSO_SIC1. Running the recipe for

30 seconds is sufficient to etch 10-layer graphene which is confirmed by our Raman measurement. Actually, the etching time is doubled in our process to ensure the graphene exposed to plasma is removed completely. The HSQ is removed by being rinsed in Buffered oxide etch 6:1 (BOE, J.T.Baker) for 30 seconds then rinsed in DI water for 60 seconds. Now, we get the graphene nanoribbon array on the SiC substrate.

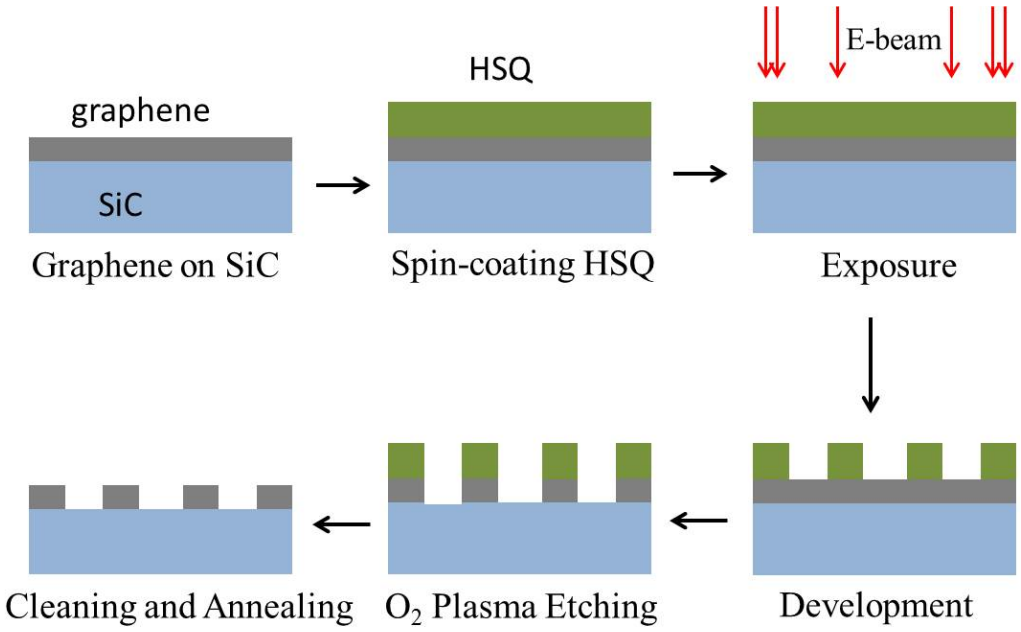

Figure 18: Graphene nanoribbon array fabrication process.

2.2.3 High Vacuum Annealing

Si-H bonds of HSQ can be broken by the electron-beam generating the hydrogen atoms [52]. The generated hydrogen atoms can form sp^3 C-H bonds with the graphene. These bonds, to some extent, lower the quality of our samples in the infrared transmission measurement leading to a weaker strength of the cyclotron resonance absorption. However, it has been proven that this process is reversible by thermal annealing at high temperature [53]. Our sample is annealed at 600 °C for 2 hours in high vacuum ($< 5 \times 10^{-5}$ mTorr) achieved by a turbo pump (Pfeiffer TC 110). The temperature is

increased to 300 °C with a ramping rate of 10 °C/minute and then increased to 600 °C at 5 °C/minute. 2 hours later, the furnace is shut down and the temperature drops to the room temperature slowly. The turbo pump is running during the whole process.

2.3 Sample Characterization

Scanning Electron Microscopy (SEM) is a powerful technique for imaging. The Zeiss Ultra60 FE-SEM is used to examine the quality of the graphene nanoribbon array. Because the SiC substrate we use is insulating, low voltage mode is selected with a typical voltage of 2 kV. The working distance is 5 mm. Figure 19 shows the SEM images of the samples. Atomic force microscopy (AFM, Park System XE-100) is also

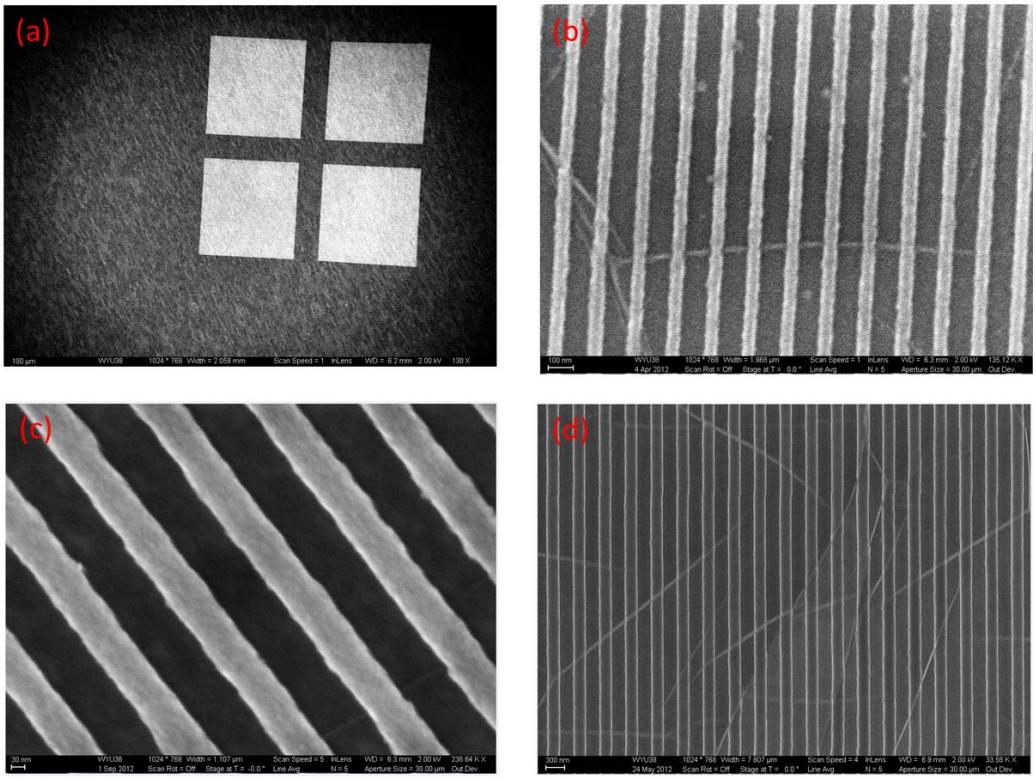

Figure 19: SEM image of epitaxial graphene nanoribbon arrays. (a) Four arrays on the substrate. Each array is 400 μm by 40 μm and the spacing between arrays is 100 μm. (b) 50 nm wide ribbons with 100 nm spacing. (c) 100 nm wide ribbons with 100 nm spacing. (d) 200 nm wide ribbons with 200 nm spacing.

employed to image the samples as shown in Figure 20. Non-contact mode is used to

protect the sample. Compared to SEM, AFM is more accurate with a resolution in the sub-nanometer range. In addition, it can measure the thickness of the sample.

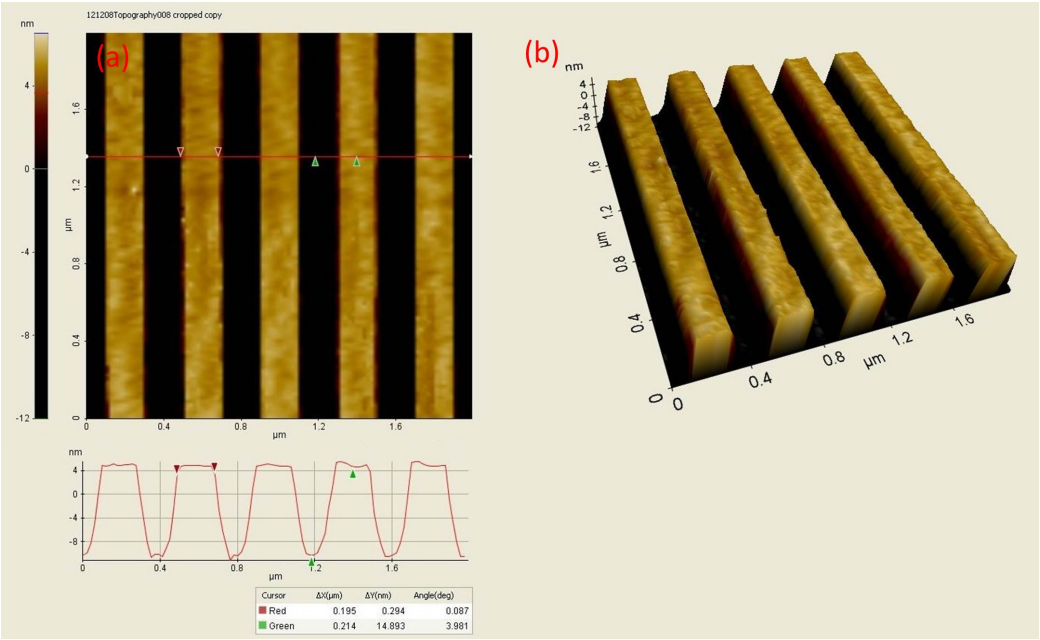

Figure 20: AFM image of epitaxial graphene nanoribbon arrays. (a) The width of ribbon is 200 nm with 200 nm spacing. The bottom panel shows the line profile. The pair of red arrows measures the width and the pair of green arrows gives the thickness of the ribbon. The thickness of multilayer epitaxial graphene is $\sim 148.9\,\text{Å}$ corresponding to ~ 44 graphene layers. (b) 3D view of the ribbons.

CHAPTER III

TUNING ELECTRON-PHONON COUPLING IN GRAPHITE VIA MAGNETIC FIELD

3.1 Introduction to Magnetophonon Resonance in Graphene and Graphite

In solids, electron interact with the motion of the lattice and sometime can be scattered into a different state. The electron-phonon coupling (EPC) is an important issue in solid state physics because it plays a key role in many phenomena [54]. Ballistic transport, superconductivity, excited state dynamics, Raman spectra and phonon dispersions all fundamentally depend on it [55]. Optical spectroscopy is one of the techniques used to investigate EPC, including Raman spectroscopy, infrared spectroscopy, and angle-resolved photoelectron spectroscopy (ARPES) [56].

An external magnetic field applied perpendicular to graphene gives rise to discrete Landau levels. The optical phonon energy may coincide with the energy of one of the inter-Landau-level transitions, leading to the magnetophonon resonance. EPC in graphene and graphite has been extensively studied via Raman spectroscopy [6, 57, 58]. Figure 21 shows the magnetic field evolution of the Raman scattering response of the E_{2g} phonon in multilayer epitaxial graphene in fields up to 33 T. A pronounced avoided crossing behavior of the phonon energy is observed each time the inter-Landau-level transition is tuned in resonance with the phonon energy. The experimental results are interpreted well by the theoretical models of electron-phonon coupling in graphene. In graphene, optical phonons are represented by the relative displacement of two sub-lattice atoms **A** and **B**. The Hamiltonian for phonons and

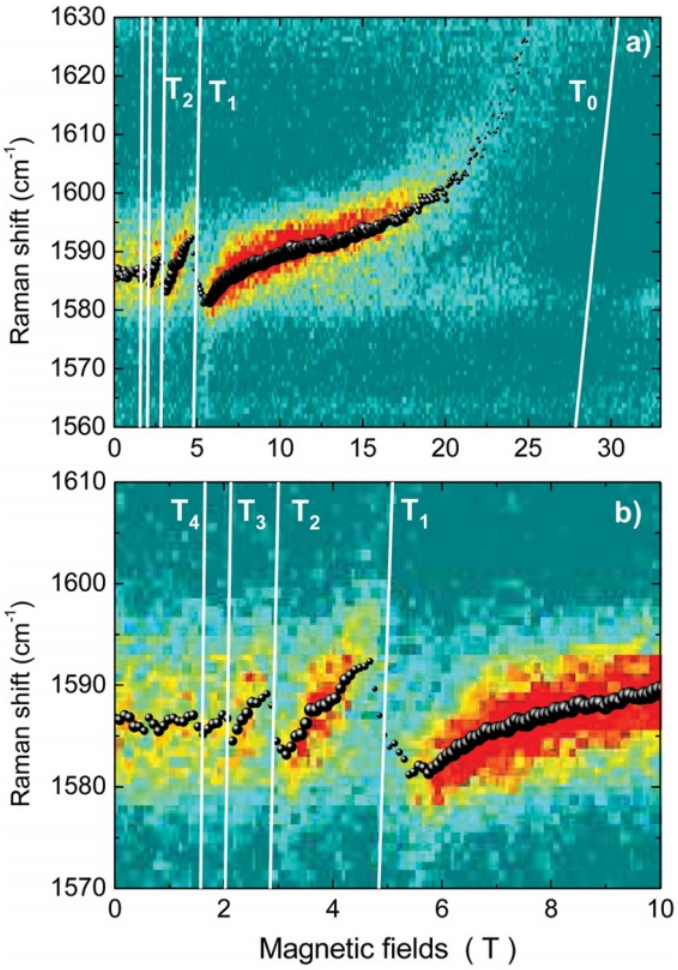

Figure 21: (a) Color map of the magneto-oscillatory component of Raman scattering spectra of E_{2g} band phonons as a function of magnetic field measured at $T = 4.2$ K. The extracted peak position is shown with full dots. The size is proportional to the line amplitude. Solid lines T_k represent the energies of the inter-Landau-level transitions: $L_{-k,(-k-1)} \to L_{k+1,(k)}$, which couple to E_{2g} phonon. (b) Zoomed-in view of the 0 to 10 T range of the magnetic fields. Reprinted from Ref. [6].

EPC can be written as [59, 60, 61]

$$\begin{aligned} \boldsymbol{u}(\boldsymbol{r}) &= \sum_{\boldsymbol{q},\mu} \sqrt{\frac{\hbar}{2Nm\omega}} (b_{\boldsymbol{q},\mu} + b^{\dagger}_{-\boldsymbol{q},\mu}) \boldsymbol{e}_{\boldsymbol{q},\mu} e^{-i\boldsymbol{q}\cdot\boldsymbol{r}}, \\ H_{ph} &= \sum_{\boldsymbol{q},\mu} \omega b^{\dagger}_{\boldsymbol{q},\mu} b_{\boldsymbol{q},\mu} + g\sqrt{2m\omega}(\sigma_x u_y - \sigma_y u_x), \end{aligned} \tag{43}$$

where N is the number of unit cells, m is the mass of a carbon atom, ω is the phonon energy at the Γ point, $\boldsymbol{q} = (q_x, q_y)$ is the wave vector, and μ denotes the mode (t for transverse and l for longitudinal). $b^{\dagger}_{\boldsymbol{q},\mu}$ and $b_{\boldsymbol{q},\mu}$ are the creation and destruction

operators of a phonon with polarization $\mathbf{e}_{\mathbf{q},\mu}$, respectively. The constant g characterizes the electron-phonon coupling [62]. $\sigma = (\sigma_x, \sigma_y)$ are the Pauli matrices. The dressed phonon propagator corresponding to the Hamiltonian in Eq. 43 is obtained by solving Dyson's equation. The pole of this propagator gives the coupled mode frequencies,

$$\omega_A^2 - \omega^2 = 4\omega \left[\sum_{n=n_F+1}^{N} \frac{\Omega_n g_A^2(n)}{\omega_A^2 - \Omega_n^2} + \frac{\Delta_{n_F} g_A^2(n_F)}{\omega_A^2 - \Delta_{n_F}^2} \right], \tag{44}$$

where n_F stands for the number of the highest fully occupied Landau level, g_A is the effecting coupling constant, $\Delta_n = v_F\sqrt{2e\hbar B}(\sqrt{n+1} - \sqrt{n})$, and $\Omega_n = v_F\sqrt{2e\hbar B}(\sqrt{n+1} + \sqrt{n})$ represents the energy of inter-Landau-level transitions (cyclotron resonance).

The strongest effect of the electron-phonon coupling occurs when ω coincides with Ω_n. In such a case, Eq. 44 can be simplified to

$$\begin{aligned} \omega_A^{\pm}(n) &= \frac{1}{2}(\Omega_n + \omega_0) \mp \sqrt{\frac{1}{4}(\Omega_n + \omega_0)^2 + g_A(n)^2}, \\ \omega_0 &\simeq \omega + \sum_{n=0}^{n_F} \frac{\Omega_n g_A^2(n)}{\omega^2 - \Omega_n^2}, \end{aligned} \tag{45}$$

where "$\pm$" represents the lower and higher mode. Figure 22 shows the peak positions and line width of magnetophonon resonance extracted from Figure 21. The solid red lines represent the best fit using Eq. 44. This model can be used to explain the magnetophonon resonance in graphene [6, 57] and also the phenomena occurring in graphite [58, 63].

The electron-phonon coupling in graphene and graphite has been studied for many years. Understanding EPC in graphitic materials is of fundamental interest, while tuning EPC is technologically important for the development of carbon-based nanoelectronics. The EPC can be tuned by electric and magnetic fields, through Fermi-energy shifting and Landau quantization. In this chapter, we explore the magnetic-field tunable EPC in graphite via infrared spectroscopy.

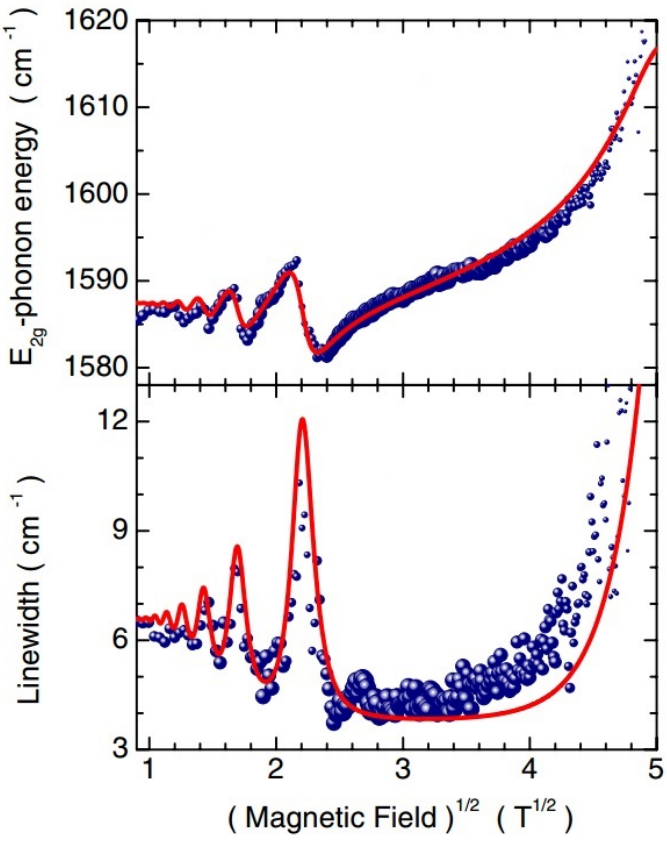

Figure 22: Magnetic field evolution of the peak position (upper part) and the linewidth of the magneto-oscillatory component of the measured E_{2g} Raman band. Solid red lines show the best fit using Eq. 44. Reprinted from Ref. [6].

3.2 Experiments and Discussion

3.2.1 Experimental Method

To study the transmission spectra of graphite, we use ultrathin graphite flakes in order for there to be sufficient light transmission. Following the method to create exfoliated graphene [33, 21], we prepare the ultrathin graphite flakes by repeatedly pulling scotch tape off the highly oriented pyrolytic graphite. This technique is similar to that used in the previous works [64, 42]. The tape used in our experiment (Figure 23 (a)) is selected to allow for sufficient infrared light transmission in the frequency range of interest. Figure 23 (b) shows the Raman spectrum and an optical image of the graphite flakes.

The experimental setup is shown in Figure 16. A broadband source (Globar lamp) is used to generate infrared radiation and a KBr beamsplitter is employed in the interferometer. The ultrathin graphite flakes together with the tape are mounted on a sample holder located at the center of the resistive magnet. The magnetic field can go up to 35 T. The transmission spectra are recorded with a computer.

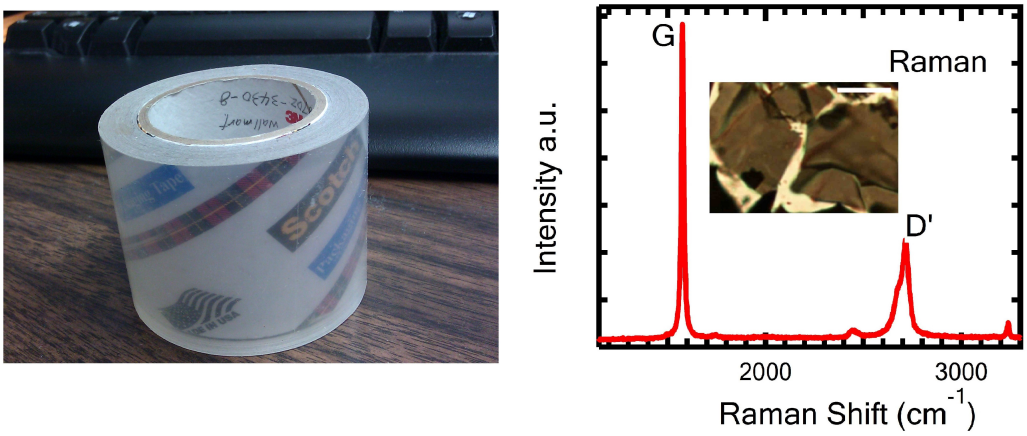

Figure 23: (a) The Scotch tape used for our ultrathin graphite flakes preparation. The part number is 34-8702-3430-8. (b) Raman spectrum of ultrathin graphite flakes. Typical G peak and D' peak are evidenced. Inset: Optical image of ultrathin graphite flakes.

3.2.2 Results and Analysis

Graphite has proven to be an interesting system to study EPC [62, 65]. It has a peculiar (optical) phonon dispersion relation [66], with the Raman-active E_{2g} phonon and infrared-active E_{1u} phonon degenerated at the Γ point and the A_1' phonon located at the K point. These optical phonon modes strongly interact with charge carriers, which set the ultimate limit to high-field ballistic transport [67] and give rise to anomalies in Raman [55] and photoemission spectra [68].

Figure 24 shows the transmission spectrum of the tape used in our experiment. As we can see, this tape is quite transparent except a few absorption dips. More than 80% of the infrared light will pass the tape, especially for the light of the same frequencies as those of the K-point and Γ-point optical phonons in graphite. In

addition, the transmission spectra of the tape has little dependence on magnetic field which is good for our infrared magneto-spectroscopy measurement.

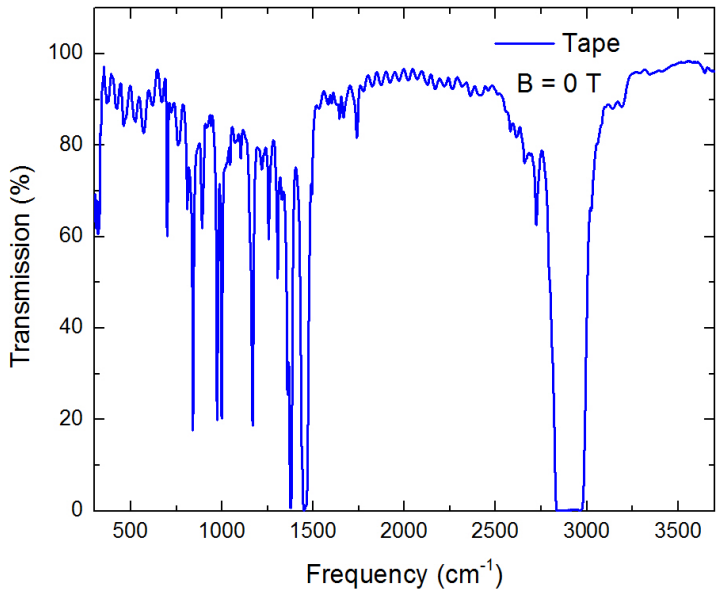

Figure 24: Infrared transmission spectrum of the Scotch tape used in the experiment at zero magnetic field.

Figure 25 shows the raw transmission spectra of the ultrathin graphite flakes on the tape substrate which are quite different from that of the tape because of the additional absorption of graphite flakes. One spectrum is measured at zero magnetic field while the other one is taken at $B = 20$ T. The difference between two spectra is due to the magnetic field effect. We divide the spectra measured at different magnetic fields $T(B)$ by the zero-field spectrum $T(0)$ and get the relative transmission spectra of graphite $T(B)/T(0)$ as shown in Figure 26.

As we can see, four distinct inter-Landau-level transitions (cyclotron resonance, CR) can be identified (using Nakao notation [69]): K point: $(LL-1) \rightarrow e1$, K point: $h1 \rightarrow e2$, H point: -1$\rightarrow$0, and H point: -2(-1)$\rightarrow$1(2). At the K point of the graphite Brillouin zone, as we discussed in the section 1.2.2, the Landau energies can be well approximated by the effective bilayer graphene model with the interlayer coupling γ_1 doubled. Using Eq. 37, we can calculate the energies of Landau levels $LL-1$, $h1$,

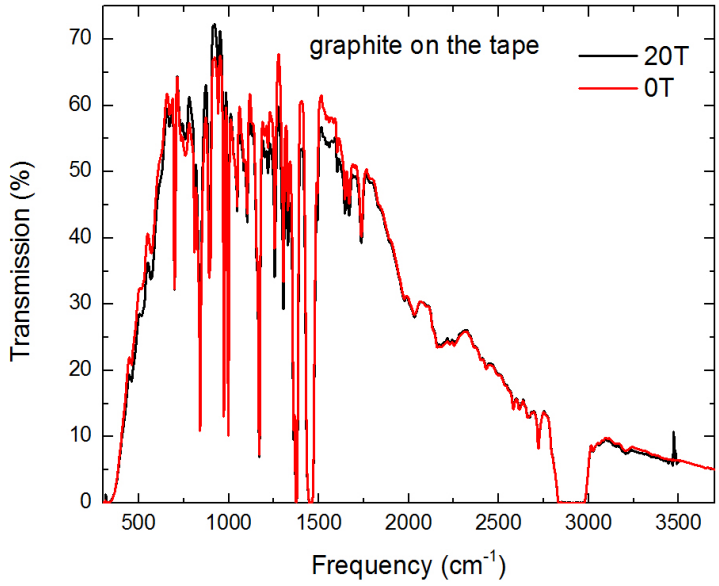

Figure 25: The raw spectra of ultrathin graphite flakes on the Scotch tape.

$e1$, and $e2$. Then, the transition energies $(LL-1) \rightarrow e1$ and $h1 \rightarrow e2$ are obtained as shown in Figure 26 (dashed red line and dashed orange line). The CR energies at the K point are linear with respect to magnetic field B. The parameters we use here are $\gamma_1 = 0.6\,\text{eV}$, $v_F = 0.91 \times 10^6$ m/s for transition $h1 \rightarrow e2$, and $v_F = 1.14 \times 10^6$ m/s for transition $LL-1 \rightarrow e1$.

The carriers at the H point behave like massless Dirac fermions in monolayer graphene [2, 64, 70]. The CR energy scales with $\sqrt{B}$ as indicated in Eq. 31. Therefore, the energy of the transition H: $n = -2(-1) \rightarrow 1(2)$ is given by

$$\Delta E = v_F \sqrt{2e\hbar B}(\sqrt{2} + \sqrt{1}), \tag{46}$$

where Fermi velocity $v_F = 1.02 \times 10^6$ m/s [71]. In Figure 26, the dashed green line represents the best fit. The dashed yellow line guides the transition $H : n = -1 \rightarrow 0$. Ideally, the CR energy is given by $\Delta E = v_F \sqrt{2e\hbar B}(\sqrt{1})$. Experimentally, we find that the energy dispersion fails to follow $\sqrt{B}$ dependence rigorously due to the electron-phonon coupling. We will focus on this CR in discussion below.

The cyclotron resonance $(H : n = -1 \rightarrow 0)$ can be tuned via magnetic field. When the CR energy is not comparable with the phonon energy at relatively low

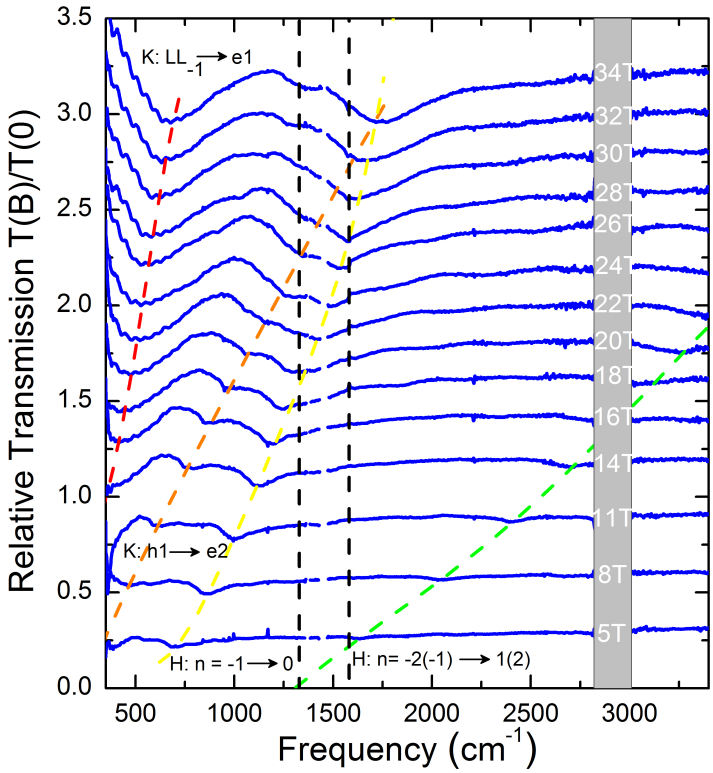

Figure 26: The relative transmission spectra of ultrathin graphite flakes on Scotch tape at different magnetic fields. The spectra are vertically shifted for clarity. The dashed red, orange, and green lines represent the best fits to the transitions, while the dashed yellow line guides the evolution of the transition $H : n = -1 \rightarrow 0$ as a function magnetic field. Two vertical dashed lines indicate the relevant phonon energies.

or quite high magnetic field, it can be predicted by Eq. 31 and the CR absorption lineshape can be described well using a single Lorentzian model as

$$T(\omega) = \frac{A}{\pi} \frac{\frac{1}{2}\Gamma}{(\omega - \omega_c)^2 + (\frac{1}{2}\Gamma)^2}, \tag{47}$$

where ω_c is the CR energy, Γ is the linewidth (full width at half maximum, FWHM), and A corresponds to the spectral weight. A representative fit to the spectrum at 34 T is shown in Figure 27. However, when the CR energy approaches the energy of $K - A_1'$ phonons with decreasing the magnetic field, they become to strongly interact with each other. As a result, the CR splits into two modes. This phenomenon is known as "anti-crossing". In such a case, we introduce a two-Lorentzian model to

analyze the splitting of the CR quantitatively.

$$T(\omega) = \frac{A_+}{\pi} \frac{\frac{1}{2}\Gamma_+}{(\omega - \omega_+)^2 + (\frac{1}{2}\Gamma_+)^2} + \frac{A_-}{\pi} \frac{\frac{1}{2}\Gamma_-}{(\omega - \omega_-)^2 + (\frac{1}{2}\Gamma_-)^2}, \tag{48}$$

where "+" ("-") corresponds to the higher (lower) mode. The relative transmission spectra $T(B)/T(0)$ at 10 T and 19 T as well as the corresponding fits are presented in Figure 27. As we can see, during the anti-crossing, the spectral weight of the lower branch gradually transfers to the upper branch with increasing magnetic field.

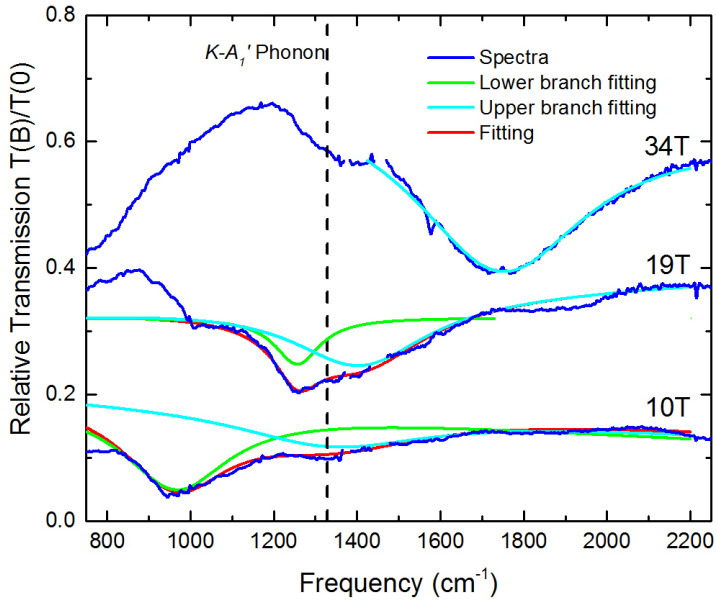

Figure 27: The relative transmission spectra $T(B)/T(0)$ of ultrathin graphite flakes on Scotch tape at selected magnetic fields. The spectra are vertically shifted for clarity. The green lines show the lower branch fitting, and the cyan lines represent the higher branch fitting. The red lines represent the fits using the two-Lorentzian model described by Eq. 48. At a high magnetic field (34 T), a single Lorentzian model is used to fit the spectrum.

Following this method, we fit all the relative transmission spectra and plot the fitting parameters as a function of B. Figure 28 (a) shows the extracted CR energies and Figure 28 (b) shows the linewidth at different magnetic fields. As we discussed in section 3.1, the EPC can be described by a standard two-coupled-mode model [57, 58, 61, 72]. Thus, we can rewrite Eq. 22 in a more conventional way as [58]

$$\omega_\pm - i\gamma_\pm = \frac{\tilde{\omega}_c + \tilde{E}_K}{2} \pm \sqrt{(\frac{\tilde{\omega}_c - \tilde{E}_K}{2})^2 + g^2}, \tag{49}$$

where "+"("-") stands for the higher (lower) branch. $\tilde{E}_K = E_K - i\gamma_K$, $\tilde{\omega}_c = \omega_c - i\gamma_c$, γ_K is the linewidth of the unperturbed phonon mode, γ_c is the linewidth of the CR, and g is the coupling parameter. Conventionally, a dimensionless parameter λ is often used to measure the strength of the electron-phonon coupling and the relation between λ and g is given by

$$g = \sqrt{\frac{\lambda}{4\pi}}\hbar\omega_B, \tag{50}$$

where $\hbar\omega_B = v_F\sqrt{2e\hbar B}$ is the magnetic energy and v_F is the Fermi velocity of carriers at the H point in graphite. In Figure 28 (a), the solid black lines represent the best fit to the data using Eq. 49. Here, $v_F = (1.04 \pm 0.01) \times 10^6$ m/s, $E_K = 1329 \pm 9\text{cm}^{-1}$, and $\lambda_K = (5.2 \pm 0.9) \times 10^{-2}$ are obtained from the fit. We neglect γ_K in Eq. 49, because it is much smaller than γ_c ($\gamma_K \ll \gamma_c$). In Figure 28 (b), we first fit the γ_c with an empirical formula $\gamma_c = 6.0 \times B$ without considering the electron-phonon coupling. This magnetic field dependence of linewidth is likely due to the linear-in-B scattering rate of the charge carriers in the $n = 0$ Landau level [73].

In Figure 26, there is another small spectral feature around 1581cm^{-1} when $B >$ 16T. This feature is due to the interaction between the CR and the $\Gamma - E_{1u}$ phonon leading to the magnetophonon resonance. The asymmetric lineshape reminds of the Fano resonance and it can be explained well by the Fano formula [74]. In our case, the asymmetric Fano resonance lineshape is due to the quantum interference between the continuum state of CR and the discrete state of $\Gamma - E_{1u}$ phonon. Our result is also consistent with that reported in the bilayer graphene [75]. We fit the Fano-like feature after removing the CR background, following the Fano formula in Reference [76],

$$T(E) = -\frac{A_0}{\gamma}\frac{q^2 + 2qz - 1}{q^2(1 + z^2)}, \tag{51}$$

where $z = \frac{E - E_{ph}}{\gamma}$. A_0 is a constant for a given magnetic field, E_{ph} is the phonon energy, γ is the linewidth, and q is the dimensionless Fano parameter characterizing the asymmetric lineshape. When $|q| \ll 1$, the spectra exhibit a peak. While $|q| \approx 1$, it

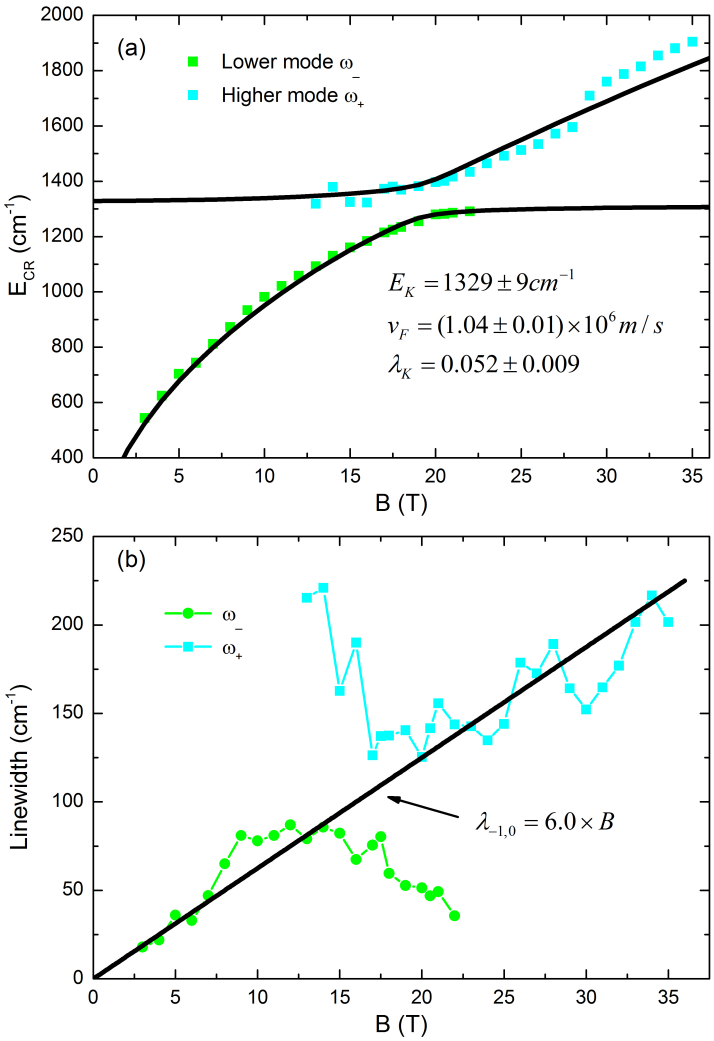

Figure 28: The extracted CR energies and linewidth from the results of the fits to the relative transmission spectra of graphite. (a) CR energy is plotted as a function of magnetic field. The solid lines show the best fits using Eq. 49. The fitting parameters are also presented. (b) Linewidth versus magnetic field. The solid line represents the best linear-in-B fit.

exhibits a dispersive lineshape. If $|q| \gg 1$, it shows a dip. Figure 29 shows the relative transmission spectra $T(B)/T(0)$ of graphite around 1580cm^{-1}. Three spectra (solid blue lines) at selective magnetic fields are showed with the corresponding fits (solid red lines). As we can see, the feature is developing from an anti-resonance peak (enhanced transmission) to a resonance dip(absorption) with increasing magnetic field. At low magnetic field, the system is in the electron-dominant regime giving rise to enhanced transmission. While at high magnetic field, the system is in the phonon-dominant

regime leading to the absorption.

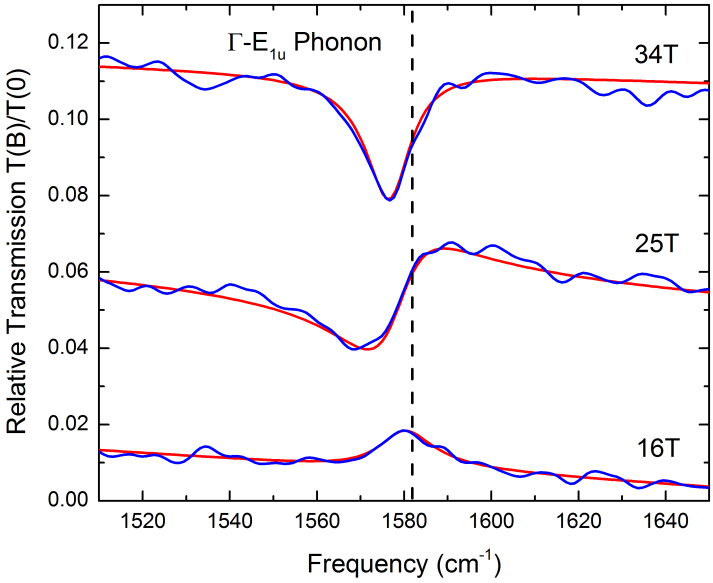

Figure 29: Relative transmission spectra $T(B)/T(0)$ of graphite around 1580cm^{-1} without CR background. The solid red lines represent the best fits using Eq. 51. The asymmetric lineshape develops from a peak to a dip with increasing magnetic field.

Figure 30 (a) shows the extracted phonon energy E_{ph} as a function of magnetic field and Figure 30 (b) shows the extracted linewidth. Still, we can perform a quantitative analysis in terms of electron-phonon coupling using Eq. 49 after replacing E_K (γ_K) with E_Γ (γ_Γ). It turns out that both E_{ph} and linewidth can be described well in this case. $E_\Gamma = 1581\text{cm}^{-1}$, $\gamma_\Gamma = 4.0\text{cm}{-}1$, and $\lambda_\Gamma = 0.0072$ result in the best fits as shown in Figure 30 (solid black lines). Here, $\lambda_\Gamma = 0.0072$ is an order of magnitude smaller than $\lambda_K = 0.052$. As λ characterizes the electron-phonon coupling, weak electron-phonon coupling (small λ) will give rise to continuous changing in the magnetophonon resonance energy while strong electron-phonon coupling will result in the "anti-crossing" phenomenon. The Fano parameter q and A_0 are shown in Figure 31. At low magnetic field, $|q| < 1$ corresponds to an anti-resonance peak in the spectra. At high magnetic field, $|q| > 1$ and the spectra exhibit a resonance dip. Basically, $|q|$ increases when the CR energy approaches, crosses, and passes the phonon energy with increasing magnetic field. The fitting parameter A_0 quickly increases at the

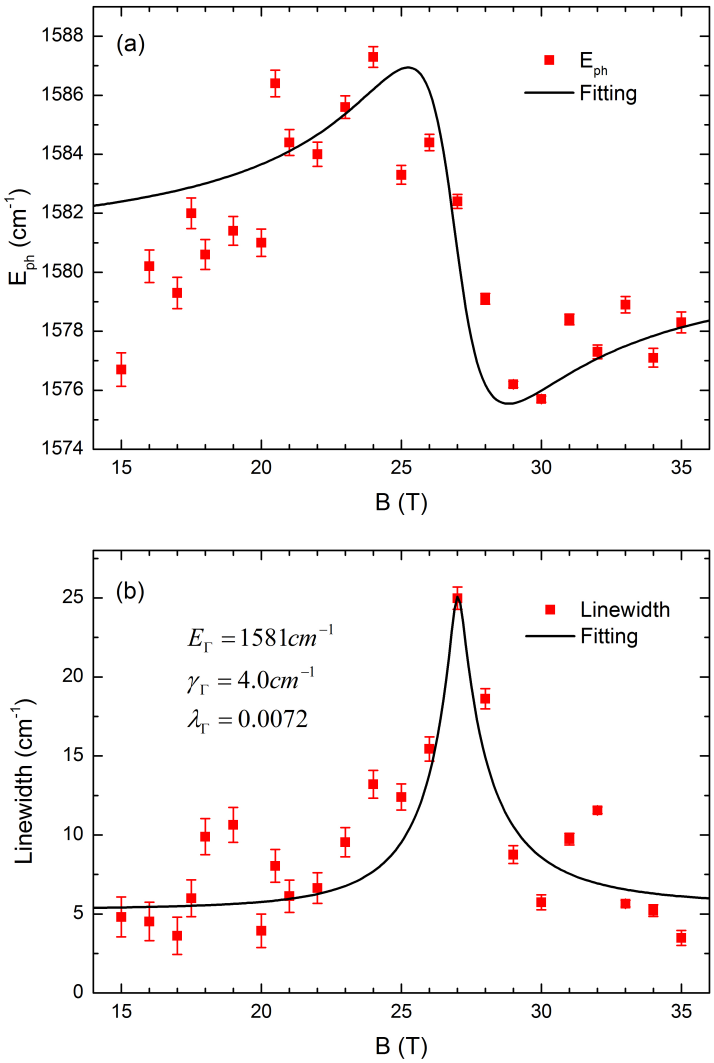

Figure 30: The extracted E_{ph} energy and linewidth from the Fano fits. (a) E_{ph} is plotted as a function of magnetic field. (b) Linewidth versus magnetic field with fitting (solid black line) using Eq. 49. The solid black lines represent the best fit using Eq. 49. The fitting parameters are also presented.

resonance of the phonon energy and then decreases with increasing magnetic field. This result is consistent with the charge-phonon theory [77].

3.3 Conclusion

We performed the infrared spectroscopy measurement of ultrathin graphite flakes in magnetic field up to 35 T. Four distinct inter-Landau-level transitions are observed. Two of them are associated to the carriers at the K point of graphite Brillouin zone

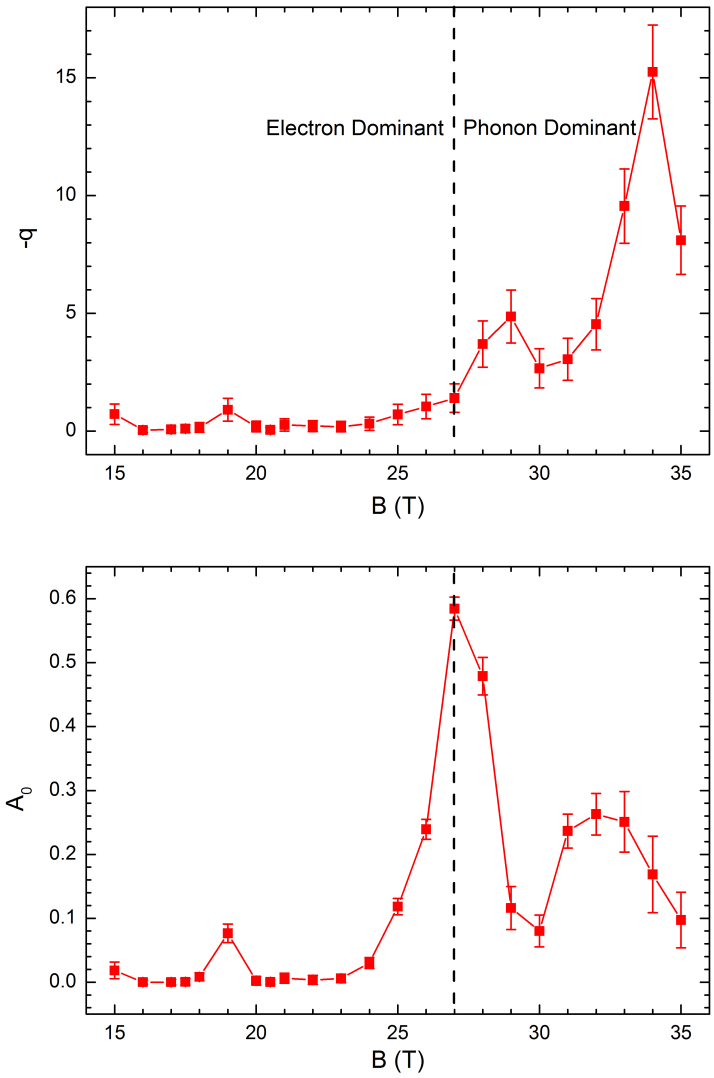

Figure 31: Fitting parameters q and A_0 as a function of magnetic field.

and they scale with magnetic field B similar to that of bilayer graphene. The other two transitions occur at the H point with $\sqrt{B}$ dependence. The carriers at the H point behave like massless Dirac fermions in monolayer graphene. The cyclotron resonance energy ω_c corresponding to the inter-Landau-level transition $H : -1 \rightarrow 0$ crosses two phonon modes $K - A_1'$ and $\Gamma - E_{1u}$ via tuning magnetic field. The interaction between the cyclotron resonance and the phonon $K - A_1'$ is relatively strong giving rise to the anti-crossing phenomenon and the feature in the spectra can be well described using a two-Lorentzian model. The electron-phonon coupling

around the phonon mode $\Gamma - E_{1u}$ is weak resulting in the magnetophonon resonance. The asymmetric Fano-like lineshape in the spectra can be well fit using the Fano formula. We demonstrate that both of the electron-phonon couplings can be tuned by varying the magnetic field. Although the two couplings behave quite differently, both of them can be successfully analyzed using a standard two-coupled-mode model.

CHAPTER IV

MAGNETOPLASMONS IN EPITAXIAL GRAPHENE NANORIBBONS

4.1 Introduction

4.1.1 Epitaxial Graphene

Epitaxial graphene is obtained by annealing silicon carbide (SiC) at high temperature. In this process, silicon sublimes from the surface and the carbon layer transforms to graphene. High-quality epitaxial graphene can be produced by a confinement controlled sublimation (CCS) method developed by Prof. Walter A. de Heer's group at Georgia Tech [78]. Such graphene exhibits all the transport properties of isolated graphene including Shubnikov−de Haas (SdH) oscillations with a Berry phase shift of π [79], weak antilocalization [80], the half integer quantum Hall effect [81], and highly efficient spin transport [82]. Figure 32 shows a direct measurement of quantized Landau levels in epitaxial graphene via scanning tunneling spectroscopy [7]. The characteristic $n = 0$ Landau level state is observed as well as the square root field dependence of Landau level energies.

Compared to exfoliated graphene, epitaxial graphene plays a pivotal role in the development of graphene-based large scale integrated electronics [78, 83, 84, 85, 86]. For example, Figure 33 shows an array of epitaxial graphene transistors on SiC substrate [8]. Epitaxial graphene can be grown on a wafer scale and patterned using the standard lithographic technique. It has many attractive properties for next-generation nanometer-scale electronics such as high mobility [79, 81], ballistic and coherent conduction [87], and high maximum current density.

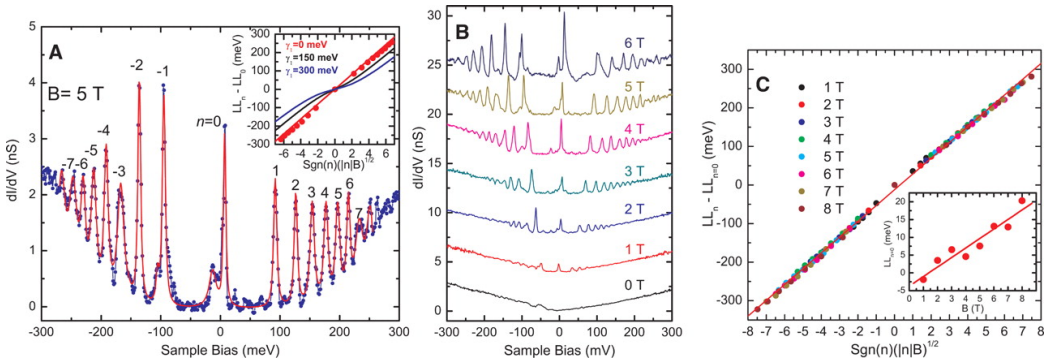

Figure 32: (A) Blue data points show the Landau levels in the tunneling differential conductance spectra versus sample bias in multilayer epitaxial graphene at $B = 5$ T. The red line shows the best fit. (Inset) Landau level peak position versus the square root of Landau level index and magnetic field. (B) Landau level spectra at various magnetic fields. (C) Landau level energies at different magnetic fields (1 T to 8 T) as a function of the square root of Landau level index and magnetic field. The linear fit (solid line) yields a Fermi velocity of $v_F = 1.128 \pm 0.004 \times 10^6$ m/s. Reprinted from Ref. [7].

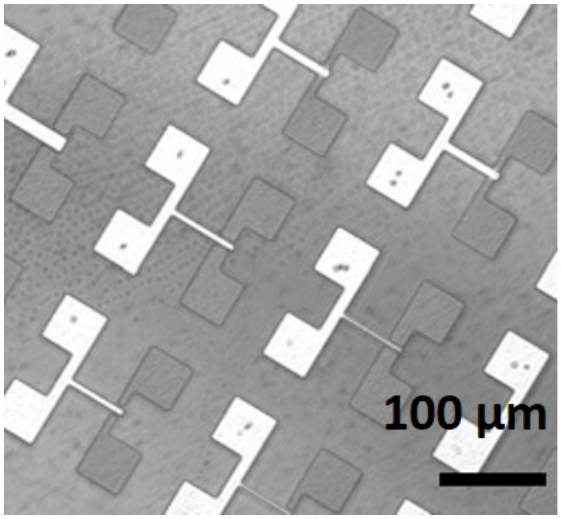

Figure 33: Optical image of epitaxial graphene transistors on SiC substrate. Reprinted from Ref. [8].

4.1.2 Infrared Magneto-spectroscopy of Epitaxial Graphene

Epitaxial graphene grown on SiC is suited for infrared magneto-spectroscopy studies due to the large graphene coverage on the wafer and the transparency of SiC in the infrared spectral range. Ever since its successful growth, many infrared measurements have been performed revealing unique properties of epitaxial graphene [2, 37, 38, 88,

89, 90].

4.1.2.1 Multilayer graphene on C-face

Multilayer graphene can be grown epitaxially on the carbon terminated face of single crystal silicon carbide [83]. The first 1-2 layers are electron doped due to the built-in electric field leading to charge transfer from the substrate to graphene, and the other layers are essentially undoped [91]. Multilayer epitaxial graphene also exhibits a unique crystal structure. The graphene layers are typically rotated by angles other than the 60° rotation of graphite. This unusual stacking makes the top graphene layers electronically decouple from each other which has been predicted theoretically [92, 93] and proven in experiments [2, 7, 9, 38]. The electronically isolated graphene sheets show a set of nearly independent linearly dispersing bands (Dirac cones) at the graphene K point in the angle-resolved photoemission spectrum (ARPES) (shown in Figure 34) [9]. Each Dirac cone corresponds to an individual graphene sheet.

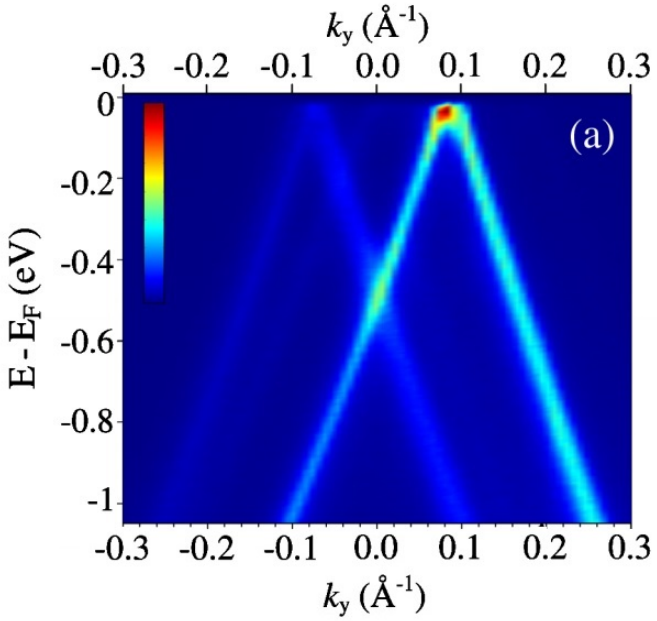

Figure 34: Band structure of an 11-layer epitaxial graphene on C-face measured by ARPES. Two linear Dirac cones are visible. Reprinted from Ref. [9].

Figure 35 shows the relative transmission spectra (solid black lines) of multilayer

epitaxial graphene grown on the C-face of SiC. The thickness of graphene is approximately 100 Å corresponding to about 30 graphene layers. A typical cyclotron resonance absorption lineshape is observed, which relates to the inter-Landau-level transition $LL_{-1(0)} \rightarrow LL_{0(1)}$. Note that the two transitions $LL_{-1} \rightarrow LL_0$ and $LL_0 \rightarrow LL_1$ are indistinguishable because the incident infrared light is unpolarized. The resonance lineshape can be described well (solid red lines in Figure 35) using a single Lorentzian model as

$$T(\omega) = \frac{2a}{\pi} \frac{\gamma}{4(\omega - \omega_c)^2 + \gamma^2}, \tag{52}$$

where a depends on the weight of the spectra, γ is the linewidth, and ω_c is the CR energy ($LL_{-1(0)} \rightarrow LL_{0(1)}$).

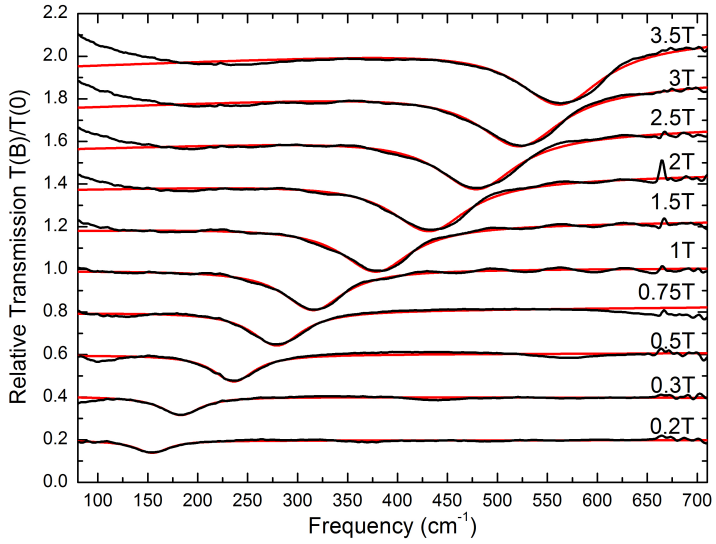

Figure 35: Relative transmission spectra of 30-layer epitaxial graphene grown on the C-face of SiC (solid black lines). Solid red lines represent the best fits using Eq. 52. Spectra are vertically shifted for clarity.

The extracted CR energy ω_c is plotted as a function of $\sqrt{B}$ in Figure 36. The Landau level energy of quasineutral graphene has $\sqrt{B}$ dependence, given by (refer to section 1.2.1)

$$E_n = \mathrm{sgn}(n) v_F \sqrt{2e\hbar B|n|}, \tag{53}$$

where v_F is the Fermi velocity and n is the Landau level index. Therefore, ω_c of the

inter-Landau-level transition $LL_{-1(0)} \rightarrow LL_{0(1)}$ reads

$$\omega_c = v_F\sqrt{2e\hbar B}(\sqrt{1} - \sqrt{0}). \tag{54}$$

The solid red line in Figure 36 shows the best linear fit to the CR energy using Eq. 54. The result of the fit gives a Fermi velocity of $v_F = (1.02 \pm 0.01) \times 10^6$ m/s, which agrees well with that reported in other works [2, 21, 33, 37].

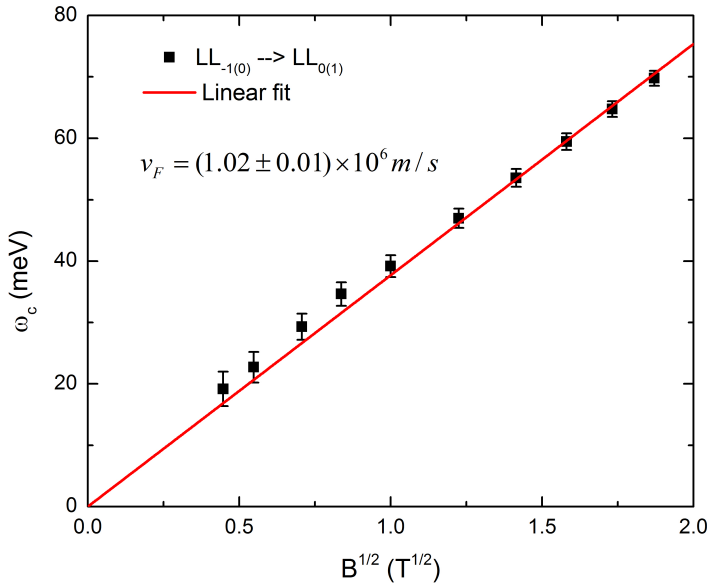

Figure 36: CR energy plotted as a function of $\sqrt{B}$. The solid red line represents the best linear fit using Eq. 54; $v_F = (1.02 \pm 0.01) \times 10^6$ m/s is obtained.

The linewidth γ is shown in Figure 37. Similar to the evolution of the CR energy with magnetic field, γ increases almost linearly with $\sqrt{B}$ as well. Note that this behavior at low energy range is different from that of holes at high energy regime in graphite sample. The electron-hole asymmetry will cause a linear B dependence of linewidth [39], which can not describe the data in our case. Shon and Ando [94] proposed that the $\sqrt{B}$ dependence of the linewidth is caused by the short- and long-range scatters. The short-range scatters will give rise to the same broadening of all Landau levels, while the long-range scatters will broaden Landau level $n = 0$ by a factor of $\sqrt{2}$ more than other Landau levels. Since only one transition is observed in our measurement, we can not justify which kind of scatters play a part in the

sample. In Ref [38], the authors observed no enhanced linewidth of $LL_{-1(0)} \rightarrow LL_{0(1)}$ transition compared to other transitions. They concluded that short-range scatters were dominant in that case.

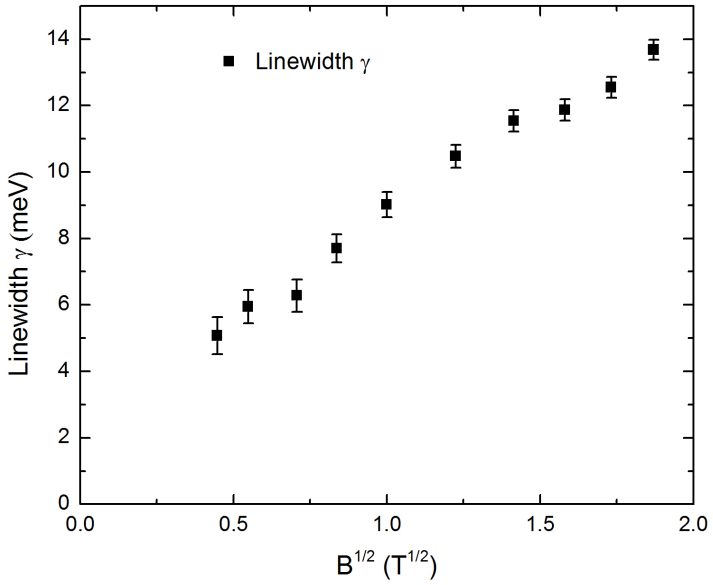

Figure 37: Linewidth of the CR plotted as a function of $\sqrt{B}$.

Next, we will discuss the spectral weight A of the absorption dip which is obtained by the following integration

$$A = \int_{\omega_c-\gamma}^{\omega_c+\gamma} \frac{2a}{\pi} \frac{\gamma}{4(\omega-\omega_c)^2+\gamma^2}\, \mathrm{d}\omega. \tag{55}$$

Figure 38 shows A as a function of $\sqrt{B}$. The relative transmission of two-dimensional conducting electrons for unpolarized light can be written as [95, 96]

$$\begin{aligned} T(\omega, B) &\approx 1 - \beta \frac{\mathrm{Re}[\sigma_{xx}(\omega, B)]}{\epsilon_0 c}, \\ \beta &= \frac{\kappa^2+3}{2(\kappa^2+1)}, \end{aligned} \tag{56}$$

where $\sigma_{xx}(\omega, B)$ is the optical conductivity, ϵ_0 is the vacuum permittivity, c is the speed of light in vacuum, and $\kappa = 2.6$ for SiC [38]. The optical conductivity is given by [97, 98, 99]

$$\sigma_{xx} = \frac{4G_B e^2}{\omega} \sum_{m,n} \frac{(f_m - f_n) M_{m,n}}{E_{m,n} - (\hbar\omega + i\gamma)}, \tag{57}$$

where $E_{m,n}$ are the transition energies $LL_m \rightarrow LL_n$, $G_B = (eB)/h$ is the Landau level degeneracy, $f_m\,(f_n)$ is the occupancies of the Landau levels, and $M_{m,n} = \frac{v_F^2}{p}\delta_{|m|,|n|\pm 1}$ are the selection rules with $p = 2$ for m or $n = 0$ and 4 otherwise. Therefore, the integrated transmission for the transition between the completely full LL_0 and the empty LL_1 can be written as

$$I(B) = \frac{\beta}{\epsilon_0 c}\int \mathrm{Re}(\sigma_{xx}(\omega))\,d\omega \approx \frac{e^3 v_F^2 B}{\epsilon_0 c E_1} = \beta\frac{e^2}{2\epsilon_0 \hbar c}E_1 \propto \sqrt{B}, \tag{58}$$

where $E_1 = v_F\sqrt{2e\hbar B}$ is the magnetic energy. Eq. 58 gives a rough estimate of the intensity of the transition $LL_0 \rightarrow LL_1$. In Figure 38, the solid red line represents the linear fit using Eq. 58. A Fermi velocity of $v_F = 1.93 \times 10^6$ m/s is obtained which is slightly higher but still reasonable.

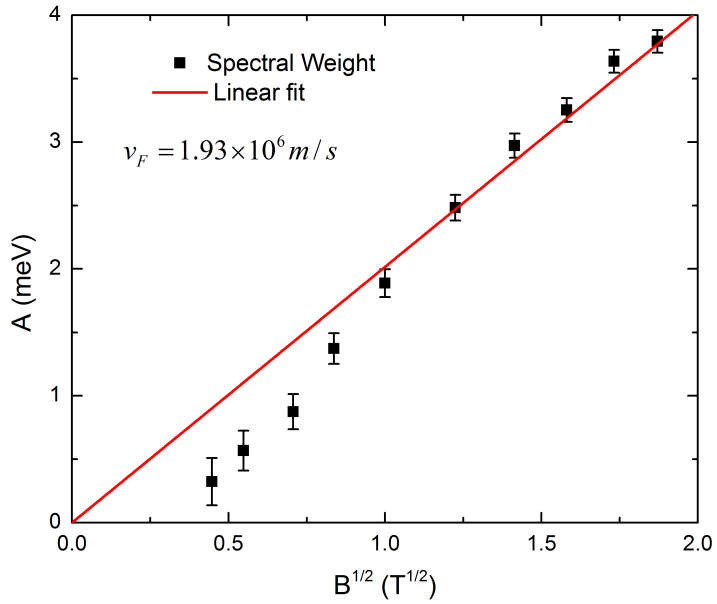

Figure 38: Spectral weight A plotted as a function of $\sqrt{B}$. The solid red line represents the best linear fit to all the data points using Eq. 58. $v_F = 1.93 \times 10^6$ m/s is obtained.

Besides this, other basic information about the graphene can be obtained from the inter-Landau-level transitions. The observed transition $LL_0 \rightarrow LL_1$ can help estimate the Fermi level of multilayer epitaxial graphene. The higher bound of the Fermi level

is equal to $n = 1$ Landau level energy. According to Eq. 53,

$$E_F \leq E_1 = v_F\sqrt{2e\hbar B_{lowest}}, \tag{59}$$

where B_{lowest} is the lowest magnetic field at which the transition $LL_0 \rightarrow LL_1$ can be observed. In our case, $B_{lowest} = 0.2$ T, which gives an estimated Fermi level of $E_F \leq 17$ meV with $v_F = 1.02 \times 10^6$ m/s. The Fermi level is slightly above the Dirac point indicating that multilayer epitaxial graphene is quasineutral. The carrier density n_s can be obtained by the following equation. In graphene [13],

$$\begin{aligned} E_F &= \hbar v_F k_F, \\ k_F^2 &= 2\pi n_s. \end{aligned} \tag{60}$$

Taking 2-fold degeneracy into account, n_s is given by

$$n_s = 2\frac{E_F^2}{2\pi\hbar^2 v_F^2} = \frac{E_F^2}{\pi\hbar^2 v_F^2}. \tag{61}$$

In our case, $E_F = 17$ meV yields $n_s = 2.1 \times 10^{10}\,\mathrm{cm}^{-2}$.

The carrier scattering time τ can be estimated from the linewidth of the CR. According to Ref. [3, 35],

$$\tau = \frac{2\hbar}{\gamma}, \tag{62}$$

where γ is the linewidth. In our work, the scattering time $\tau \sim 264$ fs is obtained at low magnetic field ($\gamma \approx 5.1$ meV) and decreases with increasing magnetic field. At $B = 3.5$T, $\gamma \approx 13.7$ meV and the scattering time $\tau \sim 96$ fs. $\tau \sim 100$ fs is reported for suspended graphene with carrier densities $\sim 10^{10}\mathrm{cm}^{-2}$ [100, 101]. $\tau \sim 200$ fs is reported for exfoliated graphene on Si/SiO_2 substrate at densities around $10^{12}\,\mathrm{cm}^{-2}$ and τ decreases with decreasing carrier density [102].

The semiclassical condition,

$$\omega_c\tau > 1, \tag{63}$$

will give an estimation of the lower bound for τ. At $B_{lowest} = 0.2$ T, $\omega_c = 17$ meV. Then

$$\tau > \frac{1}{\omega_c} \simeq 38\,\mathrm{fs}, \tag{64}$$

which is in agreement with the previous result based on the linewidth. The condition $\omega_c\tau > 1$ can be rewritten as $\mu B > 1$, where μ is the mobility. Then we can get an estimation of the lower bound for mobility $\mu > 1/B_{lowest} = 5 \times 10^4\,\mathrm{cm}^2/(\mathrm{V}\cdot\mathrm{s})$.

In Boltzmann transport theory, the conductivity is given as [103, 104]

$$\sigma(E_F) = \frac{e^2}{2} D(E_F) v_F^2 \tau, \tag{65}$$

where E_F is the Fermi level and $D(E_F) = g_s g_v \frac{|E_F|}{2\pi\hbar^2 v_F^2}$ is the density of states with $g_s = g_v = 2$ for the spin and valley degeneracy, respectively. Therefore,

$$\sigma(E_F) = \frac{2e^2}{h} |E_F| \frac{\tau}{\hbar}. \tag{66}$$

Here, $\sigma \approx 13e^2/h$ with $E_F = 17$ meV and $\tau = 264$ fs.

4.1.2.2 Epitaxial graphene on Si-face

It is known that graphene grown on the Si-face and on the C-face are different. Graphene on Si-face usually has few layers or even only one layer [105]. Due to the charge transfer from SiC, graphene on Si-face is usually highly doped [106]. The system is in the quasiclassical regime. The relative transmission spectra of graphene on a Si-face show a very much different lineshape. Instead of a Lorentzian-like resonance dip, the spectrum has a wide absorption minimum at relatively low energies as shown in Figure 39. In the classical theory for cyclotron resonance, the optical conductivity is written as [37]

$$\sigma_{\pm} = \sigma_0 \frac{i\gamma}{\omega \pm \omega_c + i\gamma}, \tag{67}$$

where "+" ("-") stands for the CR inactive (active) polarization mode of the infrared light. In the zero magnetic field, $\omega_c = 0$. Then, Eq. 67 describes the Drude model. σ_0 is the zero-field DC conductivity and γ is an introduced parameter accounting for the damping. In a simple approximation, the sample can be considered as though the graphene layer were infinitely thin and located between the vacuum and the SiC

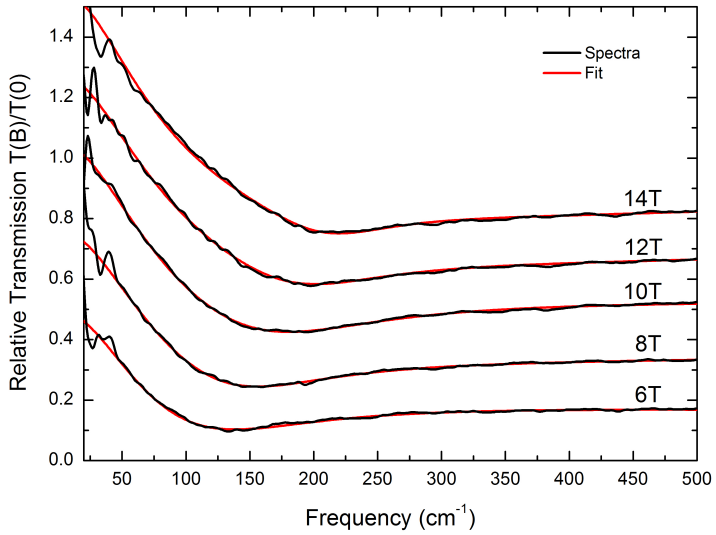

Figure 39: Relative transmission spectra of epitaxial graphene on Si-face of SiC. The spectra are vertically shifted for clarity. The red solid lines represent the best fits.

substrate with refractive index $n \simeq 2.6$. The transmission of unpolarized infrared light through the sample can be written as [107]

$$\begin{aligned} T_{\pm} &= \frac{16n^2}{|\alpha_{\pm}(\omega,B)|^2 - |\beta_{\pm}(\omega,B)|^2}, \\ \alpha_{\pm}(\omega,B) &= (n+1)\left[n+1+\frac{\sigma_{\pm}(\omega,B)}{\epsilon_0 c}\right], \\ \beta_{\pm}(\omega,B) &= (n-1)\left[n-1-\frac{\sigma_{\pm}(\omega,B)}{\epsilon_0 c}\right], \end{aligned} \tag{68}$$

where ϵ_0 is the vacuum permittivity and c is the speed of light. Note that Eq. 68 has already been simplified by averaging out the thickness of the slab. Then the relative transmission is given by

$$\frac{T(B)}{T(0)} = \frac{1}{2}\frac{T_+(B)+T_-(B)}{T(0)}. \tag{69}$$

The solid red lines in Figure 39 show the best fits which describe the spectra quite well. Zero-field $\sigma_0 = 2.5 \times 10^{-3}\Omega^{-1}$ and $\gamma_0 = 12$ meV are found to lead to the best fit. The other parameters σ_B, γ_B, and ω_c are obtained at a given magnetic field.

Figure 40 shows the CR energy as a function of magnetic field. The CR energy of epitaxial graphene on Si-face has linear-in-B dependence instead of $\sqrt{B}$ dependence.

In classical physics, the CR can be expressed by

$$\omega_c = \frac{eB}{m^*}, \tag{70}$$

where m^* is the effective mass of carriers. A linear fit to the CR energy (solid red line in Figure 40) yields $m^* = 0.065\, m_0$, where m_0 is the the mass of an electron. According to the Einstein relation $E_F = mv_F^2$, the Fermi level of graphene on Si-face is $E_F = 387$ meV with Fermi velocity $v_F = 1.02 \times 10^6$ m/s [37, 106, 108]. The Fermi level is far away from the Dirac point. The carrier density of $n_s \simeq 1.0 \times 10^{13}\,\mathrm{cm}^{-2}$ indicates that the system is highly doped. In the classical regime, massless Dirac fermions behave like massive particles and the mass is determined by the Fermi level.

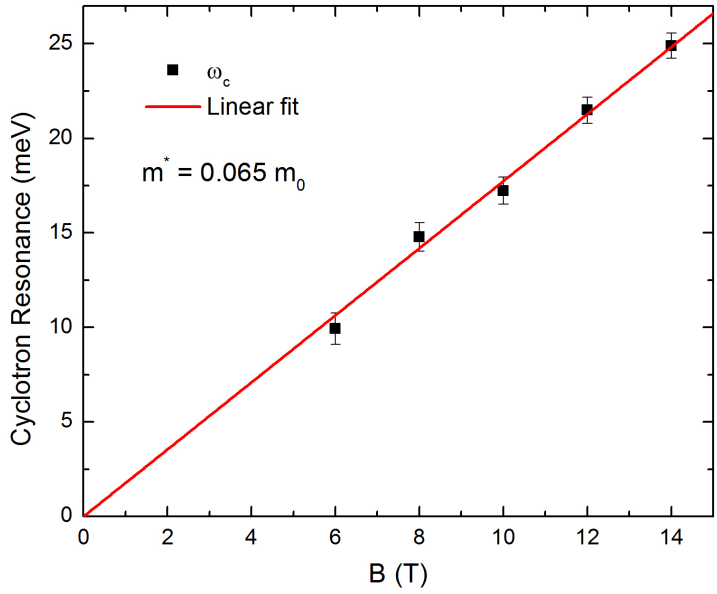

Figure 40: CR energies plotted as a function of magnetic field. Effective mass of $m^* = 0.065 m_0$ is extracted from the linear fit (solid red line).

The linear-in-B dependence of CR can be interpreted as the intraband transitions. Consider that the Fermi level is located in the conduction band. At a given magnetic field, the spacing between adjacent Landau levels is quite small near the Fermi level for highly doped graphene. The Fermi level can be estimated by the expression as

$$E_F \approx E_n = v_F\sqrt{2e\hbar Bn} = E_1\sqrt{n}, \tag{71}$$

where E_n is the nth Landau level energy and E_1 is the magnetic energy. The Fermi level is between the nth Landau level and the $(n+1)$th Landau level. n is a large number for highly doped graphene. The intraband transition energy is given by

$$\omega_c = E_{n+1} - E_n = E_1(\sqrt{n+1} - \sqrt{n}) = \frac{E_1}{\sqrt{n+1} + \sqrt{n}} \approx \frac{E_1}{2\sqrt{n}}. \tag{72}$$

According to Eq. 71,

$$\sqrt{n} = \frac{E_F}{E_1}. \tag{73}$$

Then, we have the linear-in-B dependence CR

$$\omega_c \approx \frac{E_1}{2\sqrt{n}} = \frac{E_1}{2E_F/E_1} = \frac{E_1^2}{2E_F} = \frac{\hbar e B}{E_F/v_F^2}. \tag{74}$$

Figure 41 shows the extracted parameters σ_B (panel (a)) and γ_B (panel (b)) from the fits to relative transmission spectra. σ_B decreases slightly with increasing magnetic field while γ_B remains constant to some extent. Zero-field $\sigma_0 = 2.5 \times 10^{-3}\Omega^{-1}$ and $\gamma_0 = 12$ meV are used to ensure the best fit. In addition, these two parameters together with the obtained E_F satisfy the following formula given by Boltzmann transport theory,

$$\sigma_0 = \frac{2e^2}{h}\frac{E_F}{\gamma_0}. \tag{75}$$

4.1.3 Plasmons in graphene structures

Plasmons result from the collective oscillations of electrons. They have a profound impact on the properties of materials, especially on their interaction with electromagnetic radiation. They play a fundamental role in the research on optical materials. The theory for collective description of electrons in condensed matters was first established in the early 1950s [109, 110]. Experimentally, they were further developed in the 1980s and 1990s [10, 11, 111].

Figure 42 shows the observation of plasmon resonance in the disk array of selectively doped GaAs/AlGaAs heterostructures containing 2-dimensional electron gas.

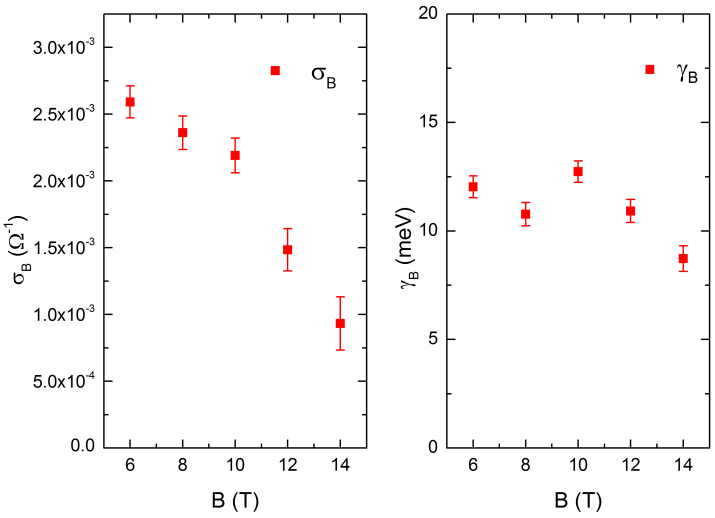

Figure 41: (a) σ_B decreases slightly with increasing magnetic field. (b) γ_B remains constant to some extent.

The zero-field plasmon frequency in disks is given by [10]

$$\omega_p^2 = \frac{n_s e^2 \pi}{2am^*(\epsilon_0 + \epsilon_1)}, \tag{76}$$

where n_s, e, and m^* are the 2D electron density, charge, and effective mass, respectively. a is the disk radius. ϵ_0 and ϵ_1 are dielectric constants of vacuum and GaAs in which the heterostructures are imbedded. Note that the plasmon frequency $\omega_p \propto \sqrt{n_s}$. With an external magnetic field perpendicular to the sample surface, the plasmon resonance in disks will split into two modes, given by [10]

$$\omega_\pm = \pm\frac{\omega_c}{2} + \sqrt{\frac{\omega_c^2}{4} + \omega_p^2}, \tag{77}$$

where "+" ("-") corresponds to the higher (lower) mode and $\omega_c = (eB)/m^*$ is the cyclotron resonance energy.

Unlike plasmons confined in disks, the plasmon energy of conventional 2-dimensional electron gas (2DEG) in ribbon structure is written as [11, 112, 113, 114]

$$\omega_p^2 = \frac{n_s e^2}{2\epsilon_0 \epsilon_1 m^*} q, \tag{78}$$

where $q = (2n+1)\pi/w\,(n = 1, 2, ...)$ is the quantized wave vector. w is the width of the ribbon. In the magnetic field, there is only one hybrid mode, the resonance

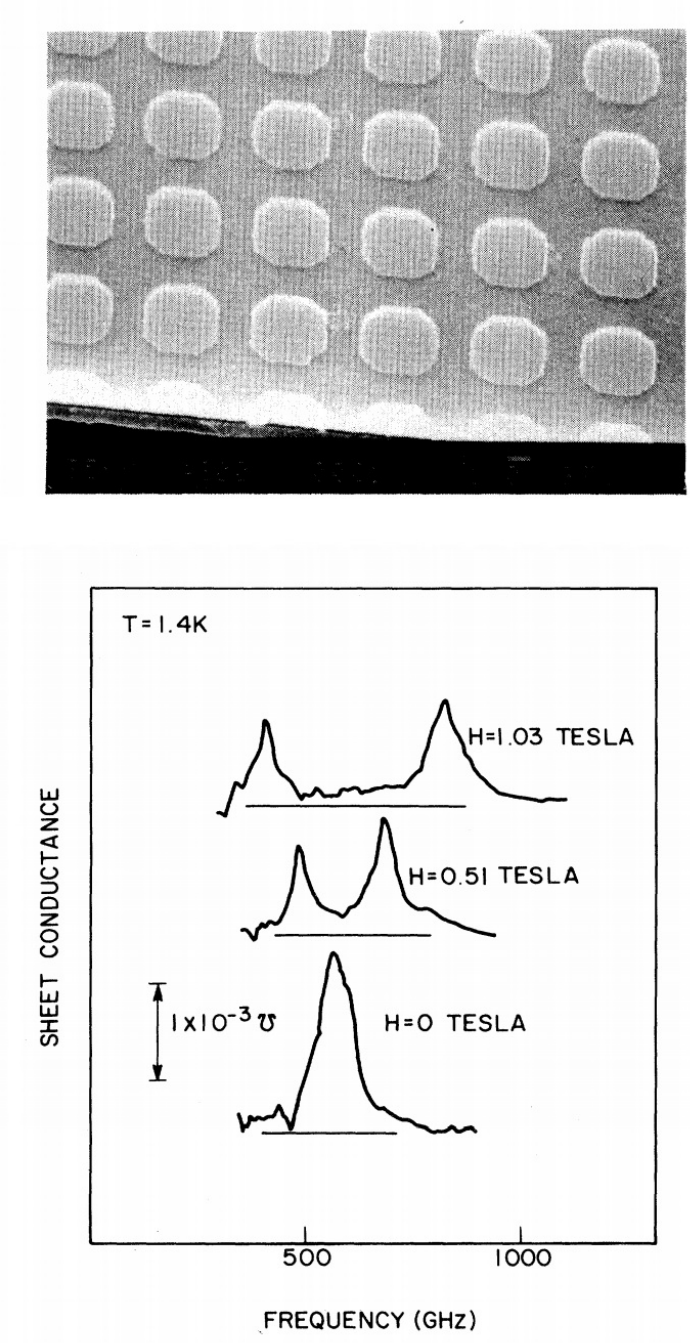

Figure 42: Top panel: disk array of selectively doped GaAs/AlGaAs heterostructures on GaAs substrate containing the two-dimensional electron gas. The bottom panel: sheet conductance of array as a function of frequency. Magnetic field is perpendicular to the surface. Reprinted with permission from [10]. Copyright (1983) by the American Physical Society [1].

frequency reads [112, 115]

$$\omega_h^2 = \omega_p^2 + \omega_c^2. \tag{79}$$

Figure 43 shows the relative transmission spectra of a doped AlGaAs/GaAs ribbon array, in the case that the electric field of the infrared radiation is perpendicular to the ribbon. The plasmon resonance is observed. When the radiation is polarized parallel to the ribbon, $q = \pi/w$ approaches zero and no resonance is observed.

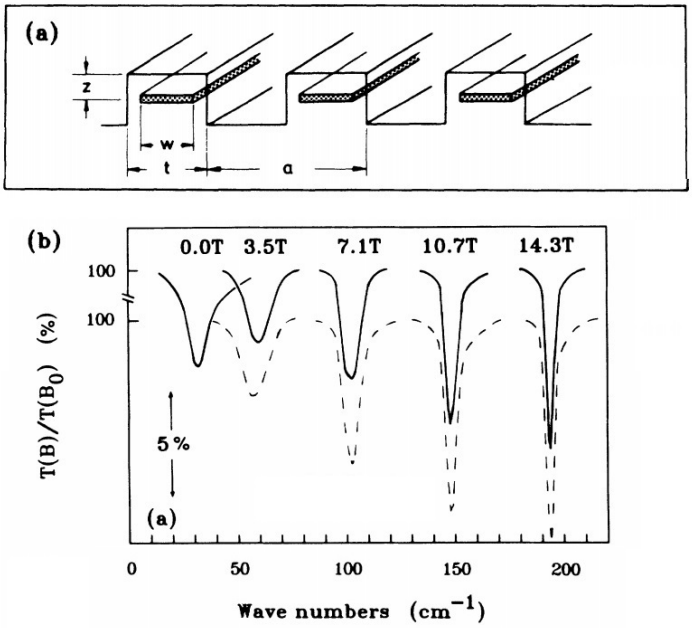

Figure 43: (a) Schematics of ribbon array. (b) Relative transmission spectra of ribbon array. The solid lines show the spectra when the light polarization is perpendicular to the ribbon. The dashed lines show the spectra when the light polarization is parallel to the ribbon. Reprinted with permission from [11]. Copyright (1988) by the American Physical Society [1].

As we can see, plasmons of a normal 2DEG in disks and ribbons behave quite differently in a magnetic field. Assume that the carriers with cyclotron mass m_c are

[1]Readers may view, browse, and/or download material for temporary copying purposes only, provided these uses are for noncommercial personal purposes. Except as provided by law, this material may not be further reproduced, distributed, transmitted, modified, adapted, performed, displayed, published, or sold in whole or part, without prior written permission from the American Physical Society.

confined by a parabolic potential:

$$V(x,y) = \frac{1}{2} m_c(\omega_x^2 x^2 + \omega_y^2 y^2), \tag{80}$$

where ω_x (ω_y) is the plasmon frequency in the x (y) direction at zero magnetic field. In the case that the plasmon confined in disks is excited by unpolarized light, $\omega_x = \omega_y = \omega_p$. The collective excitation of N charged particles with mass m_c and charge e can be simulated as that of a single particle with mass Nm_c and charge Ne [116, 117, 118]. Therefore, the dynamic conductivity of collective particles can be calculated based on a single particle theory. The motion of a single particle in the magnetic field B driven by the electric field $E(t) = E_0 e^{-i\omega t}$ of the infrared light can be described by the following equation:

$$\begin{aligned} m_c\ddot{x} + m_c\Gamma\dot{x} + m_c\omega_x^2 x &= eE_0 e^{-i\omega t} + e\dot{y}B, \\ m_c\ddot{y} + m_c\Gamma\dot{y} + m_c\omega_y^2 y &= -e\dot{x}B, \end{aligned} \tag{81}$$

where Γ_x (Γ_y) is the scattering rate. Here, we assume the electric field is along the x direction. Let

$$x = x_0 e^{-i\omega t},\ y = y_0 e^{-i\omega t}, \tag{82}$$

then Eq. 81 can be rewritten as

$$\begin{aligned} -m_c\omega^2 x_0 - i\omega m_c\Gamma_x x_0 + m_c\omega_x^2 x_0 &= eE_0 - i\omega eBy_0, \\ -m_c\omega^2 y_0 - i\omega m_c\Gamma_y y_0 + m_c\omega_y^2 y_0 &= i\omega eBx_0. \end{aligned} \tag{83}$$

With $\omega_c = eB/m_c$, Eq. 83 can be further simplified to

$$\begin{aligned} (-\omega^2 - i\omega\Gamma_x + \omega_x^2)x_0 + i\omega\omega_c y_0 &= \frac{eE_0}{m_c}, \\ (-\omega^2 - i\omega\Gamma_y + \omega_y^2)y_0 &= i\omega\omega_c x_0. \end{aligned} \tag{84}$$

By solving Eq. 84, we get

$$x_0 = \frac{eE_0}{m_c} \frac{-\omega^2 - i\omega\Gamma_y + \omega_y^2}{(-\omega^2 - i\omega\Gamma_x + \omega_x^2)(-\omega^2 - i\omega\Gamma_y + \omega_y^2) - \omega^2\omega_c^2}. \tag{85}$$

The current density $j(\omega)$ is given by

$$j(\omega) = j_0 e^{-i\omega t} = ne\dot{x} = nex_0(-i\omega)e^{-i\omega t}. \tag{86}$$

Thus,

$$j_0 = nex_0(-i\omega). \tag{87}$$

In the end, the conductivity $\sigma(\omega)$ can be written as

$$\begin{aligned}\sigma(\omega) &= \frac{j(\omega)}{E(\omega)} = \frac{j_0}{E_0} = \frac{-i\omega nex_0}{E_0} \\ &= \frac{-i\omega ne^2}{m_c} \frac{-\omega^2 - i\omega\Gamma_y + \omega_y^2}{(-\omega^2 - i\omega\Gamma_x + \omega_x^2)(-\omega^2 - i\omega\Gamma_y + \omega_y^2) - \omega^2\omega_c^2}.\end{aligned} \tag{88}$$

In the disks, the plasmons can be excited by unpolarized light. Therefore, we can assume $\omega_x = \omega_y = \omega_p$ and $\Gamma_x = \Gamma_y = \Gamma$. Finally, Eq. 88 can be rewritten as

$$\sigma(\omega) = \frac{ne^2}{m_c} \frac{-i\omega(-\omega^2 - i\omega\Gamma + \omega_p^2)}{(-\omega^2 - i\omega\Gamma + \omega_p^2)^2 - \omega^2\omega_c^2}. \tag{89}$$

The real part of the dynamic conductivity $\sigma(\omega)$ is given by

$$\mathrm{Re}\sigma(\omega) = \frac{ne^2}{m_c}\left[\frac{\omega^2\Gamma}{(\omega^2 - \omega\omega_c - \omega_p^2)^2 + \omega^2\Gamma^2} + \frac{\omega^2\Gamma}{(\omega^2 + \omega\omega_c - \omega_p^2)^2 + \omega^2\Gamma^2}\right]. \tag{90}$$

Apparently, the resonance will occur at the frequency ω satisfying the following equation:

$$\begin{aligned}\omega^2 - \omega\omega_c - \omega_p^2 = 0, or \\ \omega^2 + \omega\omega_c - \omega_p^2 = 0.\end{aligned} \tag{91}$$

By solving Eq. 91, we obtain the resonance frequencies $\omega_\pm$ in Eq. 77. The plasmon confined in disks splits into two modes. The difference between these two modes equals to the cyclotron resonance ω_c. The full width at half maximum (FWHM) $\Delta\omega_\pm$ can also be derived from Eq. 90

$$\begin{aligned}\Delta\omega_\pm &= \omega_{\pm,1} - \omega_{\pm,2} \\ &= \Gamma \pm \frac{2\omega_c\Gamma}{\sqrt{4\omega_p^2 + (\omega_c + \Gamma)^2} + \sqrt{4\omega_p^2 + (\omega_c - \Gamma)^2}},\end{aligned} \tag{92}$$

where $\omega_{\pm,1}$ and $\omega_{\pm,2}$ are the two solutions to $\mathrm{Re}\sigma(\omega) = \frac{1}{2}\mathrm{Re}\sigma(\omega_{\pm})$.

Assume the ribbon is in the y direction. When the light is polarized in the x direction, $\omega_x = \omega_p$, $\Gamma_x = \Gamma$, and $\omega_y = \Gamma_y = 0$. In such a case, Eq. 88 can be simplified to

$$\sigma(\omega) = \frac{ne^2}{m_c} \frac{-i\omega}{(-\omega^2 - i\omega\Gamma + \omega_p^2) + \omega_c^2}. \tag{93}$$

And the real part of $\sigma(\omega)$ is given by

$$\mathrm{Re}(\sigma) = \frac{\omega^2\Gamma}{(\omega^2 - \omega_c^2 - \omega_p^2)^2 + \omega^2\Gamma^2}. \tag{94}$$

Therefore, the plasmon confined in the ribbons has only one mode in the magnetic field with resonance frequency $\omega_h^2 = \omega_p^2 + \omega_c^2$.

In recent years, plasmonics has attracted a great deal of attention. It could give rise to a large amount of exciting and novel phenomena. It is one of the most promising pathways to realize the nanophotonics and holds great potential for applications. However, the enormous loss in the conventional plasmonic materials restricts its development. This problem was always a hindrance to the researcher until the successful isolation of graphene. Plasmons in graphene are tunable via changing the carrier density by applying a gate voltage or via changing the dimension of graphene structures. The loss can be quite low because of its extremely high mobility. The optical confinement can be very high making it possible to control light at scales smaller than the wavelength. All of the superiorities make graphene one of the most promising candidates for plasmonic applications.

Theoretically, the plasmon mode ω_p can be obtained from the zeros of the dielectric function. We assume each electron in the graphene moves in the external field as well as the induced field of all electrons. This model is known as random-phase approximation (RPA) and it is used to calculate the famous Lindhard dielectric function for a three-dimensional [119] and two-dimensional electron gas [120].

In the RPA model, the polarizability is given by [120]

$$\prod(q,\omega) = -\frac{g_s g_v}{L^2}\sum_{\mathbf{k}ss'}\frac{f_{s\mathbf{k}} - f_{s'\mathbf{k}'}}{\omega + \epsilon_{s\mathbf{k}} - \epsilon_{s'\mathbf{k}'} + i\eta}F_{ss'}(\mathbf{k},\,\mathbf{k}'), \tag{95}$$

where $\mathbf{k}' = \mathbf{k} + \mathrm{q}$. $s = 1$ ($s' = -1$) indicates the conduction (valence) band. $F_{ss'}(\mathbf{k},\,\mathbf{k}') = (1 + ss'\cos\theta)/2$ is the overlap of states, where θ is the angle between $\mathbf{k}$ and $\mathbf{k}'$. $f_{sk} = \frac{1}{e^{\beta(\epsilon_{s\mathbf{k}}-\mu)}+1}$ is the Fermi distribution function. $\beta = 1/(k_B T)$ and μ is the chemical potential. $g_s = g_v = 2$ are the spin and valley degeneracies. $\epsilon_{s\mathbf{k}} = \hbar v_F|\mathbf{k}|$ is the corresponding energy of graphene. L^2 is the normalization area. After summing over ss', Eq. 95 can be rewritten as

$$\prod(q,\omega) = \prod^{+}(q,\omega) + \prod^{-}(q,\omega), \tag{96}$$

where

$$\begin{aligned}
\prod^{+} =& -\frac{g_s g_v}{2L^2}\sum_{k}\left[\frac{(f_{\mathbf{k}+} - f_{\mathbf{k}'+})(1+\cos\theta_{kk'})}{\omega + \epsilon_{\mathbf{k}+} - \epsilon_{\mathbf{k}'+} + i\eta}\right.\\
&\left. + \frac{f_{\mathbf{k}+}(1-\cos\theta_{kk'})}{\omega + \epsilon_{\mathbf{k}+} - \epsilon_{\mathbf{k}'-} + i\eta} + \frac{f_{\mathbf{k}'+}(1-\cos\theta_{kk'})}{\omega + \epsilon_{\mathbf{k}-} - \epsilon_{\mathbf{k}'+} + i\eta}\right],\\
\prod^{-} =& -\frac{g_s g_v}{2L^2}\sum_{k}\left[\frac{(f_{\mathbf{k}-} - f_{\mathbf{k}'-})(1+\cos\theta_{kk'})}{\omega + \epsilon_{\mathbf{k}-} - \epsilon_{\mathbf{k}'-} + i\eta}\right.\\
&\left. + \frac{f_{\mathbf{k}-}(1-\cos\theta_{kk'})}{\omega + \epsilon_{\mathbf{k}-} - \epsilon_{\mathbf{k}'+} + i\eta} + \frac{f_{\mathbf{k}'-}(1-\cos\theta_{kk'})}{\omega + \epsilon_{\mathbf{k}+} - \epsilon_{\mathbf{k}'-} + i\eta}\right].
\end{aligned} \tag{97}$$

At zero temperature, in the long-wavelength limit ($q \to 0$), we have the following forms:

$$\prod(q,\omega) \approx \begin{cases} \frac{D_0 v_F^2 q^2}{2\omega^2}[1 - \frac{\omega^2}{4E_F^2}], & v_F q < \omega < 2E_F \\ D_0[1 + \frac{i\omega}{v_F q}], & \omega < v_F q \end{cases} \tag{98}$$

where $D_0 = (g_s g_v n/\pi)^{1/2}/v_F$ is the density of states at the Fermi energy. n is the carrier density. $E_F = \hbar v_F k_F$ is the Fermi level. The dielectric function can be written as

$$\chi(q,\omega) = 1 + v_c(q)\prod(q,\omega), \tag{99}$$

where $v_c(q) = 2\pi e^2/(q\varepsilon)$ with $\varepsilon = (\varepsilon_0 + \varepsilon_1)/2$. ε_0 is the permittivity of the free space and ε_1 is the permittivity of the substrate. By solving the equation $\chi(q, \omega) = 0$, the plasmon frequency ω_p is found:

$$\omega_p = \sqrt{\frac{g_s g_v e^2 E_F}{2\epsilon} q},\ q \to 0. \tag{100}$$

The plasmon frequency ω_p has the same dispersion $\sqrt{q}$ as that of the conventional two-dimensional electron gas [121]. In graphene, the Fermi level E_F is given as

$$E_F = \hbar v_F k_F, \tag{101}$$

with

$$k_F = \sqrt{\frac{4\pi n}{g_s g_v}}. \tag{102}$$

Therefore, $\omega_p \propto \sqrt{E_F} \propto n^{1/4}$ compared with the classical two-dimensional plasmon behavior, where $\omega_p \propto \sqrt{n}$. This result is a direct consequence of the quantum relativistic nature of graphene and it is a signature of massless Dirac fermions [122, 123, 124].

The first experimental study of plasmons in graphene is reported by the group led by Prof. Feng Wang at UC Berkeley [12]. They performed Fourier transform infrared spectroscopy measurements on micro-ribbon arrays made out of CVD graphene and were able to tune the plasmon frequency via changing the carrier density or varying the width of the ribbon as shown in Figure 44.

The magnitude of the plasmon resonance in single layer graphene is relatively weak, limiting its applications [125]. A group from IBM [126] has demonstrated transparent photonic devices based on graphene/insulator stacks. They show that the plasmon resonance magnitude and frequency can be enhanced by doping multilayer epitaxial graphene effectively. Their research on such graphene/insulator stacks may lead to further development of plasmonic devices. Besides graphene ribbons [12, 127, 128] and disks [126, 129, 130], other structures such as rings [131] and hexagons [132] are also explored. What's more, magnetoplasmons in graphene disks [133] and in monolayer graphene grown on SiC [134] have been studied as well.

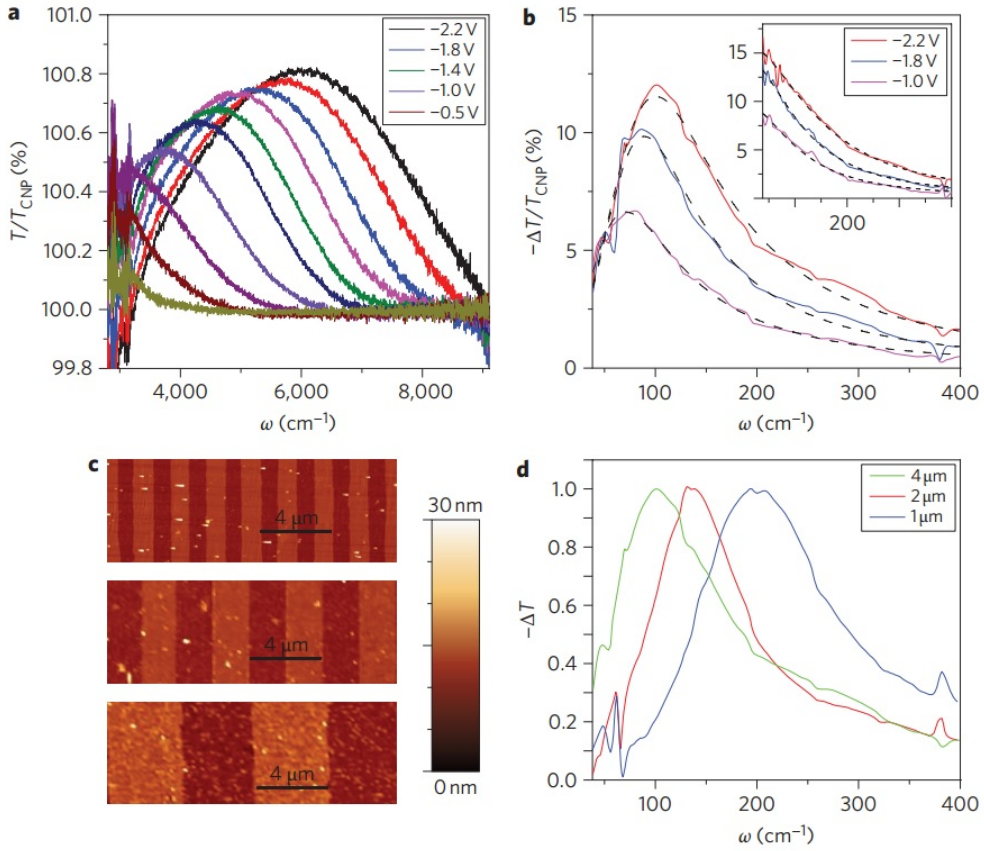

Figure 44: (a) Relative mid-infrared transmission spectra, T/T_{CNP}, of graphene ribbon array. T_{CNP} is the transmission spectrum of graphene at charge neutral point and T is the spectrum at different gate voltage. The plasmon frequency increases with increasing carrier density. (b) Tune the plasmon energy through the gate voltage. $\Delta T = T - T_{CNP}$. The infrared light was polarized perpendicular to the ribbons. The dashed lines show the best fit using a damped oscillator model as $\mathrm{Im}(-\omega/(\omega^2 - \omega_p^2 + i\omega\Gamma_p))$The inset shows the spectra when the infrared light was polarized parallel to the ribbons. The Drude absorption was observed. (c) AFM images of samples. The widths of ribbons are 1μm, 2μm, and 4μm, respectively. (d) The plasmon frequency varies in graphene ribbons of different width. Reprinted from Ref. [12].

The common ground with all these studies is that the graphene is in the quasiclassical regime. The carriers in highly doped graphene are more like massive particles and the behavior of plasmons is governed by classical law as we discussed above. The very unique features of quasineutral graphene arising from the massless Dirac fermions are not presented. We performed an infrared magneto-spectroscopy study of graphene ribbon arrays fabricated out of undoped multilayer epitaxial graphene

in the quantum regime. We succeeded in demonstrating the collective excitations of massless Dirac fermions and observed distinct deviations from the inter-Landau-level transition in magnetic field resulting from massless carriers in quasineutral graphene [135].

4.2 Experiments and Discussions

4.2.1 Experimental Method

The graphene nanoribbon (GNR) arrays are made out of the multilayer graphene epitaxially grown on the C-face of SiC. As we discuss in Section 4.1.2.1, the first few graphene layers at the graphene-SiC interface are highly doped due to charge transfer from SiC, while the subsequent layers are undoped and electronically isolated [2, 9, 38, 91]. The graphene ribbons are fabricated by the method described in Section 2.2. The length of ribbons is 400 μm and the widths are 50 nm, 100 nm, and 200 nm, respectively (Figure 45). The width-to-gap ratio w/d of graphene ribbon array is kept $1:1$. w is the width of GNR and d is the gap between adjacent ribbons. Each array is 400 μm $\times$ 400 μm. On each substrate, there are four identical arrays consisting of ribbons of the same width and the spacing between the arrays is 100 μm (Figure 45 (a)).

The experimental setup is similar to that shown in Figure 16. A superconducting magnet is used. The magnetic field is normal to the surface of the sample. The infrared transmission measurement is performed via a commercial Fourier transform infrared spectrometer (Bruker IFS 113v). The infrared light is generated by a mercury lamp. In order to reduce the amount of stray infrared light, an aperture $\sim 1\text{mm}^2$ is placed on the substrate. For the measurement with polarized infrared light, a polarizer is placed between the cone and the sample to polarize the infrared light. The electric field E of the light is either parallel to the ribbon ($E \parallel y$) or perpendicular to the ribbon ($E \parallel x$) as shown in Figure 46.

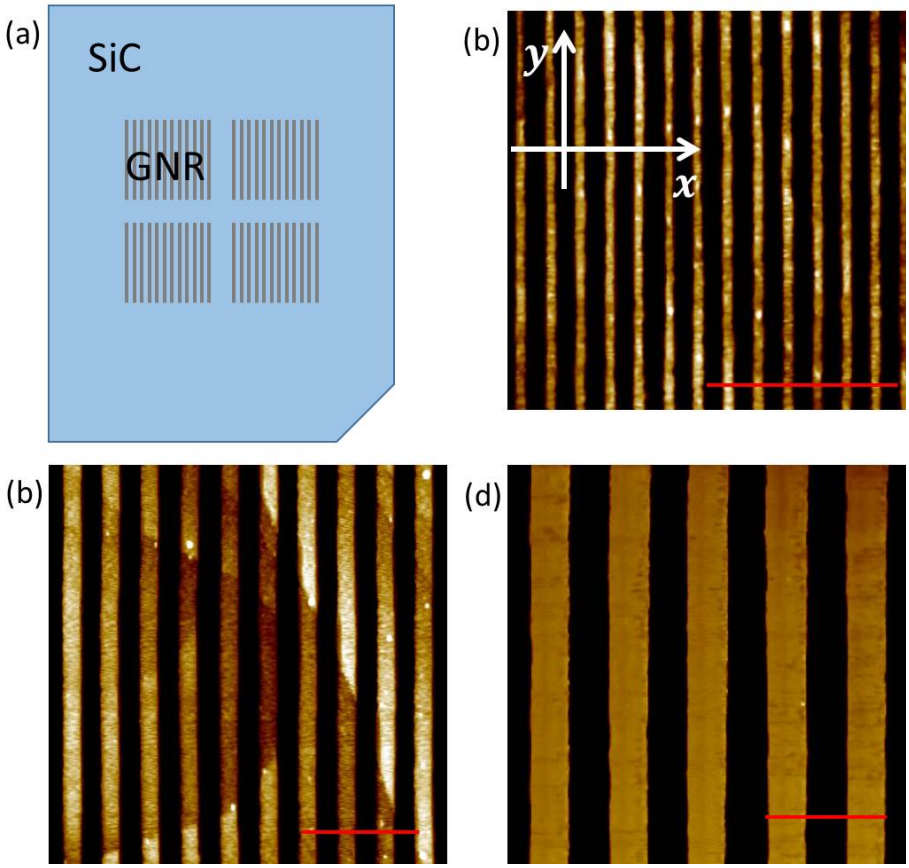

Figure 45: (a) Schematics of four graphene ribbon arrays on the substrate. (b) AFM image of 50 nm-wide ribbons. (c) AFM image of 100 nm-wide ribbons. (d) AFM image of 200 nm-wide ribbons. The bright area shows the ribbons and the black part is the gap. The scale bar is 0.6 μm.

4.2.2 Results and Analysis

First, we study the unpatterned two-dimensional (2D) graphene film as a reference. The reference sample undergoes all the fabrication processes (coating resist, vacuum annealing *et al.*) in order for an accurate comparison. Figure 47 (a) shows the relative transmission spectra $T(B)/T(0)$ of the reference sample at various magnetic fields. An obvious cyclotron resonance (CR) absorption dip is observed which corresponds to the inter-Landau-level transition $LL_{-1(0)} \rightarrow LL_{0(1)}$. Still, the resonance feature can be fit using a single Lorentzian model described in Section 4.1.2 (dotted red line). The CR can be resolved at magnetic field down to 0.2 T indicating that the Fermi level

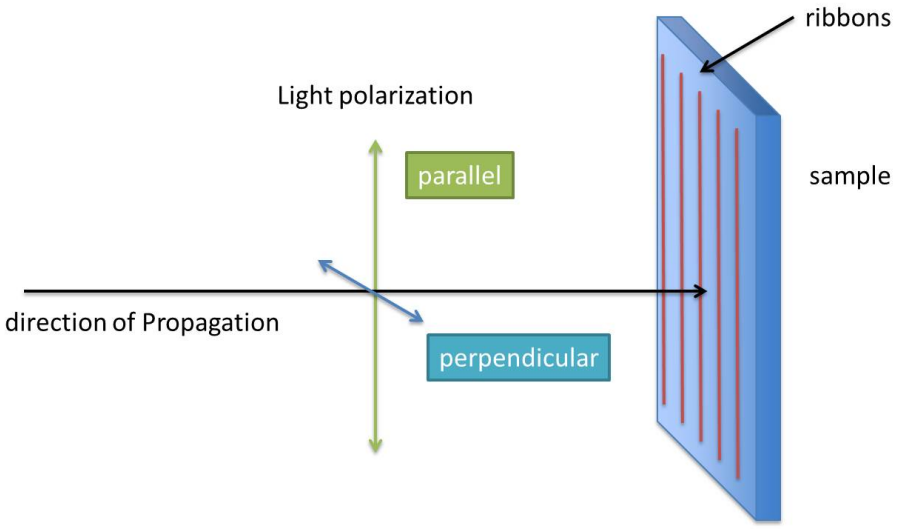

Figure 46: The light is polarized before reaching the sample. The polarization is either parallel or perpendicular to the ribbon direction.

of graphene is $E_F \leq 17$ meV. The mobility is estimated to be $\mu > 50\,000\,\mathrm{cm^2V^{-1}s^{-1}}$ under the classical condition $\mu B > 1$. At high magnetic field, there is another CR-like feature that appears in the low frequency range. This CR probably originates from the graphene grown on the Si-face of SiC (the back side of the substrate). During the growth of multilayer epitaxial graphene on the C-face, 1 - 2 graphene layers will be grown on the Si-face which is confirmed by our Raman spectroscopy measurement.

Figure 47 (b) shows the CR energy extracted from the Lorentzian fit to the relative transmission spectra. The CR energy exhibits characteristic $\sqrt{B}$ dependence. A linear fit (solid red line) yields the Fermi velocity of $v_F = (1.02 \pm 0.01) \times 10^6$ m/s which agrees with our previous study presented in Section 4.1.2.1 as well as other reported works[2, 21, 33, 37].

Here, we want to emphasize that the Fermi level E_F in our samples is more than one order of magnitude smaller than that reported in previous works on graphene plasmons [12, 126, 127, 128, 129, 130, 133, 134]. In addition, the high value of mobility suggests that multilayer epitaxial graphene is an ideal system for studying plasmons of massless Dirac fermions.

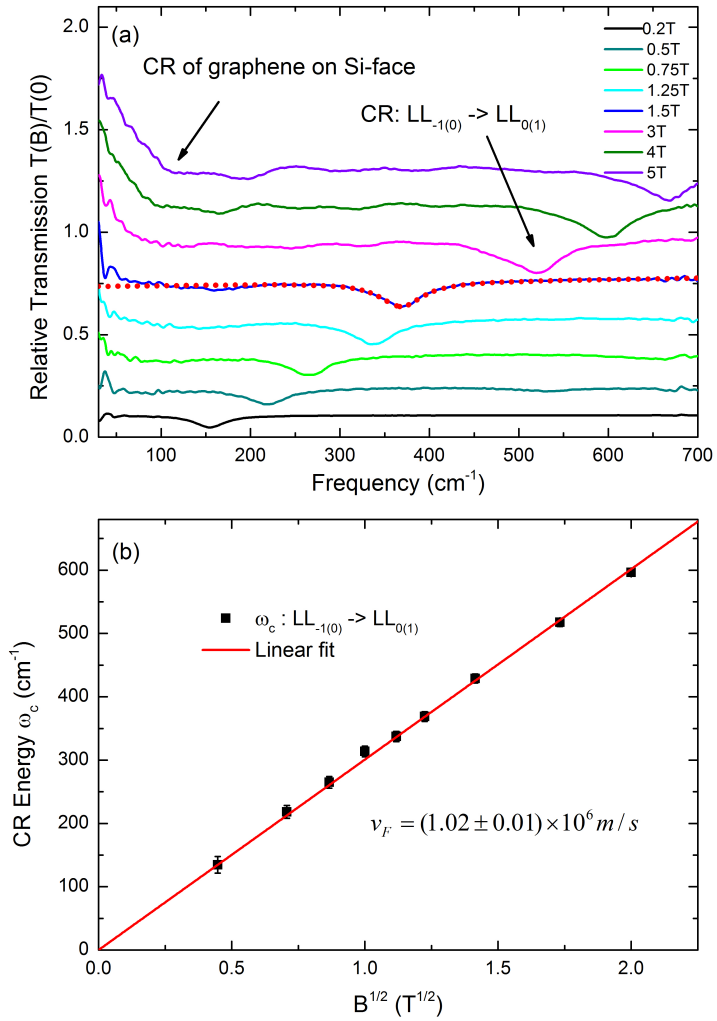

Figure 47: (a) Relative transmission spectra of 2D graphene film at different magnetic fields. The spectra is vertically shifted for clarity. Inter-Landau-level transition $LL_{-1(0)} \rightarrow LL_{0(1)}$ in multilayer epitaxial graphene on C-face is observed as well as intra-Landau-level transition in graphene on Si-face. The dotted red line represents the Lorentzian fit to the CR resonance lineshape. (b) The CR energy $(LL_{-1(0)} \rightarrow LL_{0(1)})$ is plotted as a function of $\sqrt{B}$. The red solid line represents the best linear fit.

In the following discussion, we will focus on the transmission spectra of graphene nanoribbon arrays. Figure 48 shows the extinct transmission spectra $1-T(\mathrm{GNR})/T(\mathrm{SiC})$ of 100nm-wide ribbon at zero magnetic field. The infrared light is polarized parallel or perpendicular to the ribbon direction. In both cases, no plasmon resonance is observed. Instead, the spectra show a Drude-like absorption feature probably due to the graphene grown on the silicon-face (the back side of the substrate). As the carrier

density n_s in the quasineutral graphene is very low ($\sim 2.1 \times 10^{10}\,\mathrm{cm}^{-2}$), the strength of plasmon resonance in the GNR is probably too weak to be observed.

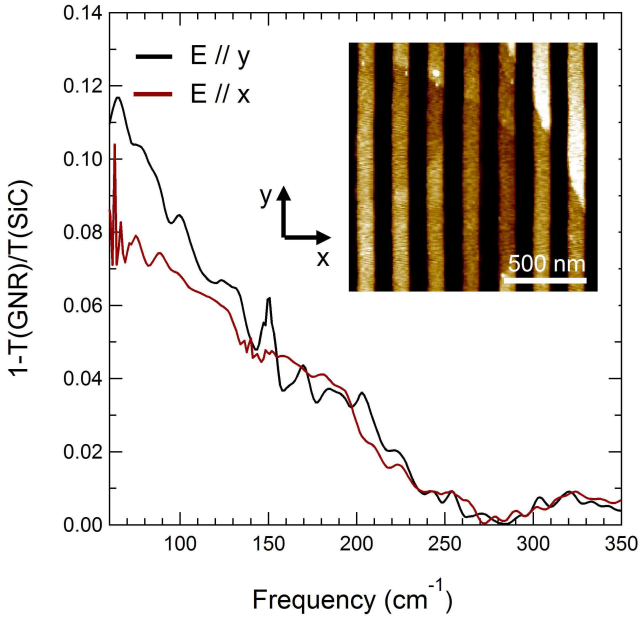

Figure 48: Extinct transmission spectra $1 - T(GNR)/T(SiC)$ of 100nm-wide GNR array sample. Solid red line shows the spectrum when the electric field of the light is parallel to the ribbon direction while solid black line shows the spectrum with $E \parallel x$. Inset: AFM image of 100nm-wide ribbons.

In order to probe the plasmon in our quasineutral GNR arrays, we apply a magnetic field perpendicular to the sample surface. In such a case, the plasmon ω_p will couple with the CR ($LL_{-1(0)} \rightarrow LL_{0(1)}$), forming the upper hybrid mode (UHM) with energy ω_h which disperses as [31, 136, 137]

$$\omega_h(q, B) = \sqrt{\omega_c^2(B) + \omega_p^2(q)}, \tag{103}$$

where $q = \pi/w$ is the wave vector and w is the width of GNR.

Figure 49 shows the relative transmission spectra $T(B)/T(0)$ of 2D graphene (solid black line), 100nm-wide GNR array (solid blue line), and 50nm-wide GNR array (solid red line) at selective magnetic fields. The spectra are measured with unpolarized infrared light. The inter-Landau-level transition $LL_{-1(0)} \rightarrow LL_{0(1)}$ is observed in all

the samples. As we can see, the resonance lineshape of GNR array samples is clearly blueshifted with respect to that of 2D graphene due to the formation of UHM. The energy shift is more pronounced at low magnetic field. Because $\omega_p \propto q^{1/2} \propto w^{-1/2}$, the narrower GNR holds plasmon of higher energy. According to Eq. 103, the energy shift increases with decreasing width of GNR. In addition, the amplitude of UHM decreases also with the width of GNR. In Figure 49, the spectra of 50nm-wide GNR and 100nm-wide GNR are scaled by a factor of 30 and 10, respectively. Due to the reduction, we can not observe UHM in the GNR at very low magnetic field.

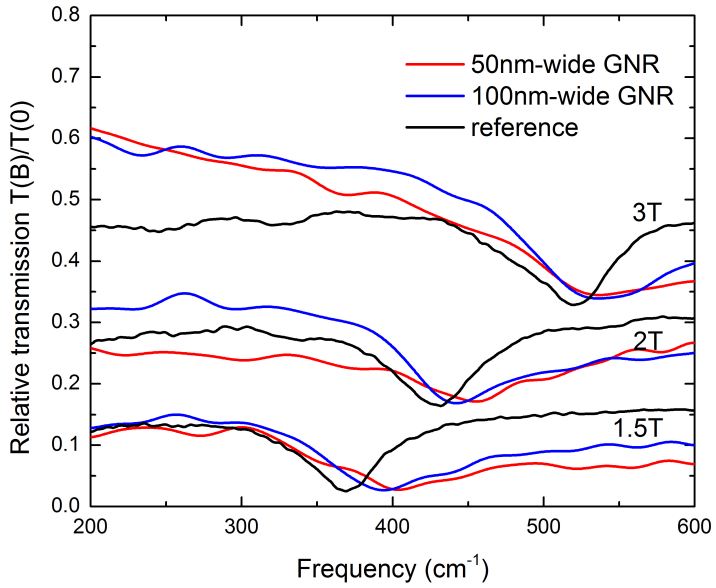

Figure 49: Relative transmission spectra $T(B)/T(0)$ of 2D reference sample, 100nm-wide GNR, and 50nm-wide GNR at selective magnetic fields. The spectra of 100nm-wide GNR is scaled by a factor of 10 while the spectra of 50nm-wide GNR is multiplied by 30. The curves are shifted for clarity.

It is predicted that the plasmon energy can interchange between adjacent ribbons, known as plasmon cross-talk, in dense GNR arrays with $w/d > 2$ [138, 139]. Figure 50 shows the relative transmission spectra of GNR arrays consisting of 100nm-wide ribbons with $w/d = 2:1$ and $w/d = 1:1$ at select magnetic fields. The resonance almost occurs at the same frequency indicating that the plasmon cross-talk effect can be largely neglected in our study.

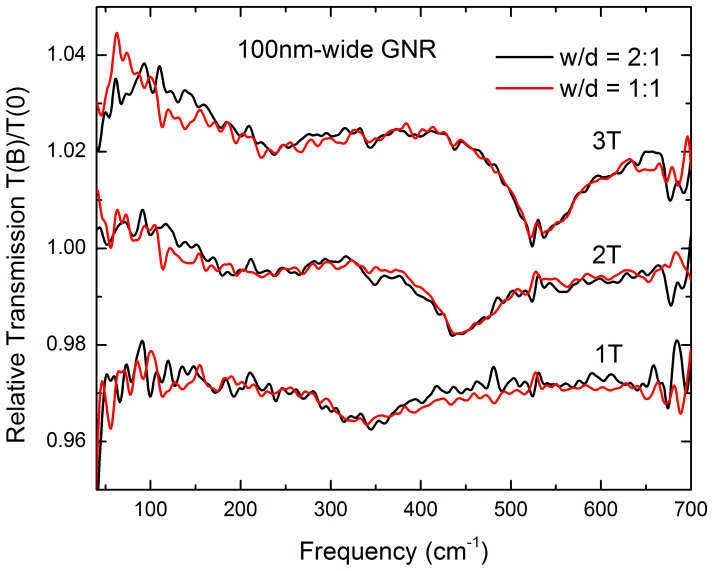

Figure 50: Relative transmission spectra $T(B)/T(0)$ of GNR arrays consisting of 100nm-wide ribbons with $w/d = 2:1$ (solid black line) and $w/d = 1:1$ (solid red line). The curves are vertically shifted for clarity. The resonance absorption dips almost coincide with each other, revealing no plasmon cross-talk effect.

The relative transmission spectra of GNR arrays is fitted by a single Lorentzian model described above and the resonance energy ω_h is obtained. Eq. 103 can be rewritten as

$$\omega_h^2(q, B) = \omega_c^2(B) + \omega_p^2(q), \tag{104}$$

with $\omega_c = v_F\sqrt{2e\hbar B}$. Therefore, ω_h^2 is linear with respect to B with slope $2e\hbar v_F^2$ and non-zero intercept ω_p^2. We plot ω_h^2 as a function of B shown in Figure 51 (a). For comparison, ω_c^2 of 2D graphene is exhibited as well. Clearly, ω_h^2 shows the linear-in-B dependence and can be described quite well by a linear fit with $v_F = 1.02 \times 10^6$ m/s. The extracted values of ω_p are summarized in Table 1. As we can see, even the plasmon energy of 50nm-wide GNR array is comparable to the CR energy at 0.2 T, the lowest magnetic field at which the resonance can be observed. Therefore, the UHM energy is dominated by the contribution from the CR. At high magnetic field, $\omega_h \approx \omega_c$. So, the energy shift $\omega_h - \omega_c$ we observe in the relative transmission spectra decreases with increasing magnetic field.

To better reveal the UHM dispersion, it is instructive to plot ω_h in units of v_F/l_B, as a function of ql_B as shown in Figure 51 (b). $l_B = \sqrt{\hbar/eB}$ is the magnetic length. In this way, the CR line collapses on a single point at $q = 0$ and the dispersion of UHM is highlighted. The solid lines show the best fits using Eq. 103. In the low field limit, Eq. 103 becomes insufficient to describe graphene magnetoplsmons as the UHM approaches the diagonal line $\omega = v_F q$, separating regions of interband and intraband excitations. Contrary to conventional 2DEG, $\omega_p > v_F q$ in quasineutral graphene is valid for any value of q. The UHM can never enter the intraband particle-hole continuum defined by frequencies $\omega < v_F q$ but only the interband regime, where it is weakly Landau damped and merges into one of the linear magnetoplasmons [140, 141, 142].

The UHM dispersion relation can also be investigated by considering the UHM energy shift with respect to the CR energy of 2D graphene. In the limit $\omega_p \ll \omega_c$, $\omega_h - \omega_c$ can be written as

$$\omega_h - \omega_c = \omega_c(\sqrt{1 + \frac{\omega_p^2}{\omega_c^2}} - 1) \approx \frac{1}{2}\frac{\omega_p^2}{\omega_c}, \tag{105}$$

where we Taylor expand Eq. 103 to the linear order. The Taylor expansion is valid if the plasmon energy is small compared to the CR energy. In our case,

$$\frac{\omega_p^2}{\omega_c^2} = \frac{\alpha_G E_F}{\hbar v_F} q l_B \leq \alpha_G < 1, \tag{106}$$

where $\alpha_G = 2.2/\epsilon$ is the fine structure constant of graphene. Therefore, Eq. 108 holds within our experimental parameter range and measurement accuracy. With

$$\begin{aligned} \omega_p &= \sqrt{\frac{2e^2 E_F}{4\pi\epsilon_0\epsilon} q}, \\ \omega_c &= v_F\sqrt{2e\hbar B} = \sqrt{2}\hbar\frac{v_F}{l_B}, \end{aligned} \tag{107}$$

the energy shift in units of Coulomb energy $e^2/(4\pi\epsilon_0\epsilon l_B)$ can be rewritten as

$$\frac{\omega_h - \omega_c}{e^2/(4\pi\epsilon_0\epsilon l_B)} \simeq \frac{E_F}{\sqrt{2}\hbar v_F} q l_B^2 \propto \frac{1}{wB}, \tag{108}$$

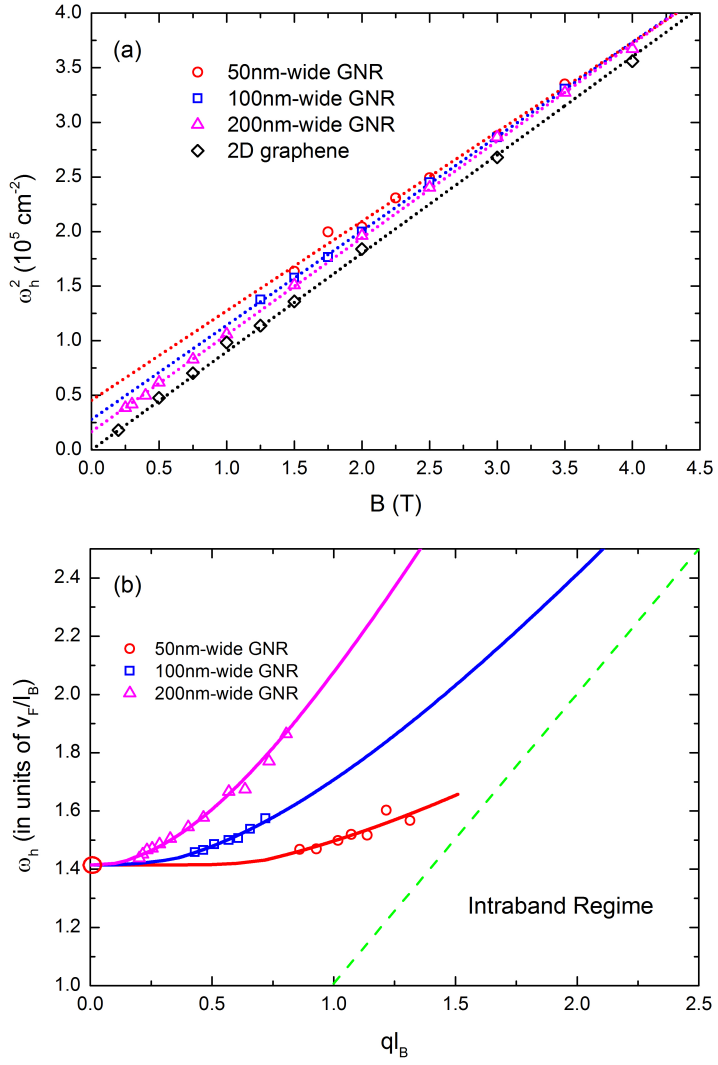

Figure 51: (a) ω_h^2 (ω_c^2) plotted as a function of B. The dotted lines show the best fits using Eq. 104 with $v_F = 1.02 \times 10^6$ m/s. (b) UHM energy ω_h in units of v_F/l_B plotted as a function of ql_b. The CR energy ω_c of 2D graphene collapse on a single point (red circle) at $q = 0$. The solid lines represent the best fits to the data using Eq. 104. The dashed green line defined by equation $E = \hbar v_F q$ separates the interband and intraband excitations.

where ϵ_0 is the vacuum permittivity, $\epsilon = (\epsilon_{SiC} + 1)/2 \approx 5$ is the relative permittivity of epitaxial graphene. Figure 52 shows the energy shift in units of Coulomb energy as a function of ql_B^2. There is a small vertical offset for different GNR arrays which is not predicted by Eq. 108. The offset is about 1.5% of the CR energy at $B = 4$T for the 100nm-wide GNR. In our analysis, we consider a simple model using the dispersion relation of the plasmon mode for 2D graphene (Eq. 100) and replacing the wave

vector by $q = \pi/w$ to account for the GNR geometry. This model provides insight about the dispersion and gives ql_B^2 scaling. Further corrective geometric terms, such as those discussed in Ref. [138], may give rise to the small offset in the data taken from GNR arrays with ribbons of different width. Apart from the vertical offset, all data collapse on a single line as shown in Figure 52 (b). Eq. 108 can fit the data quite well (dotted line). $E_F = 17 \pm 2$ meV is obtained from the results of the fitting which is in very good agreement with our estimation from 2D graphene.

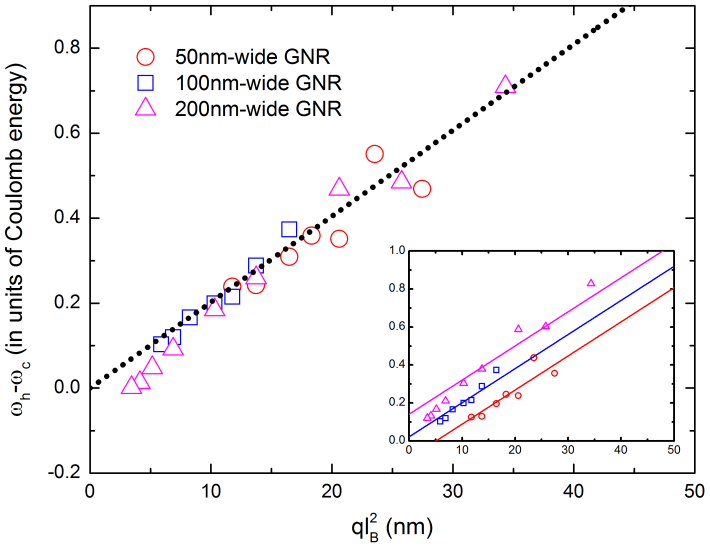

Figure 52: Inset: The energy shift in units of Coulomb energy in the GNR array sample as a function of ql_B^2. Main panel: Apart form a small offset, the data collapse on a single line. The dotted line and the solid lines represent the best linear fit with $v_F = 1.02 \times 10^6$ m/s.

The scaling behavior $\propto ql_B^2$ is unique to the UHM in graphene in the quantum regime and can serve as the signature of massless Dirac fermions. In the conventional 2DEG or highly doped graphene, the CR energy is given by

$$\omega_c = \frac{eB}{m^*}. \tag{109}$$

And the plasmon energy can be written as [11]

$$\omega_p = \sqrt{\frac{Ne^2}{2\epsilon\epsilon_0 m^*}q}, \tag{110}$$

where N is the carrier density. Therefore, the energy shift in units of Coulomb energy reads

$$\frac{\omega_h - \omega_c}{e^2/(4\pi\epsilon_0\epsilon l_B)} \approx \frac{1}{2}\frac{\omega_p^2}{\omega_c} = N\pi q l_B^3. \tag{111}$$

Thus, ql_B^3 scaling is expected. This unique behavior in quasineutral graphene also helps us exclude other interpretations of our data such as magnetoexcitons [143, 144, 145, 146]. Magnetoexcitons may be understood as inter-Landau-level transitions acquiring a weak dispersion, as a function of the electron-hole wave vector, due to the mutual Coulomb interaction. For small values of $ql_B \ll 1$, the magnetoexciton-induced energy shift scales with ql_B which does not match our experimental result as shown in Figure 52.

Finally, we discuss the polarization-resolved measurements. Figure 53 shows the relative transmission spectra of 200nm-wide GNR array (a) and 100nm-wide GNR array (b) at selective magnetic fields. The spectra are measured using polarized infrared light. The electric field of the radiation is either parallel ($E \parallel y$) or perpendicular ($E \parallel x$) to the ribbon direction. Because the linear polarizer reduces the intensity of the infrared light and the CR absorption is weak, we can not observe any resonance feature in the relative transmission spectra of the 50nm-wide GNR array measured using the polarized light. The resonance lineshape can be described using a single Lorentz model (dotted line). For both 200nm-wide and 100nm-wide GNR arrays, the energy of UHM is higher in $E \parallel x$ polarization than that in $E \parallel y$ polarization. The FWHM in $E \parallel x$ polarization is much broader compared with that in $E \parallel y$ polarization.

Similarly, the resonance energy ω_h is extracted from the Lorentzian fit to the relative transmission spectra. ω_h in units of v_F/l_B is plotted as a function of ql_B in Figure 54 (a) and the data can be fitted using Eq. 103 with $v_F = 1.02 \times 10^6$ m/s (dotted line). The values of ω_p from the results of the fit are summarized in Table 1. In figure 54, the energy shift $\omega_h - \omega_c$ in units of Coulomb energy is plotted as a function

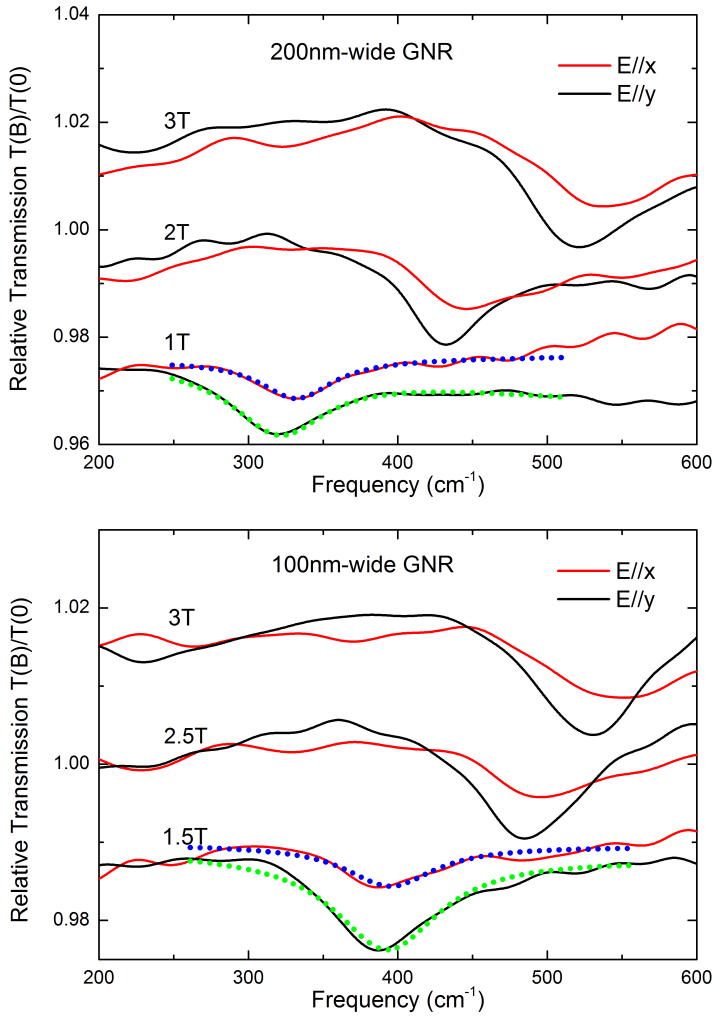

Figure 53: (a) Relative transmission spectra of 200nm-wide GNR array with infrared light polarized either parallel or perpendicular to the ribbon direction. (b) Relative transmission spectra of 100nm-wide GNR array with polarized infrared light. The dotted lines represent the best fits using a single Lorentzian model.

of ql_B^2. ql_B^2 scaling still holds for both polarizations except for the small offset. The vertical offset is similar to that found in the unpolarized measurement, which indicates that additional geometric corrections to Eq. 103 depend on the ribbon direction with respect to the polarization direction. This polarization-dependent behavior of UHM was not observed in the previously study on quasi-1D quantum wires [11, 147].

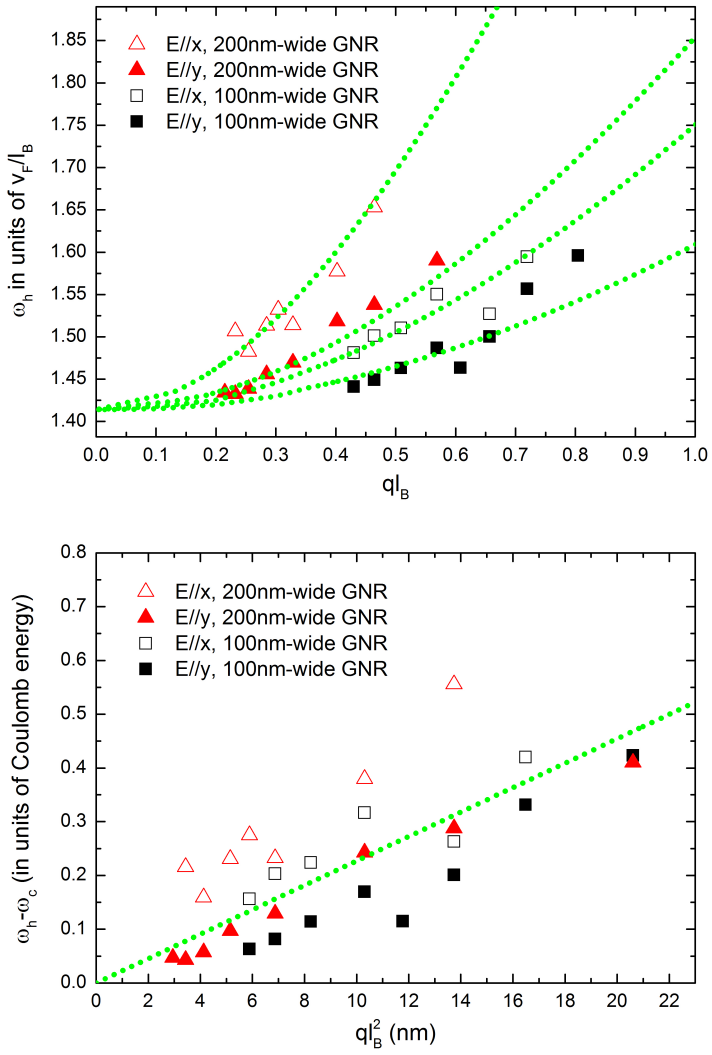

Figure 54: (a) The energy of UHM in units of v_F/l_B plotted as a function of ql_B. (b) The energy shift of UHM with respect to the CR energy in 2D graphene versus ql_B^2. The dotted lines show the best fits using Eq. 103 with $v_F = 1.02 \times 10^6$ m/s.

4.3 Conclusion

In conclusion, we fabricated large-scale GNR arrays out of multilayer epitaxial graphene grown on the C-face of SiC. We studied the plasmon properties of graphene via Fourier transform infrared spectroscopy in the magnetic field. Multilayer epitaxial graphene is quasineutral and each layer behaves like isolated undoped graphene. The carriers exhibit unique properties of massless Dirac fermions in the magnetic field. The inter-Landau-level transition has characteristic $\sqrt{B}$ dependence. The Fermi level of

Table 1: Plasmon energy ω_p extracted from Figure 51 and Figure 54.

$\omega_p(\mathrm{cm}^{-1})$	Width and thickness: 200nm and 72Å	100nm and 128Å	100nm and 104Å	50nm and 61Å
Unpolarized	126	149	143	172
Perpendicular $E \parallel x$	154	171	...	...
Parallel $E \parallel y$	104	133	...	...

$E_F \leq 17\,\mathrm{meV}$ is estimated as well as the mobility of $\mu > 50\,000\,\mathrm{cm}^2\mathrm{V}^{-1}\mathrm{s}^{-1}$. Such a high value of mobility guarantees longer lifetime and much less loss than the conventional plasmonic materials.

Three different GNR arrays are fabricated consisting of ribbons with widths of 50nm, 100nm, and 200nm, respectively. For the 100nm-wide GNR array, the UHM energy is within the range from $300\,\mathrm{cm}^{-1}$ to $610\,\mathrm{cm}^{-1}$ in our experiment, corresponding to the wavelength $\lambda_{IR} \approx 16 - 33\,\mu\mathrm{m}$. Thus, $\lambda_{IR}/\lambda_{plasmon} \approx \lambda_{IR}/2w \approx 80 - 165$. The strong reduction in plasmon wavelength is consistent with the theoretical prediction. The high degree of optical confinement is achieved in our study.

We show that the graphene plasmon can couple with the CR, forming an UHM and resulting in a blueshift with respect to the CR energy of 2D graphene. The observed energy shift exhibits a peculiar ql_B^2 scaling, which is one of the distinct properties of massless Dirac fermions. This signature phenomenon helps us distinguish the plasmon of quasineutral graphene from that in conventional two-dimensional electron gas and in highly doped graphene.

CHAPTER V

CONCLUSION

Graphene has a unique band structure. The conduction band and valence band touch at the Dirac points making graphene a zero-gap semiconductor. Close to the Dirac points, graphene has linear energy dispersion with constant Fermi velocity $\sim 10^6$ m/s and carriers' behavior is described by the Dirac function for massless Dirac fermions. In an external magnetic field B, quantized Landau levels of graphene scale with $\sqrt{B}$ and an unusual $n = 0$ Landau level appears. Graphite consists of graphene layers. In a magnetic field, carriers at the H point of the graphite Brillouin zone behave like Dirac fermions due to the effectively vanishing interlayer coupling, while at the K point of the graphite Brillouin zone, Landau levels scale with B in the low energy range.

The first part of the thesis relates to the infrared magneto-spectroscopy study of ultrathin graphite flakes. Within the measured frequency range, four distinct inter-Landau-Level transitions are observed arising from the carriers at the H point and the K point of the graphite Brillouin zone. Our interest is focused on the electron-phonon coupling. The CR of Dirac-like carriers corresponding to the Landau-level transition $H : n = -1 \rightarrow 0$ can be tuned via magnetic field. The CR will interact with phonons ($K - A_1'$ phonon or $\Gamma - E_{1u}$ phonon) when the CR energy is close to the phonon energy. The coupling between the CR and the $K - A_1'$ phonon is strong leading to the "anti-crossing" phenomenon. With increasing magnetic field, the weight of the lower branch will transfer gradually to the upper branch. The interaction between the CR and $\Gamma - E_{1u}$ phonon is relatively weak with the coupling parameter λ one order of magnitude smaller. The weak coupling gives rise to magnetophonon resonance which

exhibits an asymmetry lineshape in the relative transmission spectra. The Fano-like feature evolves from an anti-resonance peak to a resonance dip with increasing magnetic field and can be described well by the Fano formula. Both of the EPC's can be explained by a standard two-coupled-mode model.

The second part of this thesis explores the magnetoplasmons in quasineutral multilayer epitaxial graphene nanoribbon arrays via infrared spectroscopy. Multilayer graphene is in the quantum regime with high mobility of $\mu > 50\,000\,\mathrm{cm}^2/(\mathrm{V}\cdot\mathrm{s})$. We fabricated large-scale GNR arrays with various widths (50 nm, 100 nm, and 200 nm). The plasmon energy $\omega_p \propto n^{1/4}$ in graphene compared to $\omega_p \propto n^{1/2}$ in a conventional two-dimensional electron gas, which is a signature of massless Dirac fermions. In magnetic field, the plasmon will couple with the CR forming the upper-hybrid mode and resulting in a blueshift with respect to the energy of the CR. The energy shift exhibits a characteristic ql_B^2 scaling while ql_B^3 scaling is expected in a conventional two-dimensional electron gas. We demonstrate that the graphene plasmon has long lifetime with a high degree of optical confinement (80-165 for 100nm-wide ribbons). It can also be tuned via varying the width of ribbons or magnetic field. These advantages make graphene a promising candidate material for plasmonic applications.

REFERENCES

[1] P. Blake, E. W. Hill, A. H. Castro Neto, K. S. Novoselov, D. Jiang, R. Yang, T. J. Booth, and A. K. Geim, "Making graphene visible," *Applied Physics Letters* **91**, (2007).

[2] M. L. Sadowski, G. Martinez, M. Potemski, C. Berger, and W. A. de Heer, "Landau Level Spectroscopy of Ultrathin Graphite Layers," *Phys. Rev. Lett.* **97**, 266405 (2006).

[3] E. A. Henriksen, Z. Jiang, L.-C. Tung, M. E. Schwartz, M. Takita, Y.-J. Wang, P. Kim, and H. L. Stormer, "Cyclotron Resonance in Bilayer Graphene," *Phys. Rev. Lett.* **100**, 087403 (2008).

[4] L.-C. Tung, P. Cadden-Zimansky, J. Qi, Z. Jiang, and D. Smirnov, "Measurement of graphite tight-binding parameters using high-field magnetoreflectance," *Phys. Rev. B* **84**, 153405 (2011).

[5] M. Orlita, C. Faugeras, J. M. Schneider, G. Martinez, D. K. Maude, and M. Potemski, "Graphite from the Viewpoint of Landau Level Spectroscopy: An Effective Graphene Bilayer and Monolayer," *Phys. Rev. Lett.* **102**, 166401 (2009).

[6] C. Faugeras, M. Amado, P. Kossacki, M. Orlita, M. Sprinkle, C. Berger, W. A. de Heer, and M. Potemski, "Tuning the Electron-Phonon Coupling in Multilayer Graphene with Magnetic Fields," *Phys. Rev. Lett.* **103**, 186803 (2009).

[7] D. L. Miller, K. D. Kubista, G. M. Rutter, M. Ruan, W. A. de Heer, P. N. First, and J. A. Stroscio, "Observing the Quantization of Zero Mass Carriers in Graphene," *Science* **324**, 924 (2009).

[8] J. Kedzierski, P.-L. Hsu, P. Healey, P. Wyatt, C. Keast, M. Sprinkle, C. Berger, and W. A. de Heer, "Epitaxial Graphene Transistors on SiC Substrates," *Electron Devices, IEEE Transactions on* **55**, 2078 (2008).

[9] M. Sprinkle, D. Siegel, Y. Hu, J. Hicks, A. Tejeda, A. Taleb-Ibrahimi, P. Le Fèvre, F. Bertran, S. Vizzini, H. Enriquez, S. Chiang, P. Soukiassian, C. Berger, W. A. de Heer, A. Lanzara, and E. H. Conrad, "First Direct Observation of a Nearly Ideal Graphene Band Structure," *Phys. Rev. Lett.* **103**, 226803 (2009).

[10] S. J. Allen, H. L. Störmer, and J. C. M. Hwang, "Dimensional resonance of the two-dimensional electron gas in selectively doped GaAs/AlGaAs heterostructures," *Phys. Rev. B* **28**, 4875 (1983) http://journals.aps.org/prb/abstract/10.1103/PhysRevB.28.4875.

[11] T. Demel, D. Heitmann, P. Grambow, and K. Ploog, "Far-infrared response of one-dimensional electronic systems in single- and two-layered quantum wires," *Phys. Rev. B* **38**, 12732 (1988) http://journals.aps.org/prb/abstract/10.1103/PhysRevB.38.12732.

[12] L. Ju, B. Geng, J. Horng, C. Girit, M. Martin, Z. Hao, H. A. Bechtel, X. Liang, A. Zettl, Y. R. Shen, and F. Wang, "Graphene plasmonics for tunable terahertz metamaterials," *Nat Nano* **6**, 630 (2011).

[13] A. H. Castro Neto, F. Guinea, N. M. R. Peres, K. S. Novoselov, and A. K. Geim, "The electronic properties of graphene," *Rev. Mod. Phys.* **81**, 109 (2009).

[14] S. Reich, J. Maultzsch, C. Thomsen, and P. Ordejón, "Tight-binding description of graphene," *Phys. Rev. B* **66**, 035412 (2002).

[15] R. S. Deacon, K.-C. Chuang, R. J. Nicholas, K. S. Novoselov, and A. K. Geim, "Cyclotron resonance study of the electron and hole velocity in graphene monolayers," *Phys. Rev. B* **76**, 081406 (2007).

[16] P. R. Wallace, "The Band Theory of Graphite," *Phys. Rev.* **71**, 622 (1947).

[17] J. W. McClure, "Band Structure of Graphite and de Haas-van Alphen Effect," *Phys. Rev.* **108**, 612 (1957).

[18] J. C. Slonczewski and P. R. Weiss, "Band Structure of Graphite," *Phys. Rev.* **109**, 272 (1958).

[19] J. W. McClure, "Energy Band Structure of Graphite," *IBM Journal of Research and Development* **8**, 255 (1964).

[20] G. W. Semenoff, "Condensed-Matter Simulation of a Three-Dimensional Anomaly," *Phys. Rev. Lett.* **53**, 2449 (1984).

[21] Y. Zhang, Y.-W. Tan, H. L. Stormer, and P. Kim, "Experimental observation of the quantum Hall effect and Berry's phase in graphene," *Nature* **438**, 201 (2005).

[22] E. McCann and V. I. Fal'ko, "Landau-Level Degeneracy and Quantum Hall Effect in a Graphite Bilayer," *Phys. Rev. Lett.* **96**, 086805 (2006).

[23] N. B. Brandt, S. M. Chudinov, and Y. G. Ponomarev, *Semimetals: Graphite and Its Compounds (Modern Problems in Condensed Matter Sciences)* (Elsevier Science Ltd, 1988).

[24] M. S. Dresselhaus and G. Dresselhaus, "Intercalation compounds of graphite," *Advances in Physics* **51**, 1 (2002).

[25] E. McCann, "Asymmetry gap in the electronic band structure of bilayer graphene," *Phys. Rev. B* **74**, 161403 (2006).

[26] E. V. Castro, K. S. Novoselov, S. V. Morozov, N. M. R. Peres, J. M. B. L. dos Santos, J. Nilsson, F. Guinea, A. K. Geim, and A. H. C. Neto, "Biased Bilayer Graphene: Semiconductor with a Gap Tunable by the Electric Field Effect," *Phys. Rev. Lett.* **99**, 216802 (2007).

[27] T. Ohta, A. Bostwick, T. Seyller, K. Horn, and E. Rotenberg, "Controlling the Electronic Structure of Bilayer Graphene," *Science* **313**, 951 (2006).

[28] M. Dresselhaus and G. Dresselhaus, "Intercalation compounds of graphite," *Advances in Physics* **30**, 139 (1981).

[29] L. M. Zhang, Z. Q. Li, D. N. Basov, M. M. Fogler, Z. Hao, and M. C. Martin, "Determination of the electronic structure of bilayer graphene from infrared spectroscopy," *Phys. Rev. B* **78**, 235408 (2008).

[30] J. W. McClure, "Diamagnetism of Graphite," *Phys. Rev.* **104**, 666 (1956).

[31] M. O. Goerbig, "Electronic properties of graphene in a strong magnetic field," *Rev. Mod. Phys.* **83**, 1193 (2011).

[32] S. Das Sarma, S. Adam, E. H. Hwang, and E. Rossi, "Electronic transport in two-dimensional graphene," *Rev. Mod. Phys.* **83**, 407 (2011).

[33] K. S. Novoselov, A. K. Geim, S. V. Morozov, D. Jiang, M. I. Katsnelson, I. V. Grigorieva, S. V. Dubonos, and A. A. Firsov, "Two-dimensional gas of massless Dirac fermions in graphene," *Nature* **438**, 197 (2005).

[34] T. Ando, A. B. Fowler, and F. Stern, "Electronic properties of two-dimensional systems," *Rev. Mod. Phys.* **54**, 437 (1982).

[35] Z. Jiang, E. A. Henriksen, L. C. Tung, Y.-J. Wang, M. E. Schwartz, M. Y. Han, P. Kim, and H. L. Stormer, "Infrared Spectroscopy of Landau Levels of Graphene," *Phys. Rev. Lett.* **98**, 197403 (2007).

[36] E. A. Henriksen, P. Cadden-Zimansky, Z. Jiang, Z. Q. Li, L.-C. Tung, M. E. Schwartz, M. Takita, Y.-J. Wang, P. Kim, and H. L. Stormer, "Interaction-Induced Shift of the Cyclotron Resonance of Graphene Using Infrared Spectroscopy," *Phys. Rev. Lett.* **104**, 067404 (2010).

[37] A. M. Witowski, M. Orlita, R. Stępniewski, A. Wysmołek, J. M. Baranowski, W. Strupiński, C. Faugeras, G. Martinez, and M. Potemski, "Quasiclassical cyclotron resonance of Dirac fermions in highly doped graphene," *Phys. Rev. B* **82**, 165305 (2010).

[38] M. Orlita, C. Faugeras, P. Plochocka, P. Neugebauer, G. Martinez, D. K. Maude, A.-L. Barra, M. Sprinkle, C. Berger, W. A. de Heer, and M. Potemski, "Approaching the Dirac Point in High-Mobility Multilayer Epitaxial Graphene," *Phys. Rev. Lett.* **101**, 267601 (2008).

[39] P. Plochocka, C. Faugeras, M. Orlita, M. L. Sadowski, G. Martinez, M. Potemski, M. O. Goerbig, J.-N. Fuchs, C. Berger, and W. A. de Heer, "High-Energy Limit of Massless Dirac Fermions in Multilayer Graphene using Magneto-Optical Transmission Spectroscopy," *Phys. Rev. Lett.* **100**, 087401 (2008).

[40] M. Koshino and T. Ando, "Magneto-optical properties of multilayer graphene," *Phys. Rev. B* **77**, 115313 (2008).

[41] J. M. Pereira, F. M. Peeters, and P. Vasilopoulos, "Landau levels and oscillator strength in a biased bilayer of graphene," *Phys. Rev. B* **76**, 115419 (2007).

[42] K.-C. Chuang, A. M. R. Baker, and R. J. Nicholas, "Magnetoabsorption study of Landau levels in graphite," *Phys. Rev. B* **80**, 161410 (2009).

[43] F. Guinea, A. H. Castro Neto, and N. M. R. Peres, "Electronic states and Landau levels in graphene stacks," *Phys. Rev. B* **73**, 245426 (2006).

[44] J. W. McClure, "Theory of Diamagnetism of Graphite," *Phys. Rev.* **119**, 606 (1960).

[45] N. A. Goncharuk and L. Smrka, "Tight-binding description of Landau levels of graphite in tilted magnetic fields," *Journal of Physics: Condensed Matter* **24**, 185503 (2012).

[46] M. Rowan-Robinson, *Night Vision: Exploring the Infrared Universe* (Cambridge University Press, 2013).

[47] P. Griffiths, "Fourier transform infrared spectrometry," *Science* **222**, 297 (1983).

[48] W. D. Perkins, "Fourier transform-infrared spectroscopy: Part l. Instrumentation," *Journal of Chemical Education* **63**, A5 (1986).

[49] J. A. d. H. P. R. Griffiths, *Fourier Transform Infrared Spectrometry* (Wiley, New York, 1986).

[50] S. J. Allen, D. C. Tsui, and J. V. Dalton, "Far-Infrared Cyclotron Resonance in the Inversion Layer of Silicon," *Phys. Rev. Lett.* **32**, 107 (1974).

[51] P. Hoffmann and E. Knözinger, "Dynamic Range Problems in Fourier Transform IR and Far-IR Spectroscopy," *Appl. Spectrosc.* **41**, 1303 (1987).

[52] H. Namatsu, Y. Takahashi, K. Yamazaki, T. Yamaguchi, M. Nagase, and K. Kurihara, "Three-dimensional siloxane resist for the formation of nanopatterns with minimum linewidth fluctuations," *Journal of Vacuum Science and Technology B* **16** (1998).

[53] S. Ryu, M. Y. Han, J. Maultzsch, T. F. Heinz, P. Kim, M. L. Steigerwald, and L. E. Brus, "Reversible Basal Plane Hydrogenation of Graphene," *Nano Letters* **8**, 4597 (2008).

[54] S. Engelsberg and J. R. Schrieffer, "Coupled Electron-Phonon System," *Phys. Rev.* **131**, 993 (1963).

[55] A. C. Ferrari, "Raman spectroscopy of graphene and graphite: Disorder, electron-phonon coupling, doping and nonadiabatic effects," *Solid State Communications* **143**, 47 (2007), Exploring graphene recent research advances.

[56] S.-i. Tanaka, M. Matsunami, and S.-i. Kimura, "An investigation of electron-phonon coupling via phonon dispersion measurements in graphite using angle-resolved photoelectron spectroscopy," *Sci. Rep.* **3** (2013).

[57] J. Yan, S. Goler, T. D. Rhone, M. Han, R. He, P. Kim, V. Pellegrini, and A. Pinczuk, "Observation of Magnetophonon Resonance of Dirac Fermions in Graphite," *Phys. Rev. Lett.* **105**, 227401 (2010).

[58] Y. Kim, Y. Ma, A. Imambekov, N. G. Kalugin, A. Lombardo, A. C. Ferrari, J. Kono, and D. Smirnov, "Magnetophonon resonance in graphite: High-field Raman measurements and electron-phonon coupling contributions," *Phys. Rev. B* **85**, 121403 (2012).

[59] T. Ando, "Magnetic oscillation of optical phonon in graphene," *Journal of the Physical Society of Japan* **76** (2007).

[60] A. H. Castro Neto and F. Guinea, "Electron-phonon coupling and Raman spectroscopy in graphene," *Phys. Rev. B* **75**, 045404 (2007).

[61] M. O. Goerbig, J.-N. Fuchs, K. Kechedzhi, and V. I. Fal'ko, "Filling-Factor-Dependent Magnetophonon Resonance in Graphene," *Phys. Rev. Lett.* **99**, 087402 (2007).

[62] S. Piscanec, M. Lazzeri, F. Mauri, A. C. Ferrari, and J. Robertson, "Kohn Anomalies and Electron-Phonon Interactions in Graphite," *Phys. Rev. Lett.* **93**, 185503 (2004).

[63] M. Kühne, C. Faugeras, P. Kossacki, A. A. L. Nicolet, M. Orlita, Y. I. Latyshev, and M. Potemski, "Polarization-resolved magneto-Raman scattering of graphenelike domains on natural graphite," *Phys. Rev. B* **85**, 195406 (2012).

[64] M. Orlita, C. Faugeras, G. Martinez, D. K. Maude, M. L. Sadowski, and M. Potemski, "Dirac Fermions at the H Point of Graphite: Magnetotransmission Studies," *Phys. Rev. Lett.* **100**, 136403 (2008).

[65] C.-H. Park, F. Giustino, M. L. Cohen, and S. G. Louie, "Electron-Phonon Interactions in Graphene, Bilayer Graphene, and Graphite," *Nano Letters* **8**, 4229 (2008).

[66] J. Maultzsch, S. Reich, C. Thomsen, H. Requardt, and P. Ordejón, "Phonon Dispersion in Graphite," *Phys. Rev. Lett.* **92**, 075501 (2004).

[67] Z. Yao, C. L. Kane, and C. Dekker, "High-Field Electrical Transport in Single-Wall Carbon Nanotubes," *Phys. Rev. Lett.* **84**, 2941 (2000).

[68] C. S. Leem, C. Kim, S. R. Park, M.-K. Kim, H. J. Choi, C. Kim, B. J. Kim, S. Johnston, T. Devereaux, T. Ohta, A. Bostwick, and E. Rotenberg, "High-resolution angle-resolved photoemission studies of quasiparticle dynamics in graphite," *Phys. Rev. B* **79**, 125438 (2009).

[69] K. Nakao, "Landau Level Structure and Magnetic Breakthrough in Graphite," *Journal of the Physical Society of Japan* **40**, 761 (1976).

[70] W. W. Toy, M. S. Dresselhaus, and G. Dresselhaus, "Minority carriers in graphite and the H-point magnetoreflection spectra," *Phys. Rev. B* **15**, 4077 (1977).

[71] C. Faugeras, M. Amado, P. Kossacki, M. Orlita, M. Kühne, A. A. L. Nicolet, Y. I. Latyshev, and M. Potemski, "Magneto-Raman Scattering of Graphene on Graphite: Electronic and Phonon Excitations," *Phys. Rev. Lett.* **107**, 036807 (2011).

[72] Y. Kim, J. M. Poumirol, A. Lombardo, N. G. Kalugin, T. Georgiou, Y. J. Kim, K. S. Novoselov, A. C. Ferrari, J. Kono, O. Kashuba, V. I. Fal'ko, and D. Smirnov, "Measurement of Filling-Factor-Dependent Magnetophonon Resonances in Graphene Using Raman Spectroscopy," *Phys. Rev. Lett.* **110**, 227402 (2013).

[73] Z. Q. Li, S.-W. Tsai, W. J. Padilla, S. V. Dordevic, K. S. Burch, Y. J. Wang, and D. N. Basov, "Infrared probe of the anomalous magnetotransport of highly oriented pyrolytic graphite in the extreme quantum limit," *Phys. Rev. B* **74**, 195404 (2006).

[74] U. Fano, "Effects of Configuration Interaction on Intensities and Phase Shifts," *Phys. Rev.* **124**, 1866 (1961).

[75] T.-T. Tang, Y. Zhang, C.-H. Park, B. Geng, C. Girit, Z. Hao, M. C. Martin, A. Zettl, M. F. Crommie, S. G. Louie, Y. R. Shen, and F. Wang, "A tunable phonon-exciton Fano system in bilayer graphene," *Nat Nano* **5**, 32 (2010).

[76] A. B. Kuzmenko, L. Benfatto, E. Cappelluti, I. Crassee, D. van der Marel, P. Blake, K. S. Novoselov, and A. K. Geim, "Gate Tunable Infrared Phonon Anomalies in Bilayer Graphene," *Phys. Rev. Lett.* **103**, 116804 (2009).

[77] M. J. Rice and H.-Y. Choi, "Charged-phonon absorption in doped C60," *Phys. Rev. B* **45**, 10173 (1992).

[78] W. A. de Heer, C. Berger, M. Ruan, M. Sprinkle, X. Li, Y. Hu, B. Zhang, J. Hankinson, and E. Conrad, "Large area and structured epitaxial graphene produced by confinement controlled sublimation of silicon carbide," *Proceedings of the National Academy of Sciences* **108**, 16900 (2011).

[79] C. Berger, Z. Song, X. Li, X. Wu, N. Brown, C. Naud, D. Mayou, T. Li, J. Hass, A. N. Marchenkov, E. H. Conrad, P. N. First, and W. A. de Heer, "Electronic Confinement and Coherence in Patterned Epitaxial Graphene," *Science* **312**, 1191 (2006).

[80] X. Wu, X. Li, Z. Song, C. Berger, and W. A. de Heer, "Weak Antilocalization in Epitaxial Graphene: Evidence for Chiral Electrons," *Phys. Rev. Lett.* **98**, 136801 (2007).

[81] X. Wu, Y. Hu, M. Ruan, N. K. Madiomanana, J. Hankinson, M. Sprinkle, C. Berger, and W. A. de Heer, "Half integer quantum Hall effect in high mobility single layer epitaxial graphene," *Applied Physics Letters* **95**, (2009).

[82] B. Dlubak, M.-B. Martin, C. Deranlot, B. Servet, S. Xavier, R. Mattana, M. Sprinkle, C. Berger, W. A. De Heer, F. Petroff, A. Anane, P. Seneor, and A. Fert, "Highly efficient spin transport in epitaxial graphene on SiC," *Nat Phys* **8**, 557 (2012).

[83] W. A. de Heer, C. Berger, X. Wu, P. N. First, E. H. Conrad, X. Li, T. Li, M. Sprinkle, J. Hass, M. L. Sadowski, M. Potemski, and G. Martinez, "Epitaxial graphene," *Solid State Communications* **143**, 92 (2007), Exploring graphene recent research advances.

[84] Y.-M. Lin, C. Dimitrakopoulos, K. A. Jenkins, D. B. Farmer, H.-Y. Chiu, A. Grill, and P. Avouris, "100-GHz Transistors from Wafer-Scale Epitaxial Graphene," *Science* **327**, 662 (2010).

[85] SprinkleM, RuanM, HuY, HankinsonJ, M. Rubio Roy, ZhangB, WuX, BergerC, and W. A. de Heer, "Scalable templated growth of graphene nanoribbons on SiC," *Nat Nano* **5**, 727 (2010).

[86] P. N. First, W. A. de Heer, T. Seyller, C. Berger, J. A. Stroscio, and J.-S. Moon, "Epitaxial Graphenes on Silicon Carbide," *MRS Bulletin* **35**, 296 (2010).

[87] J. Baringhaus, M. Ruan, F. Edler, A. Tejeda, M. Sicot, I. AminaTaleb, A.-P. Li, Z. Jiang, E. H. Conrad, C. Berger, C. Tegenkamp, and W. A. de Heer, "Exceptional ballistic transport in epitaxial graphene nanoribbons," *Nature* **advance online publication** (2014).

[88] M. Orlita, I. Crassee, C. Faugeras, A. B. Kuzmenko, F. Fromm, M. Ostler, T. Seyller, G. Martinez, M. Polini, and M. Potemski, "Classical to quantum crossover of the cyclotron resonance in graphene: a study of the strength of intraband absorption," *New Journal of Physics* **14**, 095008 (2012).

[89] M. Orlita and M. Potemski, "Dirac electronic states in graphene systems: optical spectroscopy studies," *Semiconductor Science and Technology* **25**, 063001 (2010).

[90] M. Orlita, C. Faugeras, G. Martinez, D. Maude, J. Schneider, M. Sprinkle, C. Berger, W. de Heer, and M. Potemski, "Magneto-transmission of multi-layer epitaxial graphene and bulk graphite: A comparison," *Solid State Communications* **149**, 1128 (2009), Recent Progress in Graphene Studies.

[91] J. Hass, F. Varchon, J. E. Millán-Otoya, M. Sprinkle, N. Sharma, W. A. de Heer, C. Berger, P. N. First, L. Magaud, and E. H. Conrad, "Why Multilayer Graphene on 4H-SiC(000$\bar{1}$) Behaves Like a Single Sheet of Graphene," *Phys. Rev. Lett.* **100**, 125504 (2008).

[92] S. Latil, V. Meunier, and L. Henrard, "Massless fermions in multilayer graphitic systems with misoriented layers: ¡i¿Ab initio¡/i¿ calculations and experimental fingerprints," *Phys. Rev. B* **76**, 201402 (2007).

[93] J. M. B. Lopes dos Santos, N. M. R. Peres, and A. H. Castro Neto, "Graphene Bilayer with a Twist: Electronic Structure," *Phys. Rev. Lett.* **99**, 256802 (2007).

[94] N. H. Shon and T. Ando, "Quantum Transport in Two-Dimensional Graphite System," *Journal of the Physical Society of Japan* **67**, 2421 (1998).

[95] K. Chiu, T. Lee, and J. Quinn, "Infrared magneto-transmittance of a two-dimensional electron gas," *Surface Science* **58**, 182 (1976).

[96] T. Ando, "Theory of Cyclotron Resonance Lineshape in a Two-Dimensional Electron System," *Journal of the Physical Society of Japan* **38**, 989 (1975).

[97] Y. Zheng and T. Ando, "Hall conductivity of a two-dimensional graphite system," *Phys. Rev. B* **65**, 245420 (2002).

[98] R. Kubo, "Statistical-Mechanical Theory of Irreversible Processes. I. General Theory and Simple Applications to Magnetic and Conduction Problems," *Journal of the Physical Society of Japan* **12**, 570 (1957).

[99] T. Ando, Y. Zheng, and H. Suzuura, "Dynamical Conductivity and Zero-Mode Anomaly in Honeycomb Lattices," *Journal of the Physical Society of Japan* **71**, 1318 (2002).

[100] K. Bolotin, K. Sikes, Z. Jiang, M. Klima, G. Fudenberg, J. Hone, P. Kim, and H. Stormer, "Ultrahigh electron mobility in suspended graphene," *Solid State Communications* **146**, 351 (2008).

[101] X. Du, I. Skachko, A. Barker, and E. Y. Andrei, "Approaching ballistic transport in suspended graphene," *Nat Nano* **3**, 491 (2008).

[102] Y.-W. Tan, Y. Zhang, K. Bolotin, Y. Zhao, S. Adam, E. H. Hwang, S. Das Sarma, H. L. Stormer, and P. Kim, "Measurement of Scattering Rate and Minimum Conductivity in Graphene," *Phys. Rev. Lett.* **99**, 246803 (2007).

[103] K. Nomura and A. H. MacDonald, "Quantum Transport of Massless Dirac Fermions," *Phys. Rev. Lett.* **98**, 076602 (2007).

[104] E. H. Hwang, S. Adam, and S. Das Sarma, "Carrier Transport in Two-Dimensional Graphene Layers," *Phys. Rev. Lett.* **98**, 186806 (2007).

[105] A. Charrier, A. Coati, T. Argunova, F. Thibaudau, Y. Garreau, R. Pinchaux, I. Forbeaux, J.-M. Debever, M. Sauvage-Simkin, and J.-M. Themlin, "Solid-state decomposition of silicon carbide for growing ultra-thin heteroepitaxial graphite films," *Journal of Applied Physics* **92** (2002).

[106] A. Bostwick, T. Ohta, T. Seyller, K. Horn, and E. Rotenberg, "Quasiparticle dynamics in graphene," *Nat Phys* **3**, 36 (2007).

[107] M. P. C. B. M. L. Sadowski, G. Martinez and W. A. Deheer, "Magneto-spectroscopy of Epitaxial Graphene," *International Journal of Modern Physics B* **21**, 1145 (2007).

[108] S. Y. Zhou, G. H. Gweon, A. V. Fedorov, P. N. First, W. A. de Heer, D. H. Lee, F. Guinea, A. H. Castro Neto, and A. Lanzara, "Substrate-induced bandgap opening in epitaxial graphene," *Nat Mater* **6**, 770 (2007).

[109] D. Pines and D. Bohm, "A Collective Description of Electron Interactions: II. Collective vs Individual Particle Aspects of the Interactions," *Phys. Rev.* **85**, 338 (1952).

[110] D. Bohm and D. Pines, "A Collective Description of Electron Interactions: III. Coulomb Interactions in a Degenerate Electron Gas," *Phys. Rev.* **92**, 609 (1953).

[111] J. Allen, S. J., D. C. Tsui, and R. A. Logan, "Observation of the Two-Dimensional Plasmon in Silicon Inversion Layers," *Physical Review Letters* **38**, 980 (1977).

[112] T. Demel, D. Heitmann, P. Grambow, and K. Ploog, "One-dimensional plasmons in AlGaAs/GaAs quantum wires," *Phys. Rev. Lett.* **66**, 2657 (1991).

[113] S. Das Sarma and W.-y. Lai, "Screening and elementary excitations in narrow-channel semiconductor microstructures," *Phys. Rev. B* **32**, 1401 (1985).

[114] Q. Li and S. Das Sarma, "Collective excitation spectra of one-dimensional electron systems," *Phys. Rev. B* **40**, 5860 (1989).

[115] V. Cataudella and G. Iadonisi, "Magnetoplasmons in a two-dimensional electron gas: Strip geometry," *Phys. Rev. B* **35**, 7443 (1987).

[116] W. Kohn, "Cyclotron Resonance and de Haas-van Alphen Oscillations of an Interacting Electron Gas," *Phys. Rev.* **123**, 1242 (1961).

[117] P. A. Maksym and T. Chakraborty, "Quantum dots in a magnetic field: Role of electron-electron interactions," *Phys. Rev. Lett.* **65**, 108 (1990).

[118] L. Brey, N. F. Johnson, and B. I. Halperin, "Optical and magneto-optical absorption in parabolic quantum wells," *Phys. Rev. B* **40**, 10647 (1989).

[119] G. D. Mahan, *Many-Particle Physics*, 2nd ed. (Plenum, New York, N.Y., 1993).

[120] F. Stern, "Polarizability of a Two-Dimensional Electron Gas," *Phys. Rev. Lett.* **18**, 546 (1967).

[121] T. Ando, A. B. Fowler, and F. Stern, "Electronic properties of two-dimensional systems," *Rev. Mod. Phys.* **54**, 437 (1982).

[122] E. H. Hwang and S. Das Sarma, "Dielectric function, screening, and plasmons in two-dimensional graphene," *Phys. Rev. B* **75**, 205418 (2007).

[123] B. Wunsch, T. Stauber, F. Sols, and F. Guinea, "Dynamical polarization of graphene at finite doping," *New Journal of Physics* **8**, 318 (2006).

[124] M. Polini, A. H. MacDonald, and G. Vignale, "Drude weight, plasmon dispersion, and pseudospin response in doped graphene sheets," *arXiv preprint arXiv:0901.4528* (2009).

[125] Z. Fei, G. O. Andreev, W. Bao, L. M. Zhang, A. S. McLeod, C. Wang, M. K. Stewart, Z. Zhao, G. Dominguez, M. Thiemens, M. M. Fogler, M. J. Tauber, A. H. Castro-Neto, C. N. Lau, F. Keilmann, and D. N. Basov, "Infrared Nanoscopy of Dirac Plasmons at the GrapheneSiO2 Interface," *Nano Letters* **11**, 4701 (2011).

[126] H. Yan, X. Li, B. Chandra, G. Tulevski, Y. Wu, M. Freitag, W. Zhu, P. Avouris, and F. Xia, "Tunable infrared plasmonic devices using graphene/insulator stacks," *Nat Nano* **7**, 330 (2012).

[127] H. Yan, T. Low, W. Zhu, Y. Wu, M. Freitag, X. Li, F. Guinea, P. Avouris, and F. Xia, "Damping pathways of mid-infrared plasmons in graphene nanostructures," *Nat Photon* **7**, 394 (2013).

[128] W. Gao, G. Shi, Z. Jin, J. Shu, Q. Zhang, R. Vajtai, P. M. Ajayan, J. Kono, and Q. Xu, "Excitation and Active Control of Propagating Surface Plasmon Polaritons in Graphene," *Nano Letters* **13**, 3698 (2013).

[129] Z. Fang, Y. Wang, A. E. Schlather, Z. Liu, P. M. Ajayan, F. J. Garca de Abajo, P. Nordlander, X. Zhu, and N. J. Halas, "Active Tunable Absorption Enhancement with Graphene Nanodisk Arrays," *Nano Letters* **14**, 299 (2014).

[130] Z. Fang, S. Thongrattanasiri, A. Schlather, Z. Liu, L. Ma, Y. Wang, P. M. Ajayan, P. Nordlander, N. J. Halas, and F. J. Garca de Abajo, "Gated Tunability and Hybridization of Localized Plasmons in Nanostructured Graphene," *ACS Nano* **7**, 2388 (2013).

[131] H. Yan, F. Xia, Z. Li, and P. Avouris, "Plasmonics of coupled graphene microstructures," *New Journal of Physics* **14**, 125001 (2012).

[132] K. Y. M. Yeung, J. Chee, H. Yoon, Y. Song, J. Kong, and D. Ham, "Far-Infrared Graphene Plasmonic Crystals for Plasmonic Band Engineering," *Nano Letters* **0**, null (0).

[133] H. Yan, Z. Li, X. Li, W. Zhu, P. Avouris, and F. Xia, "Infrared Spectroscopy of Tunable Dirac Terahertz Magneto-Plasmons in Graphene," *Nano Letters* **12**, 3766 (2012).

[134] I. Crassee, M. Orlita, M. Potemski, A. L. Walter, M. Ostler, T. Seyller, I. Gaponenko, J. Chen, and A. B. Kuzmenko, "Intrinsic Terahertz Plasmons and Magnetoplasmons in Large Scale Monolayer Graphene," *Nano Letters* **12**, 2470 (2012).

[135] J. M. Poumirol, W. Yu, X. Chen, C. Berger, W. A. de Heer, M. L. Smith, T. Ohta, W. Pan, M. O. Goerbig, D. Smirnov, and Z. Jiang, "Magnetoplasmons in Quasineutral Epitaxial Graphene Nanoribbons," *Phys. Rev. Lett.* **110**, 246803 (2013).

[136] K. W. Chiu and J. J. Quinn, "Plasma oscillations of a two-dimensional electron gas in a strong magnetic field," *Phys. Rev. B* **9**, 4724 (1974).

[137] R. Roldán, M. O. Goerbig, and J.-N. Fuchs, "Theory of Bernstein modes in graphene," *Phys. Rev. B* **83**, 205406 (2011).

[138] J. Christensen, A. Manjavacas, S. Thongrattanasiri, F. H. L. Koppens, and F. J. Garca de Abajo, "Graphene Plasmon Waveguiding and Hybridization in Individual and Paired Nanoribbons," *ACS Nano* **6**, 431 (2012).

[139] A. Y. Nikitin, F. Guinea, F. J. Garcia-Vidal, and L. Martin-Moreno, "Surface plasmon enhanced absorption and suppressed transmission in periodic arrays of graphene ribbons," *Phys. Rev. B* **85**, 081405 (2012).

[140] R. Roldán, J.-N. Fuchs, and M. O. Goerbig, "Collective modes of doped graphene and a standard two-dimensional electron gas in a strong magnetic field: Linear magnetoplasmons versus magnetoexcitons," *Phys. Rev. B* **80**, 085408 (2009).

[141] R. Roldn, M. O. Goerbig, and J.-N. Fuchs, "The magnetic field particlehole excitation spectrum in doped graphene and in a standard two-dimensional electron gas," *Semiconductor Science and Technology* **25**, 034005 (2010).

[142] E. H. Hwang and S. Das Sarma, "Plasmon modes of spatially separated double-layer graphene," *Phys. Rev. B* **80**, 205405 (2009).

[143] A. Iyengar, J. Wang, H. A. Fertig, and L. Brey, "Excitations from filled Landau levels in graphene," *Phys. Rev. B* **75**, 125430 (2007).

[144] K. Shizuya, "Electromagnetic response and effective gauge theory of graphene in a magnetic field," *Phys. Rev. B* **75**, 245417 (2007).

[145] Y. A. Bychkov and G. Martinez, "Magnetoplasmon excitations in graphene for filling factors $\nu \leq 6$," *Phys. Rev. B* **77**, 125417 (2008).

[146] R. Roldán, J.-N. Fuchs, and M. O. Goerbig, "Spin-flip excitations, spin waves, and magnetoexcitons in graphene Landau levels at integer filling factors," *Phys. Rev. B* **82**, 205418 (2010).

[147] K. Kern, T. Demel, D. Heitmann, P. Grambow, K. Ploog, and M. Razeghi, "One-dimensional electronic systems in ultra-fine mesa etched InGaAs-InAlAs-InP quantum wires," *Surface Science* **229**, 256 (1990).

VITA

Wenlong Yu was born in Laixi, Shandong, China. He graduated from University of Science and Technology of China with a Bachelor of Science in Applied Physics in 2009. He then entered the graduate program in School of Physics at Georgia Institute of Technology in Atlanta, GA. He joined the Quantum Transport and Infrared Spectroscopy Laboratory under the supervision of Professor Zhigang Jiang. In the following years, he dedicated most of his time to nano-device fabrication and infrared magneto-spectroscopy.